UNIVERSITE PARIS DIDEROT

UFR de Physique

Mémoire présenté par

Davide Franco

pour l'obtention de l'

Habilitation à Diriger des Recherches

Solar neutrino physics with Borexino and beyond

soutenue le 12 mai 2016 devant un jury constitué de

M	S. Katsanevas	*président et examinateur*
Mme	C. Augier	*examinatrice*
M	C. Galbiati	*examinateur*
M	A. Giuliani	*rapporteur*
M	A. Ianni	*examinateur*
M	F. Piquemal	*rapporteur*
M	Ph. Schwemling	*rapporteur*

Contents

Section 1

Introduction

Neutrinos are fundamental particles, with neutral charge and a very tiny mass. They are produced in several processes like nuclear fusion or radioactive decays and are among the most abundant particles in the Universe. Despite that, neutrinos are extremely elusive and difficult to detect, since interact only via weak interactions. These two properties, the abundance and the low probability of interaction, make neutrinos ideal cosmic messengers: they can travel unimpeded over great distances, carrying direct information from unseen regions of our Universe. Without moving too far away, the most powerful neutrino source on the Earth is the Sun with a flux of about 60 billions per square centimeter per second. Solar neutrinos are produced in the Sun core mostly by the proton-proton (pp) fusion chain, with a subdominant contribution from the carbon–nitrogen–oxygen (CNO) cycle.

The study of solar neutrinos has given a fundamental contribution both to astroparticle and to elementary particle physics, offering an ideal test of solar models and offering at the same time relevant indications on the fundamental interactions among particles. One of the main experimental player in this field is Borexino, a solar neutrino experiment installed at the Gran Sasso Laboratory and running since 2007, detecting neutrino via elastic scattering off electrons in a scintillator target. Borexino has already produced a wide range of results in the solar neutrino sector, by performing the first real time solar neutrino spectroscopy observing neutrinos from the solar ^{7}Be, ^{8}B, *pep*, and *pp* reactions. The current effort of the collaboration is addressed on the CNO neutrinos. It i is worth remarking that the CNO cycle has a key role in astrophysics, since it is the dominant source of energy in stars more massive than the Sun and in advanced evolutionary stages of solar like stars. Further the speed of the CNO cycle is directly connected to the determination of globular clusters age, which is used to set a bound on the age of the Universe.

Borexino achieved also relevant results in the neutrino oscillation physics (e.g. day–night asymmetry), in geo–neutrino science, and in testing the fundamental physics laws (e.g. the Pauli exclusion principle and the neutrino speed of light).

The story of Borexino, however, begins much earlier than 2007. A first proposal was discussed already in 1988, when the physics goal was limited to the ^{8}B component only. The final proposal came 3 years later, with a much more ambitious goal: the real–time measurement of the solar neutrino rate in the MeV range. The ambition was directly proportional to the difficulty of such a measurement, which resided in the reduction of the natural radioactive background, intrinsic to the scintillator, at the same order of magnitude

of the signal. A challenge never attempted before, since the purification technologies of that time were not proved to be effective for such extreme requirements. On top of that, there was no detector able to measure so low levels of contaminations in the detector materials.

The Borexino collaboration started developing new purification technologies and a new ultra–low level background detector (CTF) for material screening. After more than 10 years of R&D's, the first results from Borexino were welcomed with surprise, even by the collaboration itself: the measured contamination level was below the requirement constraints and below the CTF sensitivity itself. With such a low background, Borexino had the opportunity to investigate many more physics channels than those foreseen by the original proposal, like the test of the sterile neutrino hypothesis, that will be tackled in the next years.

My research activity started with Borexino in 1999, and is still continuing. In the meanwhile I participated to other important experiences like Double Chooz focused on the measurement of the θ_{13} neutrino oscillation parameter, and DarkSide, a dual-phase liquid argon time projection chamber for the direct dark matter detection. I have chosen to describe in this dissertation my path along the Borexino story, which allows me to better illustrate my research activity following a single guiding thread.

Along this 15 years I participated to several aspects of the experiment, from the detector installation to the neutrino analysis. I have chosen four items, among several others, describing my technical contributions to Borexino (section 2): the analysis of the CTF data for testing the purification system, the Monte Carlo code, the calibrations, and an example of algorithm widely employed in the Borexino analyses. In particular, the first task began during my PhD thesis and continued afterward. Though this contribution is not evaluable in the HDR context, which takes into account only the research activity after the PhD, the CTF results (not only mine!) represent a fundamental milestone in the Borexino path toward the solar neutrino physics. I have then decided to include the description of the CTF analysis to explain one of the key features which led to the success of Borexino.

In section 4, I describe four solar neutrino analyses (^{8}B, ^{7}Be, *pep* and CNO, and *pp*) to which I directly and indirectly contributed: directly by developing the entire analysis (^{8}B) or a part of it (*pep* and CNO); indirectly by developing algorithms, evaluating systematics, running simulations, and, more in general, thanks to my contribution to the detector calibrations.

Also in the *pep* and CNO analysis, part of my contribution was included in my PhD thesis. In this specific case, the dominant source of background, the cosmogenic ^{11}C, was abated through two techniques I entirely developed: the three–fold coincidence (during my PhD) and the ortho–positronium tagging. The *pep* measurement would not be achieved without rejecting ^{11}C with a very high efficiency. Both the techniques were innovative, never attempted before, and used by other experiments after their publications. Describing the *pep* and CNO analysis could not be possible without mentioning my contribution to the three–fold coincidence.

The future of Borexino is two–fold: the precision era of the solar neutrino measurements, thanks to the higher statistics and to the purification campaigns planned to further reduce the background, and the sterile neutrino search with a very intensive source of anti-neutrinos placed close to the detector. I have been deeply involved in the neutrino source project (SOX) since the beginning and I contributed to define its optimal strategy by performing several sensitivity studies. I will then show, in section 5, the potential of Borexino in providing the ultimate word in the long standing sterile neutrino controversy.

The precision era of Borexino and the SOX project will presumably define the end of the experiment. But surely not the end of the solar neutrino physics, even if it is difficult to identify the successor of Borexino. The only candidate to date is SNO+, which is however mostly focused on the neutrino-less double beta decay. As already mentioned, since 3 years I am also involved in a new experiment, DarkSide for direct dark matter detection. DarkSide has recently demonstrated the high performances of this technology and, on this basis, the collaboration is starting to plan a very large volume detector. The natural question is: what about solar neutrino physics with a large liquid argon TPC? To answer to this question, I studied (see section 5) the advantages and the limitation of the liquid argon technology in the solar sector, demonstrating its high potential. Liquid argon in fact can be highly purified from radioactive contaminants and can provide a better detection resolution thanks to its scintillation yield, $\sim$4 times higher than the organic scintillators, like the Borexino one. I demonstrated with Monte Carlo simulations that a similar technology has potential to directly observe the last unseen component, the CNO one and to strongly improve the accuracy on the solar ^{7}Be and *pep* neutrino rates.

Section 2

Neutrinos, oscillations, and the Sun

The birth of the neutrino physics can be dated back to 1930, when Wolfgang Pauli hypothesized the existence of a neutral particle to uphold energy and momentum conservation in nuclear beta decays. Four years later, Enrico Fermi published the first theory of the beta decay of nuclei, including the Pauli's particle, named *neutrino*, with 1/2 spin a very small mass, much smaller than the mass of the electron. It took more than twenty years before Reines and Cowan [1] in 1956 detected anti-neutrinos by monitoring a volume of cadmium chloride with scintillating liquid near to a nuclear reactor. After 80 years of studies and experiments with and on neutrinos, remarkable progress has been achieved in our understanding of their properties and role in particle– and astro–physics, but, still, several fundamental questions are open.

Neutrinos are known to be tiny and neutral elementary particles. They interact with matter via the weak nuclear force but their interaction cross section is so small that matter is almost transparent to them. Neutrinos are produced by several sources: neutrinos in the Universe have origin in the Big Bang, in supernovae, or in fusion reactions inside stars like the Sun. Neutrinos are also produced by the interaction of cosmic rays with the Earth atmosphere and emitted in the radioactive decay of elements inside the Earth. In addition, anthropogenic neutrinos are produced in nuclear reactions inside nuclear power plants and in particle interactions at accelerators. Depending on the source and the environment in which neutrinos are produced, different types of neutrinos are created and their energies range from fractions of electron volt (eV) to 10^{18} eV, or higher, as shown in figure 2.1.

When the Standard Model of particle physics was constructed, in the mid 1970s, it was assumed that neutrinos are massless, that neutrinos and anti–neutrinos are distinct particles, and that all neutrinos are left–handed and all anti–neutrinos right–handed. These assumptions were justified by the non–observation of the right–handed neutrinos in experiments like the Goldhaber one in 1957, which implies a massless Dirac particle. Moreover, if the Standard Model could easily be extended to include massive neutrinos via the Higgs mechanism, particle theorists show reluctance to justify the consequent Higgs-neutrinoP interaction strength, which would be a trillion times weaker than the equivalent Higgs-top quark coupling one.

In the same year of the publication of the Goldhaber work, Bruno Pontecorvo proposed the idea that neutrinos can oscillate between neutrino and anti–neutrinos: *(...) if the theory of the two-component neutrino is not valid (which is hardly probable at present) and if the conservation law for the neutrino charge does not*

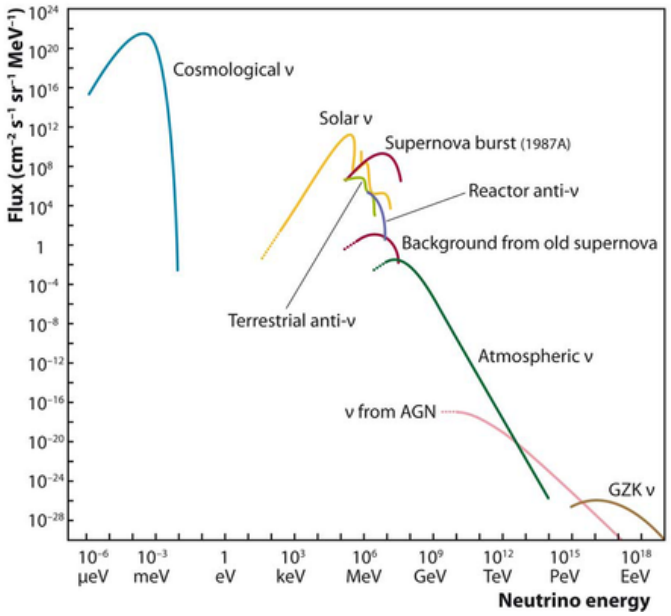

FIGURE 2.1: Fluxes and energy ranges of neutrinos from different sources.

hold, neutrino–antineutrino transitions in vacuum in principle be possible. After the muon neutrino was discovered, it was not difficult for Pontecorvo, in 1967, to extend the idea of neutrino oscillations to the case of electron and muon neutrinos. The main implication of the Pontecorvo's theory is the existence of massive neutrinos, a prerequisite for the oscillation phenomenon.

An alternative and elegant extension, able to conciliate the neutrino low mass issue with the Standard Model, is the seesaw mechanism, in which neutrino is a Majorana particles, i. e. it coincides with its own antiparticle. In this case, a particle produced as a neutrino might be capable of subsequently interacting as an antineutrino. The seesaw mechanism introduces a very heavy Majorana neutrino, with a mass of the order of some higher energy scale (for example the scale of grand unfication).

The first 40 years of life of the neutrino physics witnessed impressive progresses in terms of theoretic knowledge. At the same time, experimentalists took up the challenge to detect such elusive particles and to constrain the neutrino models. Historically, solar neutrino experiments played a fundamental role, since the Sun is one of the most abundant source of neutrinos reaching the Earth (6.4×10^{10} cm^{-2} s^{-1}). Raymond Davis Jr., who started investigating reactor neutrinos in the 1950s, in the 1970s successfully detected solar neutrinos scattering off chlorine nuclei, with an experiment located underground in the Homestake Gold Mine in South Dakota. Davis' experiment confirmed that the Sun produces neutrinos, but only about one-third of the number of neutrinos predicted by theory could be detected. This measurement was at the origin of the so–called "solar neutrino puzzle". Neutrino oscillations represented an optimal explanation to such a deficit. B. Pontecorvo, already three years before the publication of the first results of the Davis' experiment, wrote: *From an observational point of view the ideal object is the Sun. If the oscillation length is smaller than the radius of the Sun region effectively producing neutrinos (...) direct oscillations will be smeared out and unobservable. The only effect on the Earth's surface would be that the flux of observable sun neutrinos must be two times smaller than the total neutrino flux.*

Homestake will take data up to 1995 and will represent the pioneer experiment in the neutrino oscillation sector. Only in 1998 SuperKamiokande published the first evidence of neutrino oscillations with atmospheric neutrinos, followed by SNO in the solar sector in 2001, and KamLAND in 2003, using reactor neutrinos, observing for the first time the energy distortion induced by the oscillations. The oscillation discovery represents a milestone in particle physics, opening the long-awaited door to physics beyond the Standard Model. As natural consequence, the neutrino oscillation physics entered in the *precision era*, which means the accurate measurement of all the parameters which play a role in the oscillations. But accurate measurements do not exclude new physics. Several fundamental questions on neutrinos are still open, like the absolute mass of neutrinos, the mass hierarchy, the size of the CP violating phase, the Dirac or Majorana nature of the neutrino mass, and the existence of one or more sterile neutrinos.

The Borexino experiment, the focus of this dissertation, is temporally positioned in this phase. Borexino is a scintillator based detector designed to detect, in real time, low energy solar neutrinos, and in particular those from the ^{7}Be reaction. As will be discussed later, the unpredictable technological success of Borexino in reducing the background allowed to reach fundamental results, much beyond the primary goal. Borexino is in fact actually mapping the solar neutrino survival probability using solar neutrino sources with fluxes much lower than the ^{7}Be one, measured the geo-neutrino contribution, and is going to probe the existence of sterile neutrinos, as hinted by the so–called *reactor and gallium anomalies* with a very active neutrino source. Further, Borexino produced a rich set of results about technology and about critical physics topics related to ultra low background measurements. As a consequence, the technological success of Borexino is impacting on the design of the future generation of neutrino experiments.

To better appreciate the Borexino results, an overview on neutrino oscillations in vacuum and matter, neutrino physics, Solar physics, and the experimental state of the art will be presented in this section.

2.1 Neutrino oscillations in vacuum and matter effects

Neutrinos are produced and detected via the weak interaction as flavor eigenstates. However they propagate as mass eigenstates with distinct velocities. This can be modeled as a rotation by an angle θ of the flavor eigenstates with respect to the mass ones. The relation is expressed by a matrix equation, that, in the simplest case of two neutrino transition ($e \rightarrow x$), can be written as:

$$\begin{pmatrix} \nu_e \\ \nu_x \end{pmatrix} = \begin{pmatrix} cos\theta & sin\theta \\ -sin\theta & cos\theta \end{pmatrix} \begin{pmatrix} \nu_1 \\ \nu_2 \end{pmatrix} \tag{2.1}$$

In the Sun, only electron neutrinos are produced. Assuming an electron neutrino $|\nu_e\rangle$ produced at time *t*=0 with momentum $\bar{p}$, this will propagate in vacuum as the superposition of the two mass eigenstates:

$$|\nu_e(\bar{x},t)\rangle = cos\theta\,|\nu_1\rangle\, e^{-i\,(E_1 t - \bar{p}\cdot\bar{x})} + sin\theta\,|\nu_2\rangle\, e^{-i\,(E_2 t - \bar{p}\cdot\bar{x})}. \tag{2.2}$$

Under the assumption that the masses are small and neutrinos relativistic, $m << p$, the energy of the mass states is $E_j = \sqrt{\bar{p}^{\,2} + m^2} \simeq p + \frac{m_j^2}{2p}$ where $p = |\bar{p}|$ for mass states with momentum $p \simeq E$. The neutrino

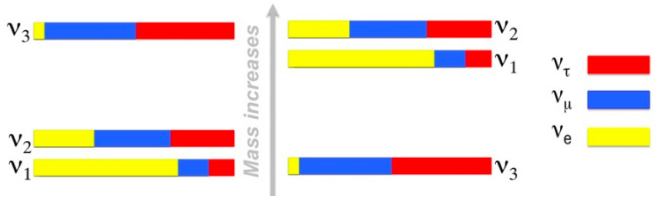

FIGURE 2.2: Normal (left) and inverted (right) hierarchy and flavor content of each individual mass state (from [2]).

survival probability to observe an electronic at time *t* can be expressed in terms of the square mass splitting $\Delta m^2 = m_1^2 - m_2^2$ as:

$$P(\nu_e \to \nu_e) = 1 - sin^2 2\theta \, sin^2 \frac{\Delta m^2}{4E} = 1 - sin^2 2\theta \, sin^2 \frac{\pi \, R}{L_0} \tag{2.3}$$

where $L_0 = \frac{4\,\pi\,E}{\Delta m^2}$ is the *vacuum oscillation length*, and *R* is the source-detector distance. In particular,

$$L_0 \simeq 2.47 \cdot \frac{E_\nu}{1\,MeV} \cdot \frac{1\,eV^2}{\Delta m^2} \cdot meters \tag{2.4}$$

The maximum oscillation amplitude occurs at $\theta = \pi/4$, also called *maximal mixing*. In the extension of the three neutrino mixing, the mixing matrix (PMNS) embodies four parameters for relating the three neutrino mass eigenstates to the three neutrino flavor eigenstates: three mixing angles (θ_{12}, θ_{13} and θ_{23}), two squared mass differences Δm^2_{12} and Δm^2_{31}, and one (if neutrino are Dirac particles) CP violating phase δ_{CP}. Nevertheless, two neutrino formalism represents an excellent approximation in most of the neutrino oscillation experiments, mainly because of their sensitivity to only one of the squared mass differences. The three mass-mixing formalism is required, for instance, in future oscillation tests aimed to measure the CP phase.

When neutrinos propagate in matter, they further undergo to coherent forward scattering through the weak interaction. Z^0-exchange processes (or neutral current) are the same for all the neutrino flavors, and generate a common phase that can be neglected. On the other hand, $W^{\pm}$-exchange (charge current) contributes only to ν_e scattering and significantly changes the propagation equation. This phenomenon was introduced for the first time by Wolfenstein in 1978 [3], and further by Mikheyev and Smirnov in 1985 [4], and it is known as Mikheyev–Smirnov–Wolfstein (MSW) effect. The evolution of the neutrino propagation in matter can be written as:

$$i\frac{d}{dt}\begin{pmatrix} \nu_e \\ \nu_x \end{pmatrix} = -\frac{M^2_{matter}}{2E}\begin{pmatrix} \nu_e \\ \nu_x \end{pmatrix} \tag{2.5}$$

where:

$$M^2_{matter} = \mathbf{U}\begin{bmatrix} m_1^2 + m_2^2 & 0 \\ 0 & m_1^2 + m_2^2 \end{bmatrix}\mathbf{U}^+ + \begin{bmatrix} A^{CC} + A^{NC} & 0 \\ 0 & A^{NC} \end{bmatrix} \tag{2.6}$$

U is given by eq. 2.1, and A^{CC} and A^{NC} the charge and neutral current terms, respectively. In particular, as already explained, the only potential which plays a role in the neutrino propagation in matter is

$$A^{CC} = A(x) = 2\sqrt{2}N_e(x)G_F E \tag{2.7}$$

where $N_e(x)$ is the electron density in the crossed medium,and G_F is the Fermi constant. The matrix operator of eq. 2.6 can be diagonalized, obtaining:

$$\begin{pmatrix} \nu_1^m \\ \nu_2^m \end{pmatrix} = \begin{pmatrix} cos\theta_m & sin\theta_m \\ -sin\theta_m & cos\theta_m \end{pmatrix} \begin{pmatrix} \nu_e \\ \nu_\mu \end{pmatrix} \tag{2.8}$$

where the mixing angle in matter θ_m , given by:

$$cos\theta_m = \frac{cos\theta - A(x)/\Delta m^2}{\sqrt{(A(x)/\Delta m^2 - cos2\theta)^2 + sin^2 2\theta}}. \tag{2.9}$$

is different from the vacuum mixing angle θ and therefore the matter eigenstates $|\nu_1^m\rangle$ and $|\nu_2^m\rangle$ do not coincide with the mass eigenstates $|\nu_1\rangle$ and $|\nu_2\rangle$. The oscillation length in matter is then:

$$L_m = \frac{L_0}{\sqrt{(A(x)/\Delta m^2 - cos2\theta)^2 + sin^2 2\theta}}. \tag{2.10}$$

If $\sqrt{2}G_F N_e(x) >> \frac{\Delta m^2}{2E} cos2\theta$, matter effects dominate and vacuum oscillations are suppressed. The resonance occurs at $\sqrt{2}G_F N_e(x) = \frac{\Delta m^2}{2E} cos2\theta$, with $\theta_m = \pi/4$ for $\Delta m^2 > 0$ in the neutrino case, and $\Delta m^2 < 0$ in the antineutrino one. In the Sun, the electronic density has very slow variations. At the solar neutrino energies, [0.1,20] MeV, this *adiabatic condition* is satisfied, and $|\nu_i^m\rangle$ (i={1,2}) are eigenstates in matter. The survival probability can be thus written as

$$P(\nu_e \to \nu_e) = \frac{1}{2}(1 + cos2\theta_m cos2\theta). \tag{2.11}$$

The survival probability is shown in figure 2.3 for the ^{8}B neutrino case from the Sun: the low energy region is dominated by vacuum oscillations, while the upper part is dominated by the mixing in matter.

2.2 Solar neutrinos

2.2.1 The Standard Solar Model

The Sun is the most abundant source of neutrinos on the Earth. Since neutrinos have origin mainly in the Sun's core, and most of them travel, unperturbed, up to Earth, they represent the ideal messengers for investigating the solar interior, and a precious resource for testing the flavor oscillation and mixing hypotheses. The mechanisms at the basis of the solar neutrino production are directly related to the energy production in the Sun. A robust neutrino flux prediction requires thus an optimal knowledge of the Sun chemical

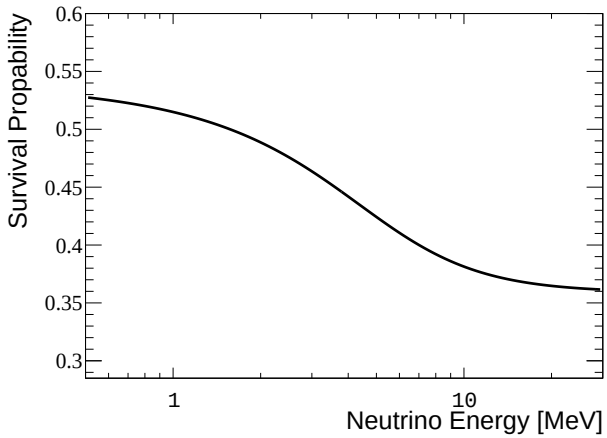

FIGURE 2.3: Survival probability of ^{8}B neutrinos from the Sun.

composition, reaction processes, and evolution. Until the late 1800's, the most accredited hypotheses explaining the source of the stellar energy were based on chemical reactions and gravitational contraction in the stars. Nevertheless, the energy that can be produced through these processes is not enough to account for the observed solar luminosity, integrated over its age, and estimated through geological considerations. It was Hans Bethe (1939) who first realized that the weak nuclear interaction was capable of converting a proton into a neutron during the brief encounter of a p+p scattering event. H. Bethe and C. H. Critchfield [5] presented the details of the full proton-proton (pp) chain of reactions (figure 2.4) that convert hydrogen to helium and allow the Sun to shine for about 10 billion years. The overall reaction balance can be represented by:

$$4p \rightarrow \alpha + 2e^+ + 2\nu_e \tag{2.12}$$

with a mass excess of 24.7 MeV plus 2 MeV from the annihilation of e^+'s. The pp-chain is now known to contribute about 98% of the Sun's energy production in its inner core. The remainder is contributed by the carbon-nitrogen-oxygen (CNO) cycle (figure 2.5), which was independently discovered by C. F. von Weizsäcker (1938) [6] and H. Bethe (1939) [7].

The Standard Solar Model (SSM) is the solution of a set of differential equations a solution of the stellar evolution equation which relies on several assumptions and is constrained by experimental boundary conditions. The evolution of the Sun is modeled from zero age to its current age, taking into account the conservation laws of physics, (that is the conservation of mass, momentum, and energy), the energy transport equation and the equations describing the nuclear reactions. The main ingredients of the SSM are the following:

- the Sun burns in hydrostatic equilibrium, maintaining a local balance between the gravitation force and pressure gradient;
- the mechanisms for energy transport are radiation and convection;
- the Sun produces its energy by fusing protons into 4He, via the pp chain, and by the CNO cycle;

- the isotope abundance changes only due to nuclear reactions;
- the initial solar interior is assumed chemically homogeneous.

The Solar equation of state is defined for an ideal gas, as hydrogen and helium are almost completely ionized in the Sun's core, corrected to account for the incomplete ionization of metals and for the radiation pressure. The basic boundary conditions, mass, age, radius, and luminosity, are determined experimentally. The energy transport in the inner part ($\sim$70% or the radius) of the Sun is radiative, while in the external shell is convective. In particular, the very high temperatures in the solar interior are responsible of frequent and energetic collisions among the particles of the gas, which is completely ionized inside and near the core. Atoms have no free electrons able to capture photons, making the inner part of the Sun transparent to radiation. The energy produced by nuclear reactions in the core travels, with a timescale of millions of years, towards the external shell, where the temperature fails, and photons are absorbed by atoms. The Sun becomes more and more opaque, at larger radius, where the energy transport is dominated by convection: the hot solar gas moves outward, while the cooler gas moves inward. The convection is directly observed by astronomers, looking at the granularity of the visible surface, which shows regions of bright and dark gas. Granule velocities ($\sim$1 km/s) and directions are measured exploiting the Doppler effect.

Observing the motion of the solar surface, it is possible also to determine the frequencies of the so–called *sound* waves, the result of internal pressure waves that reflect off the photosphere and cross the solar interior. The helioseismology can infer several critical parameters, like the opacity, the boundary of the convective region, and the heavy element composition of the Sun. The techniques adopted to deduce the chemical composition and the recent results on the heavy element abundance, which lead to important consequences on the neutrino flux predictions, will be discussed in the next subsection.
Other parameters, like the initial helium composition, can be determined interactively, requiring that the actual solar luminosity and the radius have been produced after 4.6×10^9 years.
In the last two decades, Bahcall and his collaborators developed an elaborate SSM, frequently updated following the most robust and available physics as input data (see references [8] [9] [10] [11] as examples of SSM's). In this work, we assume the Bahcall model as the reference one, but it worth to remark that a number of alternative models are present in literature (see for instance [12] by S. Turck-Chiéze et al.). As it will be later discussed, the SSM predictions played a key role in the comprehension of the neutrino oscillations. Presently, the precise knowledge of the flavor oscillation and mixing phenomena allows to operate in the opposite direction, *id est* testing the SSM by comparing its predictions with the measured neutrino rates.

2.2.2 The metallicity problem

The abundance of the heavy–elements, Z (aka *metals*, id est all the elements with an atomic number in the [6–26] range) in the Sun is a critical parameter in the SSM, since it affects the radiative opacity, and the boundary definition of the convective zone. In particular, abundances of oxygen, carbon, and nitrogen, as already mentioned, have a direct impact on the energy production of the Sun via the CNO cycle. The role of Z is also important in other sectors, as a reference in the metallicity of the stars and in the chemical evolution of galaxies.

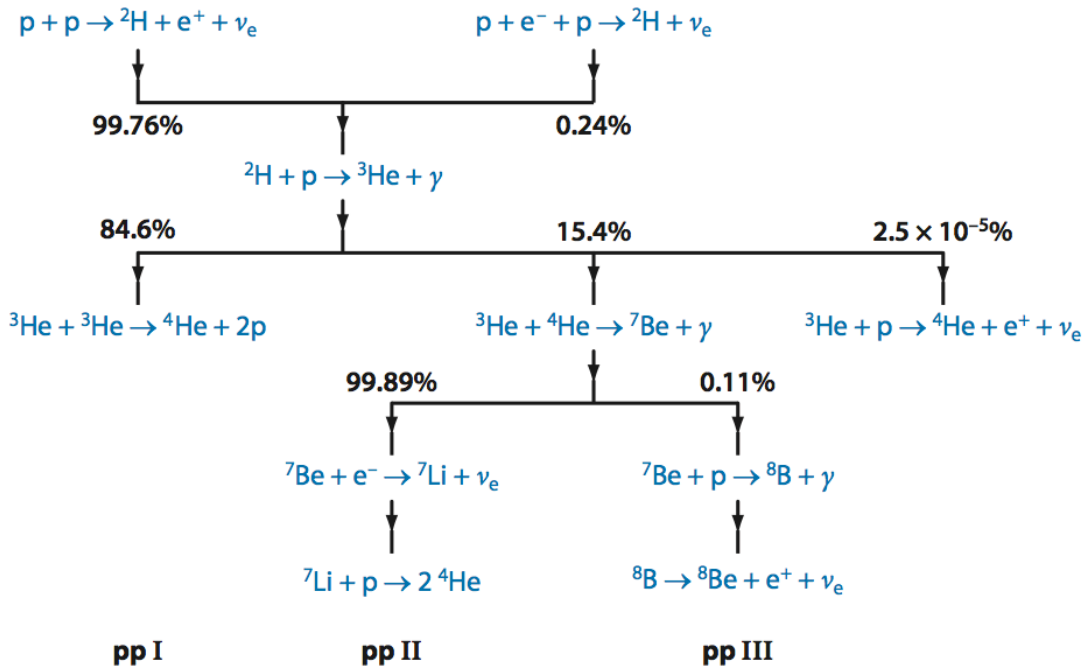

FIGURE 2.4: The proton-proton (pp) chain of nuclear fusion reactions in the Sun. The % values indicated are the branching ratio of each reaction.

The determination of the overall abundances of the elements in the Sun relies on two independent techniques: the analyses of the solar photospheric spectrum and of the pristine meteorites or chondrites, assuming these parameters unchanged over the Sun's lifetime. Each method complements the weakness of the other. Indeed, the measurements of the element abundances in meteorites are extremely accurate, but some elements, like H, He, C, N, O and Ne, are volatile, and partially escape the meteorites. Conversely, the absorption lines in the solar spectrum depend on the solar atmosphere models, and the accuracy in the line formation process is typically worse than or equal to $\sim$10%. The study of the photosphere, in particular, knew an important revision in 2005, which led to dramatic changes in the SSM predictions. Asplund and others [13] adopted a new sophisticated 3D stellar atmospheric model, obtained by 3D radiation-hydrodynamic simulations of the near–surface layers of the Sun. Their results were in excellent agreement with several independent measurements, among which with most of the pristine meteorite results. However, they found also indications on lower abundances (between 35 and 45%) of carbon, nitrogen, and oxygen, than those listed in the previous compilation (GS98 [14]), obtained by using a one–dimensional model. The revision of the oxygen abundance led to a comparable change in the neon and argon ones, since these abundances are generally measured through the Ne/O and Ar/O ratios. Further, also the silicon abundance was lowered down by $\sim$10 % with respect to the GS98 value, and, more in general all the abundances measured by looking at the pristine meteorites were re-normalized by a similar factor. To summarize the overall

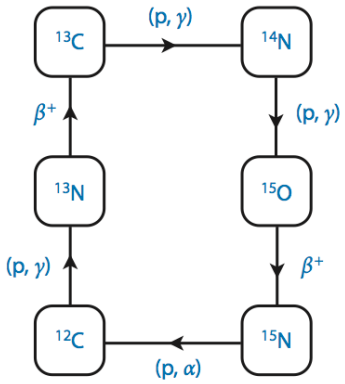

FIGURE 2.5: The CNO cycle.

variation, the traditional variable that embeds all abundances into a single quantity, the total heavy element–to–hydrogen ratio, Z/X, scaled from 0.023 to 0.0165, corresponding to a difference of ∼28%. The new set of measurements was listed in a compilation, said AGS05 [13], by Asplund, Grevesse and Sauval. The 2009 compilation (AGSS09 [15]) further improved the model describing the radiative transfer and updated opacities. The new model is in excellent agreement with the center-to-limb variation of the temperature gradient observed in the Sun [16] [17], and resulted in Z/X equals to 0.0178. The AGSS09 combines the photospheric abundances for the volute elements (C, N, O, Ne, and Ar) and the chondritic values for the remaining elements. Since the photospheric abundances are systematically larger than the meteoritic ones for the Mg, Ca, and Fe elements, a modified AGSS09 model, called AGSS09ph [18], assumes all the adopted abundances from the recommended solar photospheric ones only. This allows to study the impact of the chondritic values. The latter model predicts a Z/X value equals to 0.0181.

Even if the new heavy–element abundance is supported by robust data and provides excellent agreements with several independent measurements, the new SSM introduces some conflicts, especially with helioseismolgy results on the relative sound-speed and solar density, and strongly affects the neutrino fluxes. Figure 2.6 shows the comparison between SSM BP05 [10] predictions and measurements, assuming the GS98 and AGSS09 models: the new low–metallicity model increases the disagreement, previously almost negligible, by up a factor ∼5. The reason lies on the determination of the convection zone base, the point where opacity is sufficiently small to allow the full radiative transportation of the entire heat flux. As already mentioned, the opacity has a direct dependence on the heavy–element abundance, while the convection zone base affects the sound speed propagation. The base is located around 0.726×R in the GS98 model, and at 0.729×R in the AGS05 one, with a difference of ∼15 σ from the seismically determined value [19]. The difference is reduced to ∼11 and ∼9 σ with the AGSS09 and AGSS09ph models, respectively [18].

Another large effect due to the lowering of the heavy–elements is related to the helium abundance Ys change in the convection zone. The helium abundance of solar models needs to be changed in order to satisfy solar constraints at the current age of the Sun. The reduction of Z/X causes a reduction of Ys in the calibrated

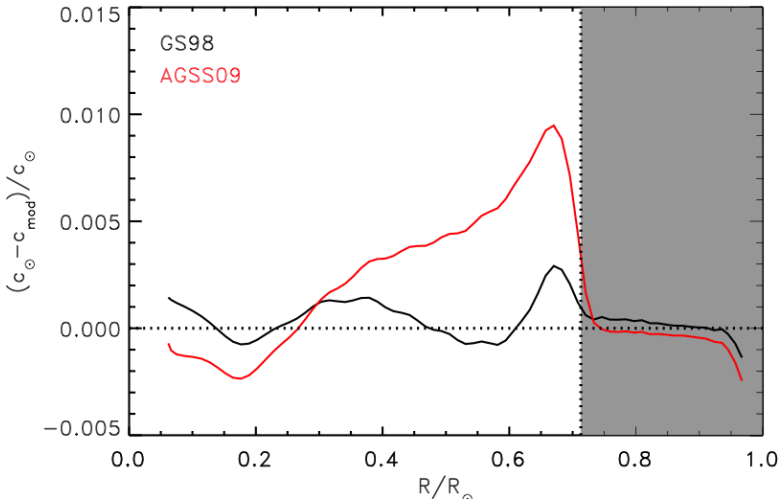

FIGURE 2.6: Relative sound speed (top) and density (bottom) differences, in terms of (Sun - Model)/Model, between solar models and helioseismology results (from [18]).

solar models. While the SSM BP05 predicts a difference of 1.8 σ using the GS98, the AGS05, AGSS09, and AGSS09ph predict a difference of 5.5, 5, and 4 σ, respectively, from the seismically determined value.

In order to reconcile helioseismology data and the SSM, Bahcall et al. [20] tried to artificially modifying opacities in the SSM, estimating that increasing 21% of the opacities would recover the good agreement at the bottom of the convective zone. However, an error of 20% in the radiative opacity does not seem possible, since experimental data have an accuracy of 4%. The metallicity problem is still unsolved.

An help in solving the puzzle can come from the comparison between the SSM and the solar neutrino rate measurements. In fact, predictions of neutrino fluxes are strongly affected by the metallicity models and precise measurements can hence provide a further constraint to the SSM. The differences in the fluxes, component by component, are quoted in table 2.1. The energy spectra are shown in figure 2.7. As already mentioned, the largest discrepancy involve the CNO neutrino components (about 30%), which, however, have a relatively low fluxes, and hence, difficult to be accurately measured. pp, hep, and pep neutrinos are almost unaffected, while ^{7}Be and ^{8}B components have been reduced by $\sim$10% and $\sim$20%, respectively. The theoretical errors on ^{7}Be and ^{8}B are almost completely uncorrelated, and hence, a very large fraction of the total error is canceled in the ratio between the two fluxes. The ^{7}Be/^{8}B neutrino flux ratio represents thus the most robust test of the SSM achievable by solar neutrino experiments.

Model	pp	pep	hep	^{7}Be	^{8}B	^{13}N	^{15}O	^{17}F
$\times$ [cm^{-2} s^{-1}]	10^{10}	10^{8}	10^{3}	10^{9}	10^{6}	10^{8}	10^{8}	10^{6}
GS98	5.97	1.41	7.91	5.08	5.88	2.82	2.09	5.65
AGS05	6.04	1.44	8.24	4.54	4.66	1.85	1.29	3.14
AGSS09	6.03	1.44	8.18	4.64	4.85	2.07	1.47	3.48
AGSS09ph	6.01	1.43	8.10	4.79	5.22	2.15	1.55	3.70

TABLE 2.1: Neutrino fluxes from different models (from [18])

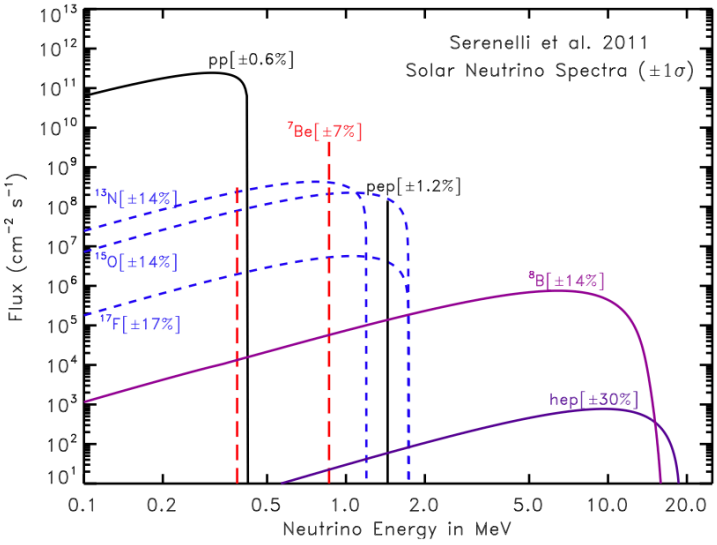

FIGURE 2.7: Energy spectrum of the pp and CNO chain solar neutrinos according to the BPS08 [11] solar model.

2.2.3 Solar neutrino experiments

Towards the end of 1940s, B. Pontecorvo [21] and L. Alvarez [22] independently proposed to detect solar neutrinos via capture on ^{37}Cl:

$$\nu_e + ^{37}Cl \rightarrow ^{37}Ar + e^- \tag{2.13}$$

with an energy threshold of 0.814 MeV, and thus sensitive mainly to ^{7}Be, ^{8}B, and CNO neutrinos. R. Davis, also motivated also by the improvements on the SSM neutrino flux predictions by J. Bahcall, raise the challenge with a detector of 615 tons of C_2Cl_4, installed in the Homestake gold mine in Lead, South Dakota [23]. The detector was shielded by 4200 m of water equivalent rock. ^{37}Ar atoms were extracted periodically every couple of months, bubbling helium gas through the liquid. Small ($\sim$0.5 cm^3) proportional chambers measured the 2-3 keV Auger electrons emitted by the ^{37}Ar electron capture decay ($\tau_{1/2} \sim 35$ days). The experiment successfully measured a solar neutrinos rate, averaged over the 25 years of data taking (1970-1995), of $2.56 \pm 0.16\,(stat.) \pm 0.16\,(syst.)$ SNU (1 SNU = 10^{-36} captures per target atom per second),

approximately 1/3 of the expected rate. The so-called Solar Neutrino Problem was initially addressed to the small fraction of detectable solar neutrinos (mainly from the ^{7}Be and ^{8}B reactions), because of the energy cut which excludes the main contribution from pp neutrinos, and to the large theoretical uncertainties due to the strong rate dependence on the solar temperature.

In the 1990's, other two radiochemical experiments, GALLEX [24][25] and SAGE [26][27][28], used a lower threshold (0.233 MeV) reaction,

$$\nu_e + ^{71}Ga \rightarrow ^{71}Ge + e^- \tag{2.14}$$

able to detect also pp neutrinos, which represent $\sim$53% of the overall interaction rate. The extraction process, which allows to identify one germanium atom among 5×10^{29} atoms of gallium, was measured with an efficiency of $\sim$90%. The so–collected ^{71}Ge is then transformed into GeH_4 gas, to fill the low-background proportional counters, which detect the electron capture decays with an half-life of 11.4 days. SAGE is located in the Baksan Underground Laboratory in the North Caucasus and it consists of 50 tons of metallic gallium. The data taking, still running at the present days, started in 1990. GALLEX, located in the Gran Sasso Underground Laboratory in Abruzzo, Italy, used 100 tons of gallium chloride solution, containing 30 tons of ^{71}Ga. The data taking, started in 1991 and lasted 6 years. After that, the detector data acquisition system and the electronics were upgraded, and the experiment continued the data taking for other 5 years, under the name of GNO [29].

The gallium experiments show a clear deficit in their observed neutrino rates compared to SSM predictions, but, unlike Homestake, the gallium deficit is only about a factor $\sim$2. The comparison between chlorine and gallex results could not be explained with either standard or nonstandard solar model predictions, but were in agreement with the neutrino oscillation hypothesis.

The limitations of radiochemical experiments, which can measure the integrated solar neutrino rate only and have no sensitivity to the neutrino directionality, were overcome by the large imaging water Cerenkov detectors, which brought an important development in the neutrino physics. Kamiokande [30], originally built as proton decay experiment in the 1980's in the Kamioka mine in Japan, was upgraded in 1985 to detect ^{8}B solar neutrinos. Kamiokande consisted of 3 ktons of water, surrounded by 950 photomultiplier tubes (PMTs), and shielded by $\sim$1,000 m of rock. Cerenkov light produced by energetic charged particles arising from neutrino interactions, produces ring-like patterns where the cone intersects the surface formed by the photomultiplier tube array. Cerenkov detectors can reconstruct the direction of the recoiling charged particle and the event energy in real time mode. The first result in 1988 confirmed the deficit observed by the chlorine experiment. The puzzle of solar neutrinos was enriched by a new apparent paradox: in the solar fusion chain, boron is created via the ^{7}Be reaction, and Kamiokande, sensitive to ^{8}B neutrinos only because of the 7.5 MeV energy threshold, saw a larger flux than the Chlorine experiment one, which includes both ^{7}Be and ^{8}B neutrinos.

The combination of all the results from Homestake, SAGE, GALLEX/GNO, Kamiokande, and the later high-statistics Super-Kamiokande [31] (50 ktons of water and over 11,000 PMTs) electron scattering measurement, can be explained only by the hypothesis of neutrino oscillations, governed by the mass-mixing parameters (Δm_{12}, θ_{12}). The degeneracy in the parameter space, however, did not allow to identify the correct solution resulting from either the vacuum oscillation or the MSW effect, even if the latter was preferred at large mixing angle.

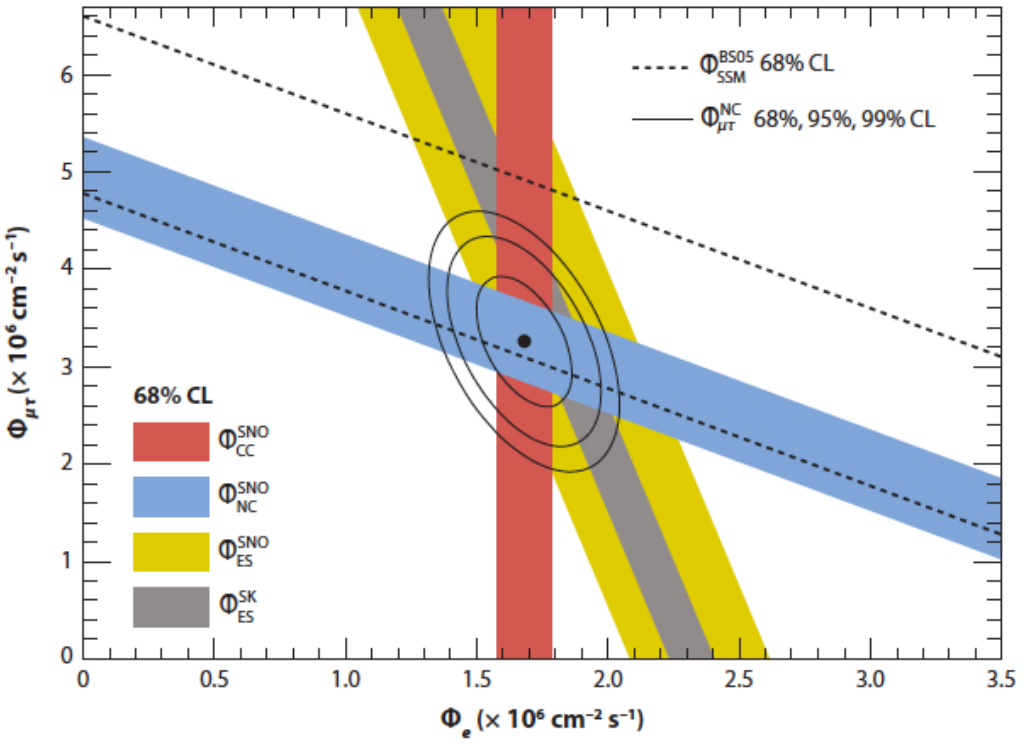

FIGURE 2.8: . Combined ν_μ and ν_τ fluxes versus the ν_e flux for the CC, NC, and ES SNO interaction channels, and for the ES SuperKamiokande one. The dashed lines define the prediction of the total ^{8}B neutrino flux from the SSM.

The definitive confirmation of the solar neutrino oscillation came from SNO [32][33], a Cherenkov experiment using 1,000 tons of ultra-pure heavy water (D_2O) housed in an acrylic vessel. The entire vessel was shielded by ordinary light water and surrounded by ∼9,500 PMTs. SNO is installed at a depth of 2 km in Sudbury, Ontario in Vale's Creighton nickel mine. Heavy water provides deuterons to serve as targets for neutrino interactions via both charged– (CC) and neutral–current (NC) neutrino interactions, in addition to the elastic scattering (ES) interactions off electrons:

$$\begin{aligned} \nu_e + d &\rightarrow p + p + e^- \quad (CC) \\ \nu_x + d &\rightarrow p + n + \nu_x \quad (NC) \\ \nu_x + e^- &\rightarrow \nu_x + e^- \quad (ES) \end{aligned} \tag{2.15}$$

where x=$\{e, \mu, \tau\}$. The CC reaction is sensitive to electron neutrinos only, while the NC one is equally

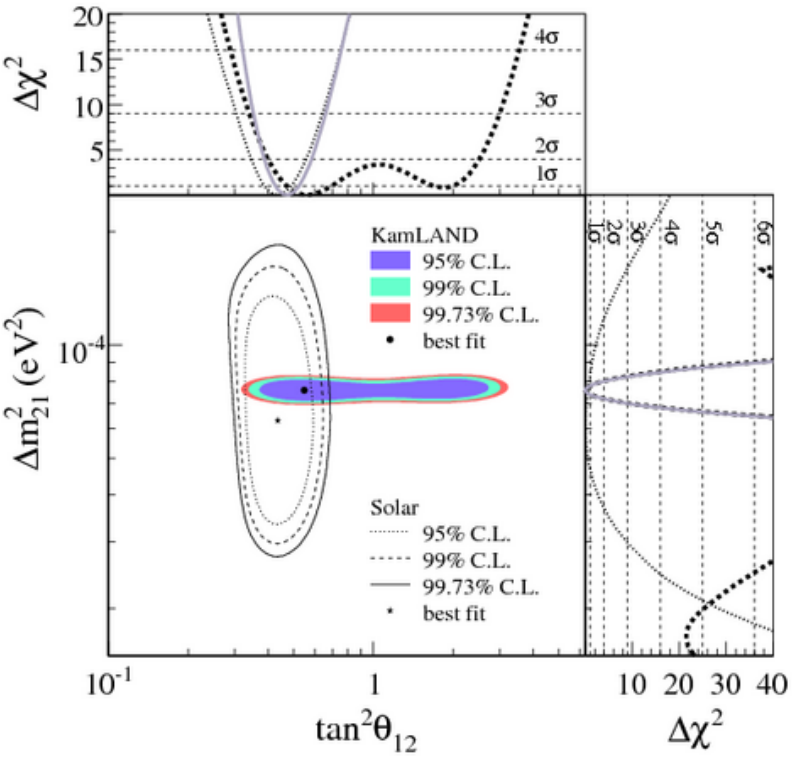

FIGURE 2.9: Two-flavor neutrino oscillation analysis contour using both solar neutrino and KamLAND results.

sensitive to all the neutrino flavors. The ES reaction has a cross section ∼6.5 higher than other two flavor ones. The SNO experiment, sensitive to the ^{8}B neutrino interactions only because of the ∼5 MeV energy threshold, was performed in three stages: with pure heavy water, adding salt (NaCl) to enhance the NC signal sensitivity with neutron capture on ^{35}Cl, and deploying into the detector an array of ^{3}He proportional counters for an independent event–by–event identification of NC events. The three reactions provide almost independent observations of the two neutrino fluxes: the electron and the combined muon and tau ones, as shown in figure 2.8 for the salt phase. The NC rate, independent on the neutrino oscillations, was in excellent agreement with the SSM expectations, while the electron neutrino flux, from the CC and ES reactions, was measured in ∼1/3 of the NC one, in agreement with the neutrino mixing in the MSW hypothesis. More important, the no flavor mixing hypothesis was disfavored by 7 σ by the SNO results. The different deficit observed by the radiochemical experiments can thus be explained by the different regime of oscillations at lower energies, dominated by the vacuum one.

A reactor neutrino experiment, KamLAND, as better explained in the next section, will prove the matter effect in the solar sector, by measuring the Δm^2_{12} parameter, and constraining θ_{12} in combination with the solar neutrino results, as shown in figure 2.9. KamLAND, further, directly observed the L/E spectrum distortion induced by the oscillation phenomenon.

Even if the solar neutrino oscillation was extremely well established by these set of experiments, a complete solar neutrino spectroscopy is still necessary for several reasons. First of all, these measurements do not solve the solar metallicity problem. Also, they do not completely disfavor another oscillation parameter region located at very low Δm^2_{12} (∼10^{-7} eV^2). Further, the transition region between the two oscillation

Source	Type of ν	$\bar{E}$ [MeV]	L [km]	min(Δm^2)
Reactor	$\bar{\nu_e}$	$\sim$1	$\sim$1	$\sim 10^{-3}$
Reactor	$\bar{\nu_e}$	$\sim$1	$\sim 10^{2}$	$\sim 10^{-5}$
Accelerator	ν_μ, $\bar{\nu_\mu}$	$\sim 10^{3}$	$\sim$1	$\sim$1
Accelerator	ν_μ, $\bar{\nu_\mu}$	$\sim 10^{3}$	$\sim 10^{3}$	$\sim 10^{-3}$
Atmospheric	$\nu_{\mu,e}$, $\bar{\nu_{\mu,e}}$	$\sim 10^{3}$	$\sim 10^{4}$	$\sim 10^{-4}$
Sun	ν_e	$\sim$1	$\sim 10^{8}$	$\sim 10^{-11}$

TABLE 2.2: Δm^2 sensitivity of typologies of neutrino experiments as function of the neutrino flavor, energy, and path length (from [34])

regimes, the matter– and the vacuum– dominated, expected between 1 and 5 MeV and not yet proved, is sensitive to non–standard interactions and to sterile neutrino oscillations (discussed in the next sections). Up to the SNO results, real–time experiments observed only a very small fraction (about 1%) of the total neutrino flux, and mainly from the ^{8}B component only. Moreover, radiochemical experiments, which have lower energy threshold, can not disentangle the solar neutrino components, since they are able to measure the integrated flux only. The difficulty in lowering the energy threshold, and observing in a real–time mode the solar neutrino interactions, mainly depends on the capability to face and suppress the radiogenic background. The presence of several radioactive contaminants, especially from the ^{238}U and ^{232}Th isotope chains, in the active mass target and, more in general, in the detector materials, represents an intrinsic limitation to the low energy solar neutrino detection up to $\sim$5 MeV, corresponding to the ^{208}Tl Q–value, the highest among the radioactive elements naturally present in nature.

Borexino, the focus of this dissertation, raise up the challenge to investigate the lower energy neutrino components from the Sun, using 300 tons of scintillator. It was primarily designed to detect the ^{7}Be component only, the second, after the pp one, in terms of flux (a summary of the overall solar neutrino results, up to the ^{7}Be measurement, is shown in figure 2.10). The excellent radio–purity achieved in the scintillator with the *adhoc* developed purification techniques, opened the door to other neutrino components, actually the ^{8}B (with 3 MeV energy threshold), pep, CNO, and pp ones, performing an almost complete solar neutrino spectroscopy. Borexino started the data taking in 2007, and is still running. It already measured ^{7}Be, ^{8}B, pp, and pep neutrino rates, setting the most stringent limit on the CNO component. The present and second data taking phase, said the precision one, finished at the end of 2014, with the first direct pp neutrino observation. In the next future, Borexino will try to further purify the scintillator to observe CNO neutrinos. Beyond this results, Borexino achieved several goals in other sectors, like in the detection of neutrinos from the Earth and in the measurement of the neutrino velocity. The Borexino experiment, to which I contributed for almost 15 years, will be widely discussed in the next sections.

2.3 Neutrino oscillations in the other sectors

Each neutrino experiment analyzes a particular region of the parameter spaces depending on the neutrino flavor, energy and path length, as shown in table 2.2 for the Δm^2 sensitivity. In addition, they can probe the oscillations by observing either flavor appearance or disappearance. The experiments on atmospheric, solar, reactor, and accelerator neutrinos are thus complementary, and all of them contribute to constraining the three mixing angles, two mass terms, and, possibly, the CP-phase. The solar sector has been already

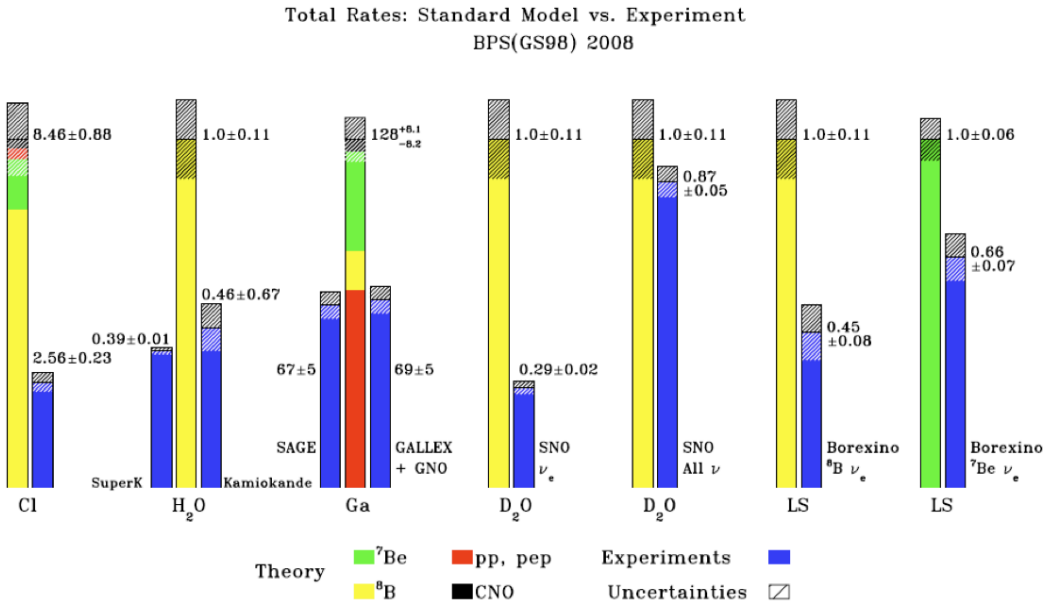

FIGURE 2.10: Comparison between experimental data and predictions from the SSM BPS08(GS98).

discussed. The next subsections are dedicated to summarize the status of the oscillations, observed by detecting atmospheric, reactor, and accelerator neutrinos.

2.3.1 Atmospheric neutrinos

Atmospheric neutrinos are produced by the decay chains of pions and kaons, originated by the interactions of the cosmic rays with air nuclei in the upper Earth atmosphere. Pions and kaons decay to ν_μ ($\bar{\nu}_\mu$) and μ^+ (μ^-). These, in turn, decay to e^+ (e^-), ν_e ($\bar{\nu}_e$), and $\bar{\nu}_\mu$ (ν_μ). The ratio R = $(\nu_\mu + \bar{\nu}_\mu)/(\nu_e + \bar{\nu}_e)$ $\sim$2 represents a robust prediction (at $\sim$5% level in the [0.1–10] GeV energy range [35]), independently on the knowledge of the absolute flux of atmospheric neutrinos. Neutrinos are detected mainly exploiting charge current interactions on nuclei, and observing electrons and muons produced in the final states. Atmospheric neutrino experiments, located underground to suppress the cosmic ray background, detect the light induced by the Cherenkov effect, a process notably efficient in the particle discrimination: muons, in fact, being more massive with respect to electrons, are subjected to a minor scattering, and produce a better defined ring of light. This technique further allows to measure the directionality of the leptons produced in the charge current reactions, and hence to infer the neutrino direction. The residual component of tau neutrinos can not be identified because of the very short tau lifetime.

In the early 1980s, the first massive (kton) underground detectors were constructed: Kamiokande [36] in Japan, and IMB [37] and Soudan [38] in the USA. In 1988, Kamiokande observed an overall reduction of the ratio R, using 3 kton of ultra pure water. This result was confirmed, a few years later, by IMB, with 10 kton of ultra pure water target, and by Soudan, a 960 ton iron tracking calorimeter. However, these experiments were unable to provide an unambiguous proof on the origin of the deficit, that is an increase of e–like events or a decrease of μ–like events. The definitive answer came, in 1998, from Super–Kamiokande, a detector with a water mass of 50 kton and equipped with $\sim$11,000 photomultiplier tubes. The deficit was compellingly attributed to the disappearance of ν_μ, crossing the Earth, and hence upward directed. Vertically downward-going neutrinos travel about 15 km while vertically upward-going neutrinos travel about 12,800 km before interacting in the detector. The Super–Kamiokande data showed that the deficit of μ-like events depended on the zenith angle, and thus on the neutrino flight length, as shown in figure 2.11. The result was later confirmed by MACRO [39] and Soudan-2 [40]. Since no up-down asymmetry has been observed for ν_e, atmospheric zenith distribution data can thus be interpreted as consequence of the dominant $\nu_\mu \rightarrow \nu_\tau$ flavor changes, with at most a subdominant contribution from $\nu_\mu \rightarrow \nu_e$. The flavor oscillation analysis is governed by the (Δm^2_{32}, θ_{23}) parameters, with an almost negligible role of ν_e matter effects, probing essentially the vacuum ν_μ oscillations. In 2013, Super–Kamiokande published [41] the evidence for the appearance of atmospheric tau neutrinos (3.8 σ), providing a further definitive proof supporting the $\nu_\mu \rightarrow \nu_\tau$ oscillation hypothesis.

2.3.2 Reactor neutrinos

Reactor neutrinos have an historical fundamental role since they were the first to be observed in the famous experiment by Reines and Cowan [42] [1], in 1956. Reactors are an intense source of electron anti–neutrinos, and depending on the baselines, they can probe different parameter regions by looking at the neutrino disappearance. Electron anti–neutrinos have the advantage to interact via inverse beta decay on protons,

$$\bar{\nu}_e + p \rightarrow n + e^+ \tag{2.16}$$

with relatively high cross section ($\sim 10^{-42}$ cm^2 in the MeV range), and with an efficient detection technique based on the neutron–positron time–space coincidence. Depending on the neutrino baseline, that is the source–detector distance, reactor anti–neutrinos can constrain different oscillation parameters. The reaction has, however, an intrinsic threshold of $\sim$1.8 MeV.

As already mentioned, KamLAND [43] probed the oscillation in the so–called solar sector. KamLAND is a 1 kton scintillator detector installed in in the Kamioka mine, in Japan. The site is surrounded by 53 Japanese commercial nuclear reactors, distributed in 16 sites in Japan and the nominal thermal power output 152 GW. The Kamioka site has a favorable condition, since 80% of neutrino contribution comes from 130 to 220 km, the distance relevant for the solar large mixing angle solution. The average baseline is $\sim$180 km. The KamLAND signature relies on the neutron capture on proton, which produces the characteristic 2.2 MeV gamma, and follows the positron annihilation, delayed by a few hundreds of microseconds. The KamLAND collaboration demonstrated in 2003 [43], for the first time, the reactor $\bar{\nu}_e$ disappearence at long baselines with high confidence level (99.95%). In 2008 [44], they provided a precision measurement, with 2881 ton x year exposure, of the Δm^2_{12} and an improvement on the constraint of θ_{12} (see figure 2.10). The

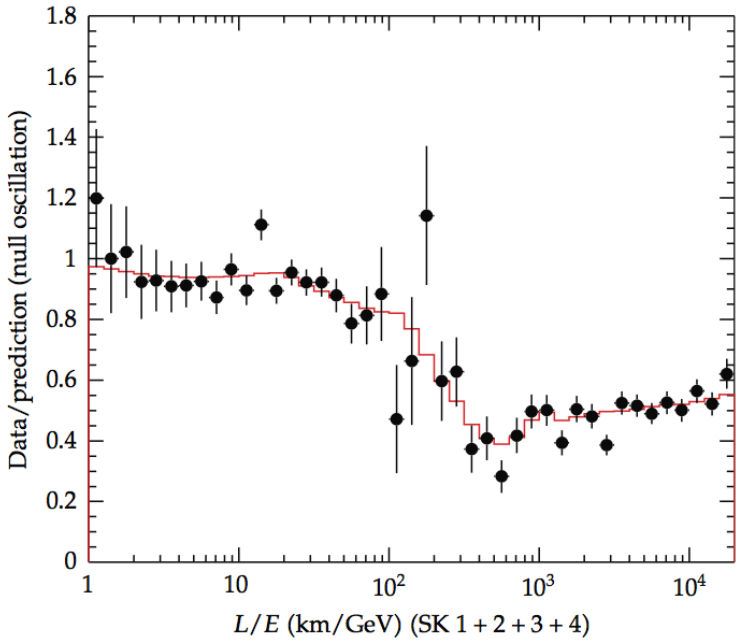

FIGURE 2.11: L/E distribution from Super-Kamiokande (240–kton × year exposure). Data over no-oscillation Monte Carlo prediction are plotted as a function of L/E. The red histogram shows the best fit for the $\nu_\mu \rightarrow \nu_\tau$ expectation..

oscillation induced distortion on the L/E spectrum, from the latter analysis, are in excellent agreement with the large mixing angle solution, as shown in figure 2.12.

At shorter baselines, on the km scale, reactor experiments can investigate the oscillation dependence on the θ_{13} mixing angle. Since reactor neutrino energy range is below the threshold for muon production, θ_{13} can be measured only through the disappearance of the antineutrinos. The probability that an electron antineutrino of energy E (in MeV) changes its flavor, after traveling a distance of L (in meters) is:

$$P_{ex} = sin^2 2\theta_{13} sin^2 \left(1.267 \frac{\Delta m^2_{31} L}{4E}\right) + cos^4 \theta_{13} sin^2 2\theta_{12} sin^2 \left(1.267 \frac{\Delta m^2_{21} L}{4E}\right) \tag{2.17}$$

At 2 km baseline, the contribution of the first term, proportional to $\sin^2 2\theta_{13}$ is maximal for 4 MeV neutrinos, and the second term can be neglected. Since P_{ex} is not dependent on the CP–phase, matter effects are negligible at such distances, and Δm^2_{31} is well constrained by atmospheric neutrino experiments, reactor neutrinos provide unambiguous measurement of θ_{13}.

At the end of 1990s, two experiments tested the hypothesis of the neutrino oscillations with reactors with $\sim$1 km baseline: Chooz [45] in the Ardennes (France) and Palo Verde [46] in the Arizona desert (USA).

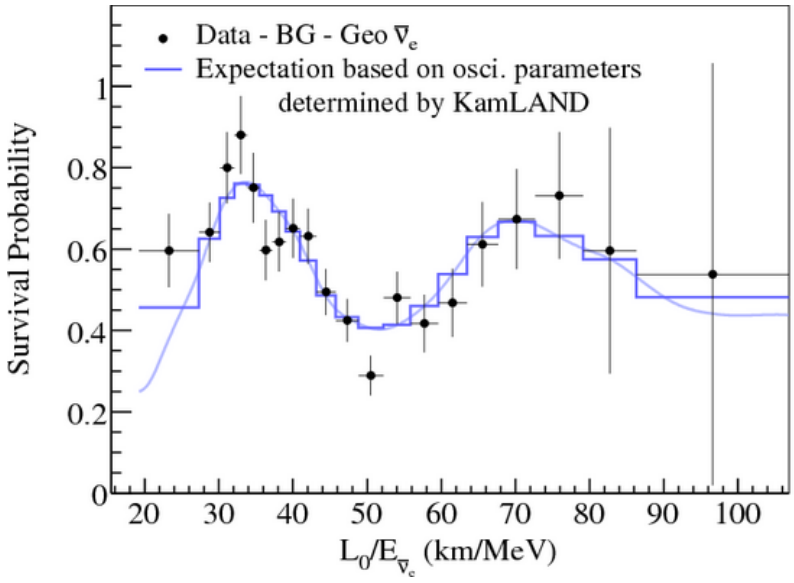

FIGURE 2.12: L/E distribution from KamLAND, after background subtraction, compared with the oscillation predictions [44].

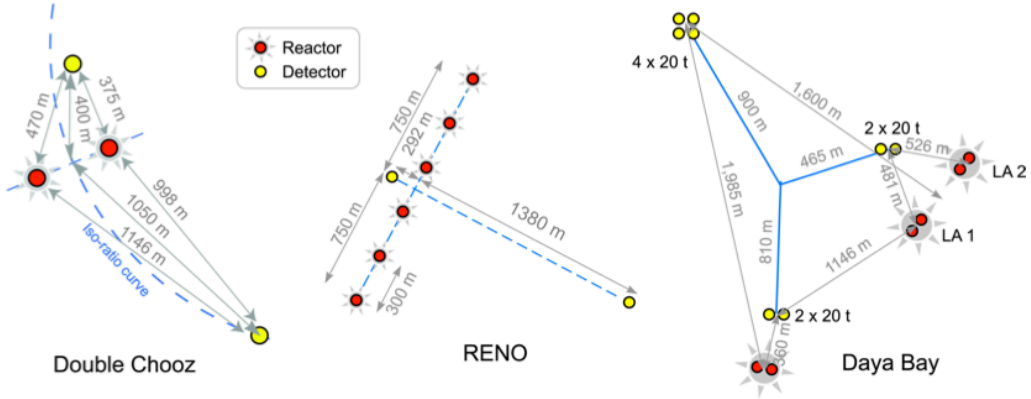

FIGURE 2.13: Long–baseline reactor experiment configurations.

Exeriment	Power [GW]	Baseline Near/Far [m]	Detector Near/Far [ton]	Overburden Near/Far [m.w.e.]
Daya Bay	17.4	360,500/1800	20,20/40	270,300/860
Double Chooz	8.9	400/1050	8.3/8.3	120/300
RENO	16.4	290/1380	16.5/16.5	120/450

TABLE 2.3: Key parameters of the long–baseline reactor experiments

Both used scintillator doped with gadolinium, to enhance the neutron capture. None of them observed neutrino oscillations, and Chooz provided the best constraint on the θ_{13} mixing angle: $\sin^2 2\theta_{13} < 0.14$ at 90% C.L.. The main limitation of both the experiments came from the systematics, dominated by the reactor flux uncertainties. To overcome this problem, a new class of experiments, Double Chooz [47], Daya Bay [48], and Reno [49], used (or will use in the case of Double Chooz) multiple identical gadolinium–doped scintillator detectors, to measure the flux near the reactors, where the oscillations are negligible, and to compare it with the far detector measurements. The ratio between the far and near rates suppresses most of the systematics and allows to investigate the small mixing angle region, down to $\sin^2 2\theta_{13} \sim 0.01$. The key parameters of the three long–baseline reactor experiments are quoted in table 2.3. The experiment geometry configurations are shown in figure 2.13.

In 2012, Daya Bay provided the first evidence (5.2 σ) of a non–zero and unexpectedly large θ_{13} ($\sim$9 degree). The result was confirmed by Double Chooz, using the far detector only but presenting the first spectral measurement, and by RENO. Since CP–violation can occur only with a non–zero θ_{13}, the long–baseline reactor result represents a fundamental milestone in the neutrino oscillation sector. Further, a large θ_{13} value will simplify the strategies and setups aiming at exploring lepton CP violation through neutrino oscillation.

Very short baseline ($<$100 m) experiments are aimed to better understand the nuclear reactor models. In 2011, a re–analysis of their overall results [50] suggested that the predicted neutrino flux was underestimated by a few percents, hinting the existence of at least an extra inactive neutrino, said *sterile*. The reactor experiment implications in the sterile neutrino hypothesis will be discussed in section 2.3.4.

2.3.3 Accelerator neutrinos

In 1990s, a set of new long–baseline accelerator experiments (K2K [5], MINOS [6], OPERA [7]) was proposed to clarify the anomaly observed in the atmospheric sector by Kamiokande and IMB, and, later, to confirm the neutrino oscillation discovery by Super–Kamiokande. The aim was to investigate the dominant oscillation channel, $\nu_\mu \rightarrow \nu_\tau$, by looking at the muon neutrino disappearance (K2K [51], MINOS [52]), at the tau neutrino appearance (OPERA [53]), and at the electron neutrino appearance (T2K [54]) in the subdominant $\nu_\mu \rightarrow \nu_e$ channel.

In the K2K experiment, the 12 GeV KEK proton synchrotron produced a muon neutrino beam, with mean energy of 1.4 GeV, which travels for 250 km and is observed by the Super–Kamiokande detector (already described in the atmospheric neutrino section). MINOS, still running, is a 5.4 kton detector consisting of iron planes interleaved with planes of scintillator strips. It reveals higher energy neutrinos ($< E_\nu > \sim 4$ GeV) produced by the 120 GeV Fermilab Main Injector, and with a longer baseline of 735 km. The L/E ratio is optimized to correspond to the first oscillation maximum of atmospheric neutrinos. Both the experiments include a near detector, to constrain the unoscillated beam spectrum and composition. As shown in figure

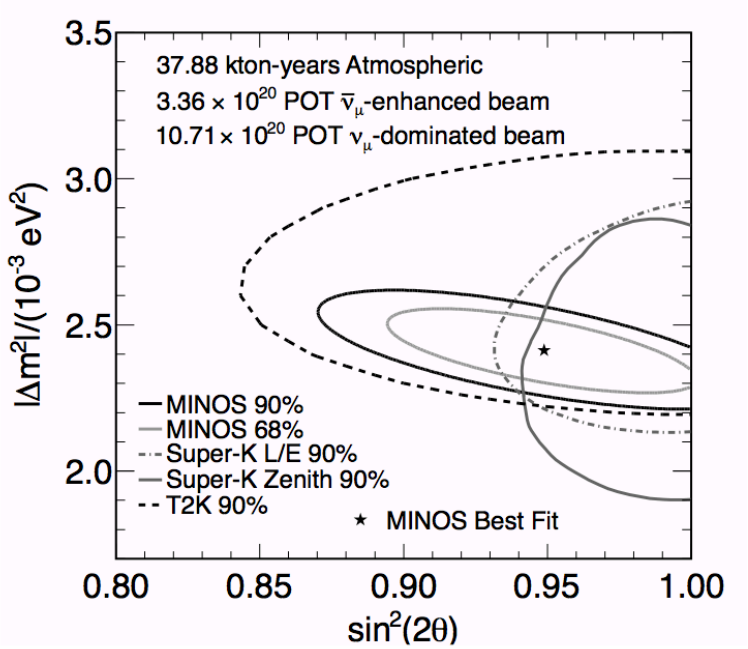

FIGURE 2.14: 90% allowed regions in the (Δm^2_{32}, $\sin^2\theta_{23}$) oscillation parameter plane [52].

2.14, MINOS and K2K results are consistent with each other and with Super–Kamiokande [52]. However, they did not solve the so–called *octant* ambiguity on the parameter $\sin^2 2\theta_{23}$, which can be obtained either for $\theta_{23} < \pi/4$ or for the complementary angle $\pi/2 - \theta_{23} > \pi/4$.

The T2K [54] experiment, follow-up of K2K which ended in 2004, started the data taking in 2010. The novelty is represented by the 30 GeV proton beam, produced at J-PARC and located 295 km away from the detector. The neutrino beam has an off-axis (2.5 degrees) configuration, yielding a quasi monochromatic energy spectrum, around 0.7 GeV, matching the $\Delta m^2_{32} \sim 2.510^{-3}$ eV^2 of the oscillation. In 2013, T2K reported the first observation of electron neutrino appearance (28 neutrinos with an expected background of 4.92 $\pm$0.55 events) in a muon neutrino beam with a peak energy of 0.6 GeV.

OPERA is located in the underground Gran Sasso Laboratory. The detector consists of 1.2 kton of emulsion/lead target, which provides a spatial resolution at the μm scale, needed to observe the $\sim 10^{-3}$ m τ track length, and the following decay. It is exposed to the CERN Neutrinos to Gran Sasso beam, with a baseline of 730 km and a mean energy of 17 GeV, chosen at the maximum of the ν_τ charge current production rate. OPERA directly observed two tau neutrinos in the 2008–2011 data sample, providing a significance for the $\nu_\mu \to \nu_\tau$ oscillation of of 2.4 σ [53].

Short baseline accelerator neutrino experiments affect the sterile neutrino problem only and will be discussed in the next section.

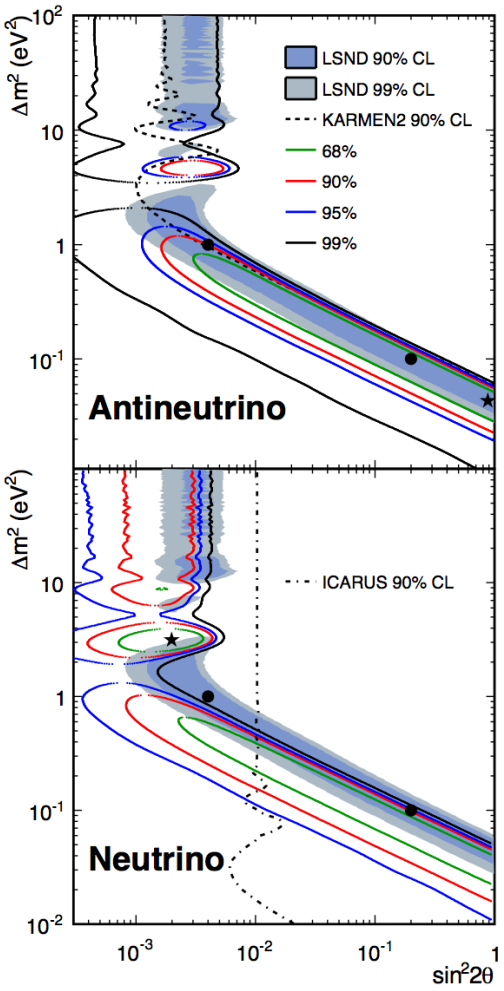

FIGURE 2.15: MiniBooNE allowed regions in antineutrino mode (top) and neutrino mode (bottom) for events with E $>$ 200 MeV [55].

2.3.4 The sterile neutrino hypothesis

Accelerator neutrino experiments at short baseline ($<$1 km) are sensitive to large Δm^2 ($>10^{-2}$ eV^2) and insensitive to the solar and atmospheric mass scales. The beams have energies which range from few tenth of MeV (from the muon decay at rest) to several hundred GeV. These experiments were designed mainly to probe the electroweak physics, the nucleon structure, and to measure the neutrino interaction cross sections. LSND, based on the liquid scintillator technique, observed in 1996 [56] the $\bar{\nu}_\mu$ oscillation in $\bar{\nu}_e$ using the Los Alamos 798 MeV proton beam with a 30 m baseline (E$_{\bar{\nu}}$ $\sim$20–53 MeV). The measured oscillation probability ($\sim$0.26%) corresponds to a Δm^2 in the 0.2–10 eV^2 range, incompatible with both the solar and the atmospheric ones.

KARMEN [57], a LSND-like experiment, with a shorter baseline, 18 m, and, hence a lower sensitivity, did not observed the same effect, ruling out part of the allowed oscillation region. The LSND effect was partially and controversially confirmed by MiniBooNE [55], an experiment specifically designed to verify

LSND. The MiniBooNE target, 800 ton of mineral oil, was illuminated by the Fermilab Booster Neutrino ν_μ beam with energy and baseline of an order of magnitude larger than those of LSND. The data, in the anti–neutrino mode, indicate an oscillation signal region, rejecting the non–oscillation hypothesis at more than 99% CL. The result is consistent with a portion of the region allowed by LSND, as shown in figure 2.15. Working in the neutrino–mode, an excess of ν_e was observed with a significance of 3.4 σ. The MiniBooNE favored neutrino-mode oscillation region covers a very small fraction of the LSND allowed region (figure 2.15).

If these measurements are not due to an artifact, a potential physical solution is represented by extra light ($\sim$ eV scale) neutrinos. Since a fourth light active neutrino is forbidden by the observed Z-boson decay width, the new neutrinos must be *sterile*, that is with no ordinary weak interactions except those induced by mixing. The name sterile was coined by Bruno Pontecorvo in 1967 [58], when he stated that the neutrino oscillations can *convert potentially active particles into particles that are, from the point of view of ordinary weak interactions, sterile , i.e. practically unobservable, since they have the "incorrect" helicity*. Many theories beyond the Standard Model justify the sterile neutrino, often introduced as gauge singlet or right–handed neutrino. In the oscillation theory, sterile neutrinos introduce non–interacting flavors, extending the mixing matrix by additional masses with extra mixing angles, and CP–violating phases. The theory, however, is unable to predict the number of sterile neutrinos, even if there is a general tendency to add three states.

Another result supporting the sterile neutrino hypothesis comes from the several neutrino reactor experiments, which ran over the years, with baselines lower than 100 m. They measured the $\bar{\nu}_e$ flux and constrained the reactor models used to predict the nominal fluxes in the average– and long–baseline experiments, as shown in figure 2.16. In 2011, a new reevaluation [50] of the nuclear reaction models, which included the most recent improved knowledge of the beta decays of the isotopes created in fission reactors, led to an increase of the nominal fluxes. The enhanced predicted flux was in disagreement with the very short baseline measurements by 2–3 σ [50] [59], depending on adopted input parameters, before the θ_{13} measurement. A very recent analysis [60], which includes the results from Daya Bay, RENO, and Double Chooz, lowers the significance to 1.4σ. The deficit, called Reactor Neutrino Anomaly, could be explained by oscillations between active and sterile neutrinos.

A third indication in favor of sterile neutrinos comes from the solar gallium neutrino experiments, GALLEX and SAGE. They were calibrated with intense radioactive sources (^{51}Cr and ^{37}Ar) of neutrinos placed inside the detector. The measured rate was found, in average, to be 2.8 σ below the expected one [61].

The results from the electron neutrino channels are, however, in tension [62] with those obtained by the accelerator experiments in muon neutrino mode, as shown in figure 2.17: the survived parameter region is very narrow and the favored mass splitting is around 1 eV^2. The 3 active + N sterile (with N>1) neutrino oscillation is disfavored mainly by the muon neutrino channel analysis [62].

Other boundaries can be set from cosmological considerations. The sterile neutrino hypothesis has severe implications in the Big Bang Nucleosynthesis and in the Cosmic Microwave Background anisotropy map. Light sterile neutrinos, in fact, could be thermally excited by the interplay of oscillations and collisions, yielding a larger N_{eff}, the effective number of relativistic neutrino degrees of freedom. The standard expectation for this parameter is 3.046, where the 0.046 takes into account effects for the non-instantaneous neutrino decoupling and neutrino flavor. The recent results of Planck [63] improved the constraint on N_{eff} = 3.30$\pm$0.54, which is compatible with both 0 and 1 sterile neutrino. N_{eff}, however, can be considered

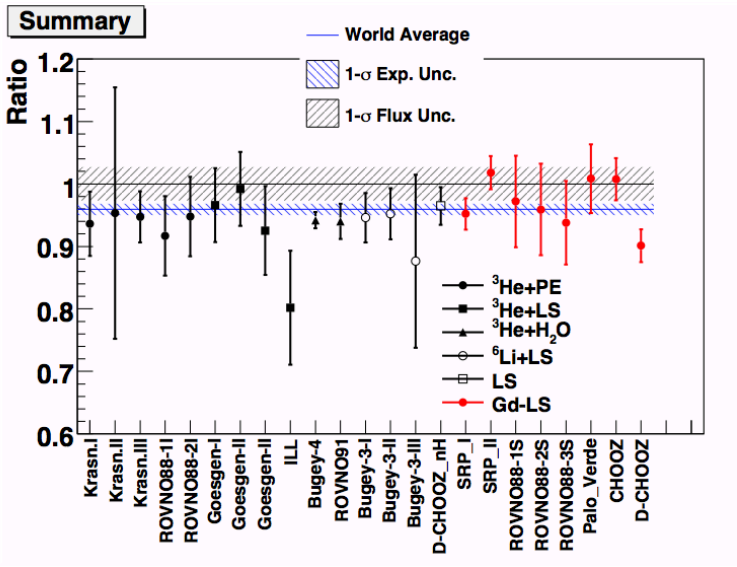

FIGURE 2.16: Experimental and predicted fluxes for very short baseline reactor experiments (form [60]; look herein for the complete list of reactor result references).

a model-dependent parameter. For instance, in several theoretical models neutrinos do not thermalize in the early universe, and the cosmological neutrino abundance would substantially decrease. Planks provides also a further more stringent constraint: assuming a sterile neutrino in association with two massless active neutrinos and a massive one with mass fixed by the atmospheric mass splitting, the sterile neutrino mass must be lower than 0.42 eV at 95% C.L. [64]. This limit is in contrast with the best fitted values from the global analysis of reactor, accelerator, and source experiments.

In conclusion, the sterile neutrino hypothesis is supported by several results, obtained with different techniques and looking at independent signatures. Even if these results are partially controversial, and the final significance can only be addressed as a generic hint of the sterile neutrino existence, they are mostly model–dependent. For this reason, one or more experiments, model–independent, are required, in the near future, to solve this issue.

2.3.5 The current global picture

The experiments described in the above sections provide an almost complete and accurate set of measurements of the oscillation parameters. Solar and long–baseline reactor neutrino oscillations are dominated by the (Δm^2_{12}, θ_{12}) parameters. Atmospheric and long–baseline accelerator neutrinos mainly probe (Δm^2_{13}, θ_{23}). The last parameter, θ_{13}, precisely measured by short–baseline reactor experiments, allows a non–zero CP–violating phase, which is, however, unconstrained. The other unknown parameters are the octant of θ_{23} and the mass hierarchy i.e. the sign of Δm^2 defined as $m^2_3 - (m^2_1 + m^2_2)/2$. Finally, the results from very short–baseline accelerator and reactor experiments, and from the calibration sources used in the solar

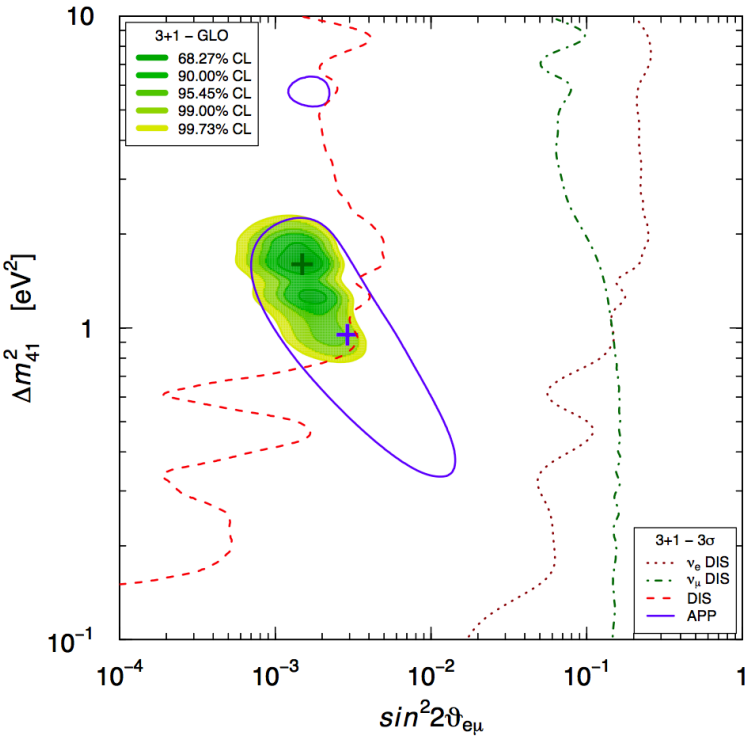

FIGURE 2.17: Allowed regions in the sin2 plane from [62].

radiochemical experiments, hints one or more further oscillation patterns, potentially induced by sterile neutrinos. The most recent values of the oscillation parameters (excluding the sterile neutrino channel), quoted in table 2.4, result from a global three neutrino analysis [65], assuming both the mass hierarchies.

Parameter	Best fit	1σ range
$\Delta m^2_{12}/10^{-5}$ eV^2	7.54	7.32 – 7.80
$\sin^2\theta_{12}/10^{-1}$	3.08	2.91 – 3.25
$\Delta m^2/10^{-3}$ eV^2 (NH)	2.44	2.38 – 2.52
$\Delta m^2/10^{-3}$ eV^2 (IH)	2.40	2.33 – 2.47
$\sin^2\theta_{13}/10^{-2}$ (NH)	2.34	2.16 – 2.56
$\sin^2\theta_{13}/10^{-2}$ (IH)	2.39	2.18 – 2.60
$\sin^2\theta_{23}/10^{-1}$ (NH)	4.25	3.98 – 4.54
$\sin^2\theta_{23}/10^{-1}$ (IH)	4.37	4.08 – 4.96 $\oplus$ 5.31 – 6.10

TABLE 2.4: Oscillation parameter best fits and 1 σ ranges from the global three–neutrino oscillation analysis [65]. Δm^2 is defined as $m^2_3 - (m^2_1 + m^2_2)/2$, with $+\Delta m^2$ for NH and $-\Delta m^2$ for IH.

Section 3

The Borexino experiment

3.1 Overview

Borexino is a real-time liquid scintillator detector, specifically designed to measure the 866 keV ^{7}Be contribution to the solar neutrino flux. The name of the project derived from the use of a Boron compound, trimethylborate, as the liquid scintillator. The goal at that time was to measure neutral– and charged–current reaction of ^{8}B neutrinos interacting with ^{11}B. The design for Borex required a very large fiducial mass, of about 1000 tons, and Borexino was planned as a small-scale prototype. However, it was realized that as long as the low energy background could be reduced, the smaller mass of Borexino would be sufficient to detect the more intense flux from ^{7}Be neutrinos. The ^{7}Be neutrino detection did not require ^{11}B, so the scintillator was changed to pseudocumene (PC) plus a wavelength shifter (PPO), and the focus of the experiment became the reduction of all the possible backgrounds, in particular the unshieldable intrinsic scintillator contamination. In order to meet the requirements for the ^{7}Be neutrino detection, the scintillator had to be purified at unprecedented levels of contamination, requiring uranium and thorium concentrations of 10^{-16} g/g, or smaller, as reported in table 3.1. ^{7}Be neutrinos would be detected via elastic scattering off electrons, and the measured rate would depend on all the neutrino flavors (the cross section for ν_e scattering is $\sim$4.5 times larger than for $\nu_{\mu,\tau}$). The advantage of observing ^{7}Be neutrinos, rather than ^{8}B, was a more robust test of the neutrino oscillations and mixing, thanks to the more accurate neutrino rate prediction by the Standard Solar Model.

Along the description of the Borexino experiment, I will highlight four technical personal contributions (among several others) which I entirely developed and which had a large impact on all the Borexino results:

- the data analysis of the Counting Test Facility to drive the purification R&D;
- the development and tuning of the Borexino Monte Carlo package;
- the energy calibration strategy with gamma sources;
- the cosmic muon rejection with the scintillator detector.

Their impact will naturally arise in the following section, describing the main Borexino results in the solar neutrino sector.

Isotope	Source	Typical conc.	Tolerable level	Strategy
^{14}C	cosmogenic (from ^{14}N)	$\frac{^{14}C}{^{12}C} \leq 10^{-12}$	$\frac{^{14}C}{^{12}C} \leq 10^{-18}$	use petroleum derivate (old carbon)
^{7}Be	cosmogenic (from ^{12}C)	3 x 10^{-2}Bq/ton	$<10^{-6}$Bq/ton	distillation or underground storage of scintillator
^{222}Rn	air and emanation from materials	100 atoms per cm^3 air	1 atoms per ton PC	nitrogen stripping
^{210}Po ^{210}Bi	^{210}Pb on the IV surface			minimum exposure, event position ident.
^{238}U ^{232}Th	suspended dust	2 x 10^{-6}g/g in dust	$< 10^{-6}$g/g in PC	water extraction, distillation
^{nat}K	dust or flour contamination	2 x 10^{-6}g/g in dust	$< 10^{-13}$g/g in scintillator	water extraction
^{39}Ar	air	1.4 Bq/m^3 in Ar	0.1 μBq/m^3 in PC	nitrogen stripping
^{85}Kr	air	1 MBq/m^3 in Kr	0.1 μBq/m^3 in PC	nitrogen stripping

TABLE 3.1: Radiopurity requirements for the Borexino scintillator.

3.2 The Counting Test Facility

When Borexino was proposed, direct radiopurity measurements in scintillators were possible only for small samples and without the required sensitivity for the solar neutrino detection. The Borexino Counting Test Facility (CTF) was a small scale prototype detector designed to verify experimentally the required purity of the organic liquid scintillator, the efficiencies of the purification systems specifically developed for Borexino, and to test the fluid handling operations. The limited dimensions of the CTF did not allow to define a fiducial volume to suppress the external background or to measure the total internal counting rate at the level of ^{7}Be neutrino interactions (0.5 counts/day/ton). Nevertheless, specific analysis techniques were developed to isolate single backgrounds like ^{238}U and ^{232}Th chain Bi–Po delayed coincidences in order to push the CTF sensitivity to $\sim$15 times the neutrino interaction rate, and to overcome to the lack of a fiducial volume definition.

The active detector consisted of $\sim$4 tons of the Borexino-like PC+PPO scintillator, housed by a 0.5 mm thick nylon vessel. The balloon was shielded by 1000 tons of pure water, contained in a cylindrical tank 11 m diameter and 10 m high. An open structure of stainless steel tubes supported an array of 100 photomultiplier tubes (PMTs), at $\sim$3 m from the detector centre.

The first run of CTF started in February 1995, and the detector was active until 2011, after the commissioning of Borexino (2007). I participated to the CTF operations, mainly in the so-called "third campaign" (2001–2006), crucial for the understanding of the initial contaminations in the scintillator from trace radioactive isotopes, like ^{238}U, ^{232}Th, ^{85}Kr and specifically to test the ^{14}C content of the Borexino scintillator delivery. In the same period, I tested the efficiencies of the custom–made purification systems, like nitrogen stripping by adsorption (which I contributed to develop), water extraction, water extraction with nitric acid, distillation, and Silica gel column.

Isotope	Contamination	Comment
^{14}C	(1.60±0.01)×10^{-18} ^{14}C/^{12}C	
^{7}Be	-	below the CTF sensitivity
^{222}Rn	30±3 cpd/100 t	mostly from vessel emanation
^{220}Rn	5.3±2.6 cpd/100 t	
^{210}Po	1085±81 cpd/100 t	
^{210}Bi	-	below the CTF sensitivity
^{238}U	(2.8±0.2)×10^{-16} g/g	from ^{222}Rn analysis and assuming secular equilibrium
^{232}Th	(0.7±0.4)×10^{-16} g/g	from ^{220}Rn analysis and assuming secular equilibrium
^{nat}K	-	below the CTF sensitivity
^{39}Ar	-	below the CTF sensitivity
^{85}Kr	64.2±32.1 μBq/m^3	mostly from vessel emanation

TABLE 3.2: Lowest levels of contaminations measured by CTF.

A day–by–day comprehension of the detector was required in order to measure the initial levels of contaminations and their decay mean times, and the residuals after the purification phases. In this context, I developed a completed set of analytical analysis tools, able to accurately determine the detector response parameters and to identify the contaminants. The light yield represented the primary information, from which depended the capability of identifying all the contaminants, and for measuring possible degeneracies of the scintillator transparency induced by the purification processes. I extracted the light yield, run by run, by fitting the ^{14}C energy spectrum convoluted with the detector resolution, and including the distortion due to the electron quenching.

The accurate measurement of the light yield allowed to define the energy–to–photoelectron conversion and to determine the energy range of the searched contaminants. Most of the analyses relied also on delayed coincidences, like ^{214}Po-Bi (τ=232 μs), ^{212}Po-Bi (τ=431 ns), and ^{85}Kr-^{85m}Rb (τ=146 μs). The first two decay segments belongs to the ^{238}U and ^{232}Th chains, while the third one is a decay branch of the ^{83}Kr one. For the other contaminants, like ^{39}Ar, ^{14}C, and ^{40}K, the identification was based on the spectral fit and on the radial analysis, which was able to disentangle the bulk contamination from the external background. This analysis drove the purification tests, and demonstrated the possibility to reach the levels of contaminations required for the feasibility of Borexino. The only background "out of control" was the α–decay from ^{210}Po, belonging to the ^{238}U chain, whose origin is still not completed assessed. The ^{210}Po represents a puzzle since its rate is largely higher than its "mother" isotope, the ^{210}Bi. The current leading hypothesis is that ^{210}Po is collected by the scintillator in the fluid handling pipelines and transported inside the detector. Another explanation is related to the ^{210}Po's emitted by the nylon vessel and transported toward the centre of the detector by convective currents. In any case, thanks to the exceptional alpha/beta discrimination achievable in the Borexino scintillator, ^{210}Po has been efficiently subtracted from the neutrino signal. An overview of the results from my CTF analyses is reported in table 3.2.

3.3 The Borexino detector

The active target of the Borexino detector, shown in figure 3.1, consists of 300 tons of PC plus 1.5 g/l of PPO. The scintillator is mechanically confined in a nylon spherical "balloon", 8.5 m diameter and 125 μm thick. The material chosen for the nylon vessel had to meet stringent requirements of cleanliness, since it is

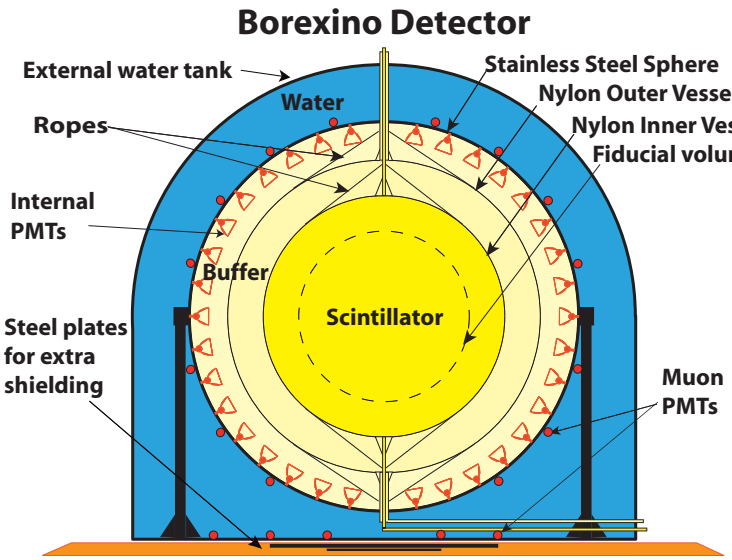

FIGURE 3.1: Sketch of the Borexino detector.

the only component in direct contact with the scintillator (optical clarity, mechanical strength and chemical resistance to the scintillator). A buffer of non–scintillating PC (1000 t) shields the active volume against external background and a second nylon vessel, ∼10 m diameter, avoid that diffused ^{222}Rn may reach the scintillator. The buffer is housed by a stainless steel sphere (13.7 m diameter), where 2200 low background phototubes, 20 cm diameter Thorn-EMI 935, are mounted. About 80& of the PMT's are coupled to light concentrators, specifically designed to increase the collection efficiency from the innermost 3 m radius of the scintillator (the averaged optical coverage is ∼32%).The stainless steel sphere is poured in a cylindrical tank equipped with 200 additional PMT's, aimed to detect the Cherenkov radiation produced by residual cosmic rays, interacting in 2000 m^3 of ultra-pure water.

The PMT's and the dynamic range of the electronics are optimized for fast single photoelectron counting. Precise timing of the PMT's, in fact, is crucial for the spatial reconstruction of each event inside the detector, and for the alpha/beta discrimination which relies on the differences between the characteristic decay times of the scintillator singlet and triplet excitation states. The optical calibration system, which I contributed to develop and install, consists of thin quartz fibers coupled and focused to each PMT, mostly mounted on the concentrator border. The pulse time and gain of each PMT is calibrated by hitting the cathode with laser photons. This operation is performed with a 1 Hz rate along all the data taking period to monitor the detector stability. Special high statistics laser runs are taken, in normal conditions, once per week to calibrate the detector response for physics data. The external muon veto is calibrated with a set of blue light LEDs. Optical sources are also exploited for monitoring the transparency of the scintillator and the buffer liquid.

The energy response of Borexino is related to the charge collected (N$_{pe}$) on the PMT's. The charge is integrated over a time gate of 80 ns, followed by a dead time of 60 ns. After this period, a new gate is ready to register a second pulse. Thanks to its ∼2200 PMT's and to a light yield of ∼500 photoelectrons/MeV, Borexino works, in the sub–MeV energy range, mainly in a single photoelectron regime, which means that

each PMT detects on average much less than one photon hit per event. The energy scale can then be also defined by the number of hit PMT's (N_p), or by counting the number of hits (N_h) on each PMT. A "hit" is defined when the measured charge is larger then $\sim$0.2 photoelectron in the integrated gate of 80 ns. A new hit can be recorded after the dead time of 60 ns. Both N_h and N_p variables are less dependent on the PMT gain and on the single photoelectron distribution with respect to N_{pe}. In particular N_p can be efficiently described in an analytical way by statistical considerations only. Assuming, in fact, $\mu = \frac{N_{pe}}{N_{PMTs}}$ as the average number of photoelectrons detected by each PMT, and the statistics dominated by Poisson fluctuations, N_p corresponds, in a first approximation, to:

$$N_p = -N_{PMTs} \times log(1 - \frac{E \times LY}{N_{PMTs}}) \tag{3.1}$$

where N_{PMTs} is the total number of PMT's, LY the light yield, and E the deposited energy. The three energy variables are used in the Borexino analyses depending on the energy range, being N_p and N_h more accurate at low energies, in the μ<0.25 range, but suffering of non linear effects at higher energies. The accurate knowledge of the three energy scales is achieved by means of Monte Carlo simulations and calibrations, discussed in the next two sections. See reference [68] for more details.

3.4 The Borexino Monte Carlo

The method of evaluation of the detector response function is based on a Monte Carlo that models and predicts the expected shapes of the signal and background. I am the author of the Borexino particle generation and tracking Monte Carlo code (named G4Bx), which is an ab–initio simulation of all the processes influencing the energy deposit of each type of particle in the scintillator and in the materials building the detector. It is important to model the scintillation and Cherenkov light emission, light propagation processes including the scattering, absorption–reemission and reflection, light detection, and the electronics response.

The simulation of the energy deposit uses the standard GEANT4 package [66] describing the energy loss of the various particle types in different materials. The photons of the produced light are tracked one–by–one until they reach a PMT and are possibly detected or until they are absorbed elsewhere. A detailed model of the response of the electronics is also included. Some of the detector parameters correlated with the light generation and propagation, as well as with the electronics response, were measured with dedicated laboratory set–ups. These include the the characteristic scintillation decay times, the PPO and PC emission spectra as functions of the wavelength λ, the PC, PPO, and DMP molar extinction coefficients as functions of λ [68]. The (PC + PPO) refraction index was measured for λ's from 245.5 nm to 600 nm, while for smaller ultraviolet wavelengths we use the values extrapolated by comparison with the results for PC with benzene. The knowledge of the dispersion relation of the refraction index is an important input in the Monte Carlo because it allows to correctly consider the group velocity for individual photons which is important for the light tracking as well as for the simulation of the Cherenkov light emission.

The various PMTs do not have identical probability to produce a signal when a photon hits the photocathode. The PMT quantum efficiencies as λ–functions have been provided by the manufacturer as well as the distribution of the peak quantum efficiency at λ = 420 nm, having a mean value of 24.7% and rms of 1.9%. The Borexino calibration data from mono–energetic calibration sources located in the detector center and

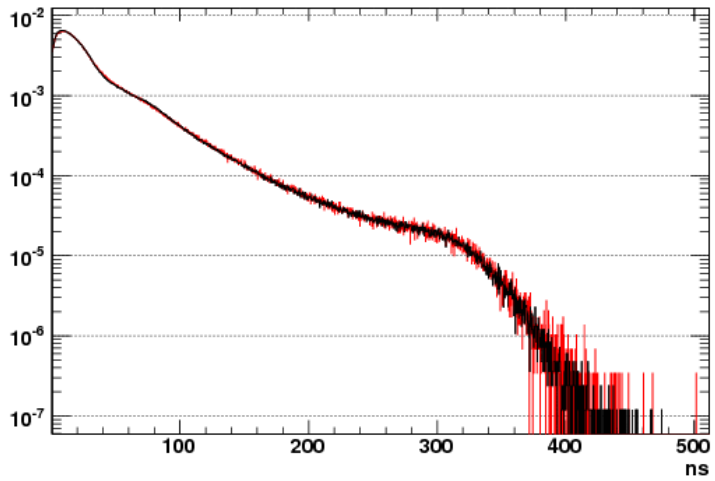

FIGURE 3.2: Data (black) vs Monte Carlo (red) comparison of the pulse shape distribution of ^{14}C events in R<50 cm from the detector center [75].

^{14}C events reconstructed within a sphere of 50 cm radius around the detector center (discussed in section 3.5) show that the quantum efficiency mean value distribution has the rms about 1.5 times larger than that resulting from the nominal ones. In the Monte Carlo we introduce this effect by rescaling the peak value of the quantum–efficiency curve according to the measured efficiency of each PMT.

The simulation reproduces the real distribution of active PMTs, the measured dark noise, and the real gain and the shape of the single–photoelectron response of each PMT following the run–by–run changes. It includes the simulation of the after–pulses and of the measured transit–time spread. The Monte Carlo code finally produces a set of raw data with the same format as that of the measured one, allowing an identical data processing.

It is required that both the energy estimators and the pulse shape distributions (*i. e.* the distribution of the arrival times of the photoelectrons on the PMT's), which are naturally highly correlated, have to be fully reproduced by the simulation. I coordinated the Monte Carlo optimization with an iterative method: several input parameters have been varied until the differences between the measured versus the simulated distributions were minimized. An effort has been made to correctly model all physical phenomena and to minimize the number of "effective" parameters. The accuracy of the Monte Carlo in reproducing the optical effects is at the percent level, as shown in figure 3.2 for the pulse shape distribution of ^{14}C events in R<50 cm from the detector center. The accurate modeling of the optical effects is critical for both the position reconstruction code, which is based on the arrival times of the photoelectrons on the PMT's, after the subtraction of the time of flight, and on the pulse shape discrimination, widely used in Borexino to separate alpha from beta particles.

I dedicated a special effort to the "non-trivial" Monte Carlo description of the quenching of ionizing particles, when part of the deposited energy in the scintillator is dissipated and not converted into light. The quenching effect introduces a non-linearity in the energy response, particularly strong for α particles, protons or nuclear fragments due to the high value of dE/dx. Electronic quenching has also a relevant impact on Borexino analyses being responsible of up to 6% deviation from the linear response at 1 MeV. Further, γ

rays interacting with the scintillator, generate a shower of Compton electrons, which amplify the electronic quenching up to a 10-20% at 1 MeV.

The most diffuse quenching model in literature is the semi-empirical Birks model, dependent on the ionization particle energy loss, dE/dx, and on a constant, the Birks parameter kB, characteristic of the medium. The model links the scintillation light dL produced when a particle looses energy in a distance dx with the stopping power dE/dx:

$$\frac{dL}{dx} = \frac{SdE}{1 + kB \cdot dE/dx} \tag{3.2}$$

where S is the light yield. The Birks parametrization is a macroscopic description of quenching, and can not be used directly in a stochastic approach as in Monte Carlo simulations. In the Birks model, in fact, the quenching effect is obtained by comparing the initial energy of the primary particle with the energy seen by the detector. All depositions of secondaries produced by the primary particle (like delta rays or X-rays) are assumed belonging to the primary. On the other side, in the Monte Carlo approach, each particle is treated independently. A correct parametrization of the Birks formalism requires to conjugate the model in a Geant4 framework, by evaluating the quenching factor for the primary ionizing particle, and inheriting the same factor to each daughter. The ingredients for this simulation approach are: an *a priori* parametrization of the energy loss, required by the Birks equation, and a table of quenching factors as function of the energy, build at the initialization phase, to speed up the simulation. The tuning of the Birks parameter with calibration sources is discussed in the next section.

3.5 Detector calibration

As responsible of the energy calibration, I identified a set of gamma sources, listed in table 3.3 [67], able to map the energy range from ∼100 keV up to several MeV. The radioisotopes were mixed inside 1 cm radius quartz vials, containing a non–scintillating solution, which absorbed most of the β particles. An AmBe neutron source was also inserted to observe gammas emitted from neutron captures on ^{2}H and ^{12}C in the scintillator, and on ^{56}Fe and ^{54}Fe in the steel of the calibration insertion system.

The γ sources placed in the detector center have been used to determine the light yield and the electron quenching parameter kB. The geometry of the γ–source vial has been fully included in the simulation. The γ–sources events have been simulated scanning the values of the light yield S and of kB. The resulting distributions of all the energy estimators have been compared with the measured ones, calculating the χ^2 as a function of S and kB. The value of kB corresponding to the minimum of the χ^2 is (0.0109 $\pm$ 0.0006) cm/MeV. Figure 3.3 shows the comparison between the measured energy distributions of the γ sources and the simulation obtained with the best value of the S and kB. The agreement between the data and the simulation is very good for all the three energy estimators, whose scales are shown in figure 3.4. The peak position and the resolution of the γ source in the detector center are reproduced by the Monte Carlo with an accuracy better than 1%.

The same energy deposits occurring in various detector positions give rise to non–equal, position–dependent values of the energy estimators. This is due to the light absorption, the geometrical effects as for example the presence of the light concentrators mounted on some PMTs, the different response of individual electronics

Isotope	Energy [keV]
^{57}Co	122+14 (89%)
^{57}Co	136 (11%)
^{139}Ce	165
^{203}Hg	279
^{85}Sr	514
^{54}Mn	834
^{65}Zn	1115
^{60}Co	1173+1332
^{40}K	1460
^{241}Am – ^{9}Be: (n,H)	2233
^{241}Am – ^{9}Be: $(n,^{12}$C)	4946
^{241}Am – ^{9}Be: $(n,^{56}$Fe)	7631
^{241}Am – ^{9}Be: $(n,^{54}$Fe)	9297

TABLE 3.3: Gamma sources used in the calibration campaign.

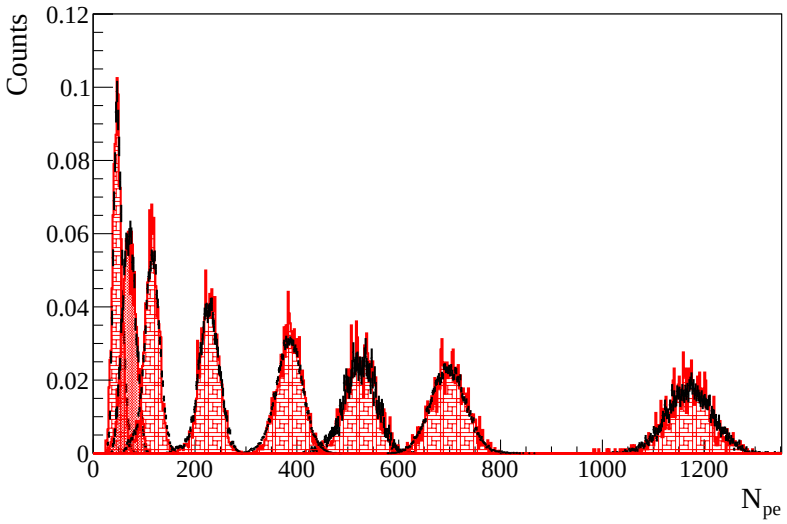

FIGURE 3.3: Data (red) vs Monte Carlo (black) comparison of the peaks from the gamma sources [75].

channels as well as non–uniform distribution of non–working electronics chains. The broken PMTs are concentrated close to the bottom of the detector thus giving a higher light loss for off–center events in the bottom hemisphere with respect to the ones in the upper hemisphere.

The position dependence response calibration was performed by locating the radioactive sources in hundreds different positions inside the scintillator volume. In addition to the already mentioned gamma sources, the position calibration relied on α and β particles from ^{222}Rn and ^{14}C, respectively, in vials filled with scintillators. These sources provide an accurate information on the position thanks to the α and β attenuation lengths, much smaller than the vial size. The vial position itself was accurately measured by means of a LED installed on the arm of the insertion system, detected by several cameras mounted on the stainless steel sphere.

The geometrical non–uniformity of the energy response has been measured with the radon source comparing the energy estimators of the ^{214}Po α–peak of the data and the Monte Carlo. The Monte Carlo data has

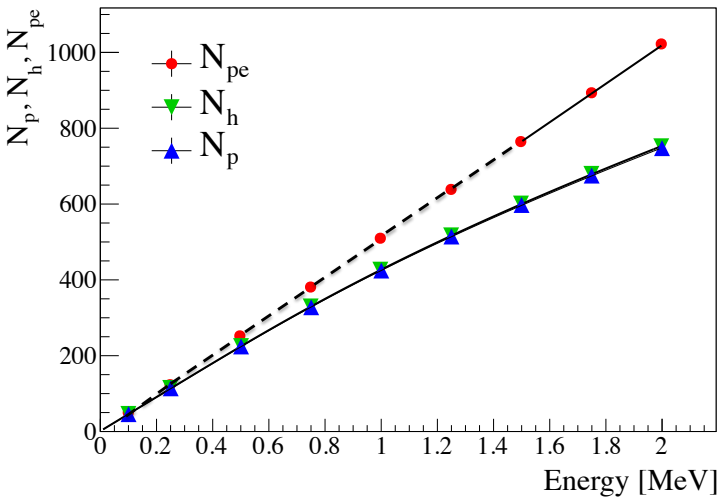

FIGURE 3.4: Borexino energy scales for three variables: the measured charge (N_{pe}), the number of hit PMT's (N_p), and the number of hits (N_h) [75].

been generated with the input parameters optimized to reproduce the source calibration data located in the detector center. As an example, figure 3.5 demonstrates the z–dependency of the N_h estimator both for the data (black circles) and for the Monte Carlo simulation (red stars).

3.6 Rejection of muons with the scintillation detector

Muons are the only relevant component of cosmic radiation penetrating the rock shielding of about 3 800 m.w.e. over the LNGS underground Halls. At this depth, the muon surface flux is reduced to $\sim$1.2 m^{-2} h^{-1}. Due to their mean energy of $\langle E_\mu \rangle \approx$270 GeV, most muons travel through the detector without any significant loss of energy. Muons crossing the scintillator are easily identified since they produce a very large amount of light, correspondent to hundreds of MeV of deposited energy. Even if the limitations of both the PMT's and the electronics cause a distortion of the energy information, the overall collected light is typically above the energy ranges of the neutrino analyses. On the other hand, muons crossing the liquid buffer only represent a critical and dangerous background component, because of the Cherenkov light and the scintillation component produced by the pseudocumene solvent itself. The amount of produced light depends almost linearly on the length of the muon trajectory in the buffer. The corresponding muon signals cover therefore the whole range of solar neutrino recoil energies. Even if the Borexino outer veto suppresses most of these events with an efficiency larger than 99%, the residual component can affect the low flux neutrino analyses, such as the *pep* one.

To reject the residual muon events, I developed an algorithm based on the track length of the events. Electrons from neutrino scatterings or particles from radioactive decays have a track length range from a few micrometers (α's) up to centimeters (γ's), almost point-like with respect to the Borexino size. The correspondent scintillation light propagates as a spherical wave, originated in a single position. Cosmic muons propagate over distances equivalent to the detector size, producing spherical waves of scintillation light all

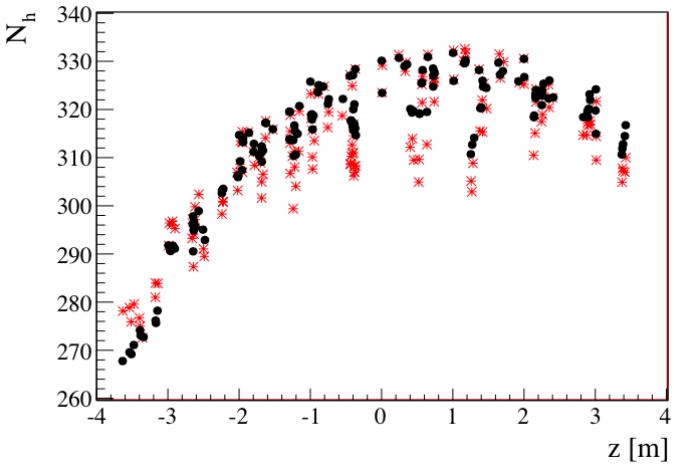

FIGURE 3.5: The N_h peak position vs z-coordinate of the ^{214}Po α peak from the radon calibration source, shown for the data (black circles) and the Monte Carlo simulation (red stars). The various points at fixed z position correspond to different x and y coordinates. The reduction of the collected light for negative z is due to the concentration of broken PMTs close to the detector's "South pole".

along the track. In addition, muons produce a large component of Cherenkov light. The correspondent photoelectron time distribution has mean and peak times delayed with respect to the "point-like" event one. Muons can be then selected with the scintillator detector by exploiting these time features, as shown in figure 3.6 where light blue dots are referred to a clean sample of muons selected by the water detector, and the black ones are neutrino candidates [68]. The red lines represent the muon rejection cuts. Thanks to this algorithm, the scintillation detector is able to reject cosmic muons with almost the same power ($\sim$99%) of the water–based muon veto.

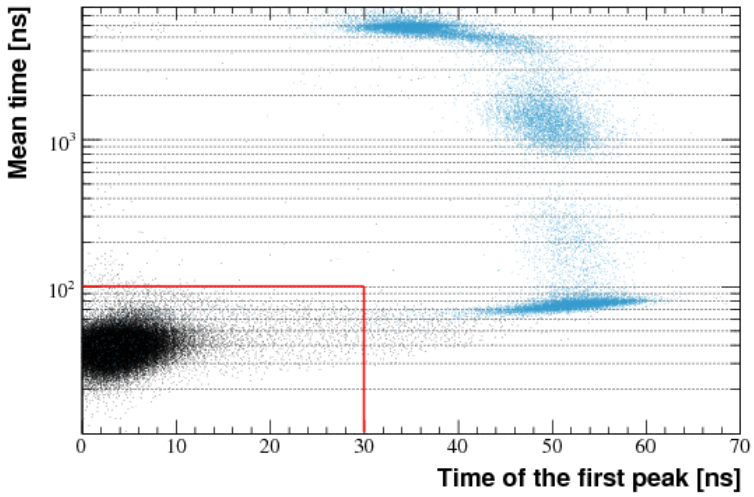

FIGURE 3.6: Mean and peak times of the pulse shape distributions of neutrino-like (black) and muon-like (light blue) events. The red lines represent the cuts applied to identify muons with the scintillator detector.

Section 4

Solar neutrinos with Borexino

I describe, in this section, the four Borexino solar neutrino analyses on ^{7}Be, *pep*, pp, and ^{8}B. As explained in the introduction of this dissertation, I've been involved directly and indirectly in all of them. In particular, I am the author of the entire ^{8}B analysis and I provided two fundamental direct contributions to the *pep* one: the rejection of cosmogenic ^{11}C background via the "three-fold coincidence technique" and the orthopositronium–based pulse shape discrimination.
The pp and ^{7}Be analyses profited of my studies on the background components, and of the calibration and the reconstruction algorithms I provided. In particular, these two analyses are based on fits with probability density functions based on the Monte Carlo I developed. Similarly, most of the efficiencies were evaluated with simulations. The percent–level accuracy reached with the simulations, thanks to the fine tuning of all the optical properties, the quenching effect, and the electronics, provided an extremely powerful tool without which the pp analysis would not be possible. The Monte Carlo of Borexino represents an added–value, from which all the analyses, not only the solar ones, benefitted.

4.1 Solar ^{7}Be neutrinos

Direct Measurement of the Be-7 Solar Neutrino Flux with 192 Days of Borexino Data, Borexino Collaboration, Phys. Rev. Lett. 101 (2008) 091302.

The ^{7}Be neutrino rate was extracted by fitting the energy spectrum of the observed events. The fits have been performed with both the analytical and the Monte Carlo approaches, as shown in figure 4.1. Several background contributions have been included. The dominant ones are: ^{85}Kr, ^{210}Bi, and the cosmogenic ^{11}C. In the analytical approach, ^{210}Po was statistically subtracted because the method was not able to properly describe the non–gaussian tails of the detector response function, not negligible due to the high ^{210}Po rate. On the other side, the Monte Carlo approach is able to reproduce all the detector distortions and to provide also an accurate description of the external background, properly calibrated with an external ^{232}Th source. The Monte Carlo was in fact properly tuned to reproduce all the optical effects occurring in the scintillator, including the absorption and reemission effect of the PPO, the Rayleigh scattering, the pure absorption, and the quantum efficiency. The quenching effect was introduced by adapting the macroscopic

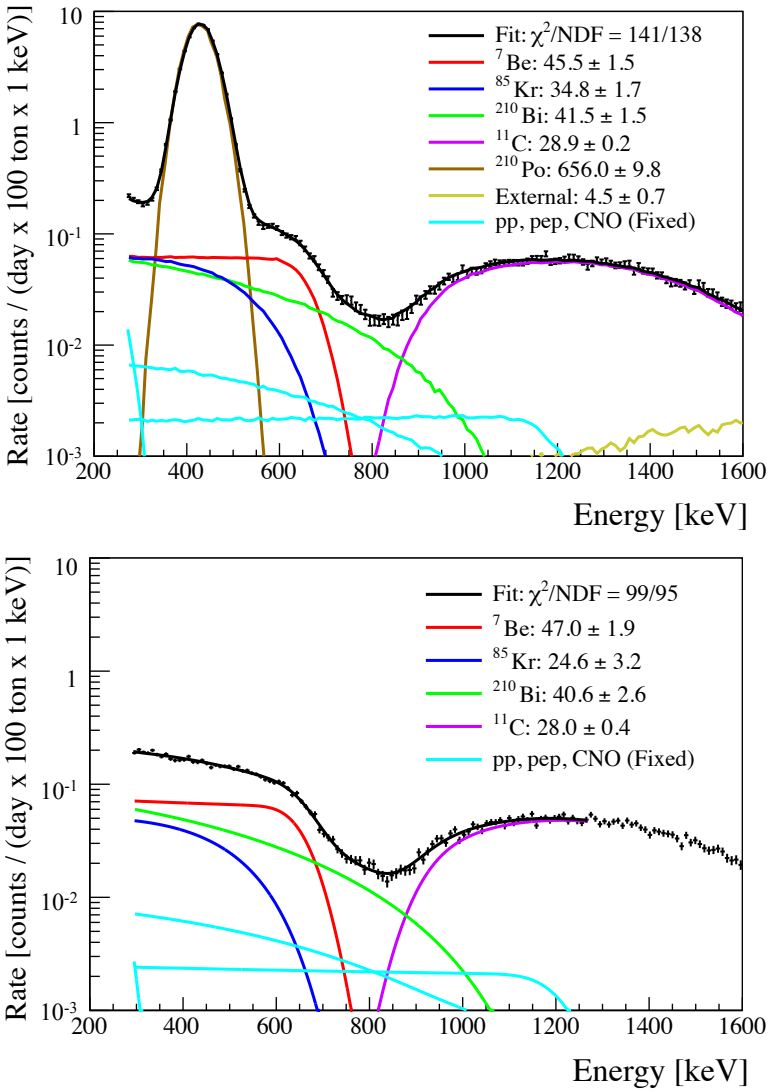

FIGURE 4.1: Spectral fits of the ^{7}Be neutrino data set, with analytical probability density functions (top) and with MC ones (bottom). In the latter, the α contribution from ^{210}Po is statistically subtracted exploiting the α/β discrimination.

Birks model to the Monte Carlo stochastic approach. Further, the Monte Carlo includes also vessel deformation on a week–by–week basis, and the mapping of living PMT's and gains on a run–by–run basis. The contributions from *pep*, pp, and CNO neutrinos have been fixed, in both the approaches, to the predicted central values from the SSM and the MSW-LMA oscillation solution. The systematics were evaluated by comparing the results of the two fitting approaching, by including other possible background contributions, and by varying the energy scale and the definition of the fiducial volume (R<3 m, corresponding to the innermost 100 ton of scintillator) within the uncertainties.

The latest and most accurate measurement of the Borexino ^{7}Be interaction rate was determined to be $46.0\pm1.5(\text{stat})^{+1.5}_{-1.6}(\text{syst})$ cpd/100 ton, with a total uncertainty below 5%. Borexino has also shown that the day–night fractional difference of the ^{7}Be interaction rates is compatible with 0 ($0.001\pm0.012(\text{stat})\pm$

0.007(syst)). The difference could be due to the ν_e regeneration by the matter effect as the neutrinos propagate through the Earth at night, and expected in some regions of MSW parameter space and in some new physics models.

4.2 Solar *pep* neutrinos

First evidence of pep solar neutrinos by direct detection in Borexino, Borexino Collaboration, Phys. Rev. Lett. 108 (2012) 051302.

The electron recoil spectra from *pep* and CNO neutrino interactions have energy endpoints at $\sim$1.2 and $\sim$1.1 MeV, respectively. ^{7}Be neutrinos represent the dominant background, limiting the low energy threshold of observation at $\sim$0.8 MeV. Above this threshold, the main obstacle to the detection of the *pep* and CNO neutrinos is due to the ^{11}C β^+ decays (Q–value = 0.96 MeV). ^{11}C is produced by the interactions of the residual cosmic rays and by their secondaries with scintillator ^{12}C atoms. The ^{11}C high production rate (about 30 cpd / 100 ton), in association with its relatively long mean lifetime ($\sim$30 min), poses a serious problem to the ^{11}C identification and removal. I developed two techniques to efficiently suppress the ^{11}C background: the three–fold coincidence technique, which looks at the neutron emitted in association with the ^{11}C production, and the positronium pulse shape discrimination, which looks at the formation of the ortho–positronium state of the emitted β^+ particle.

4.2.1 The three–fold coincidence technique

Cosmogenic C-11 production and sensitivity of organic scintillator detectors to pep and CNO neutrinos, C. Galbiati, A. Pocar, D. Franco, A. Ianni, L. Cadonati, S. Schonert, Phys. Rev. C71 (2005) 055805.

CNO and pep neutrino spectroscopy in Borexino: Measurement of the deep-underground production of cosmogenic C11 in an organic liquid scintillator, Borexino Collaboration Phys. Rev. C74 (2006) 045805.

Martin Deutsch suggested [69] that the underground production rate for all of the most significant cosmogenic nuclides out of a target mass composed of ^{12}C and ^{1}H could be guessed at from the neutron production rate alone. The list of cosmogenic nuclides produced by interactions with the target ^{12}C nuclide includes ^{8}Li, ^{9}Li, ^{11}Be, ^{8}B, ^{12}B and ^{9}C, all with mean lives below one minute and therefore they can be easily tagged with the parent muon. ^{7}Be is the cosmogenic radionuclide with the longest mean life, 77 days and ^{11}C also poses problems given its 30 minutes mean life. The inclusive cross section for the production of several cosmogenic nuclides in muon-induced cascades was experimentally determined, at 100 and 190 GeV, with a target experiment on a muon beam at CERN [71]. The results showed that ^{7}Be is not among the most likely products of cosmic ray-induced reactions: its production rate at Gran Sasso depth is expected to be less than 0.1 events per day in 100 tons. On the other hand, ^{11}C production rate was estimated in about 15 cpd / 100 ton in the Borexino scintillator at the Gran Sasso Laboratory depth.

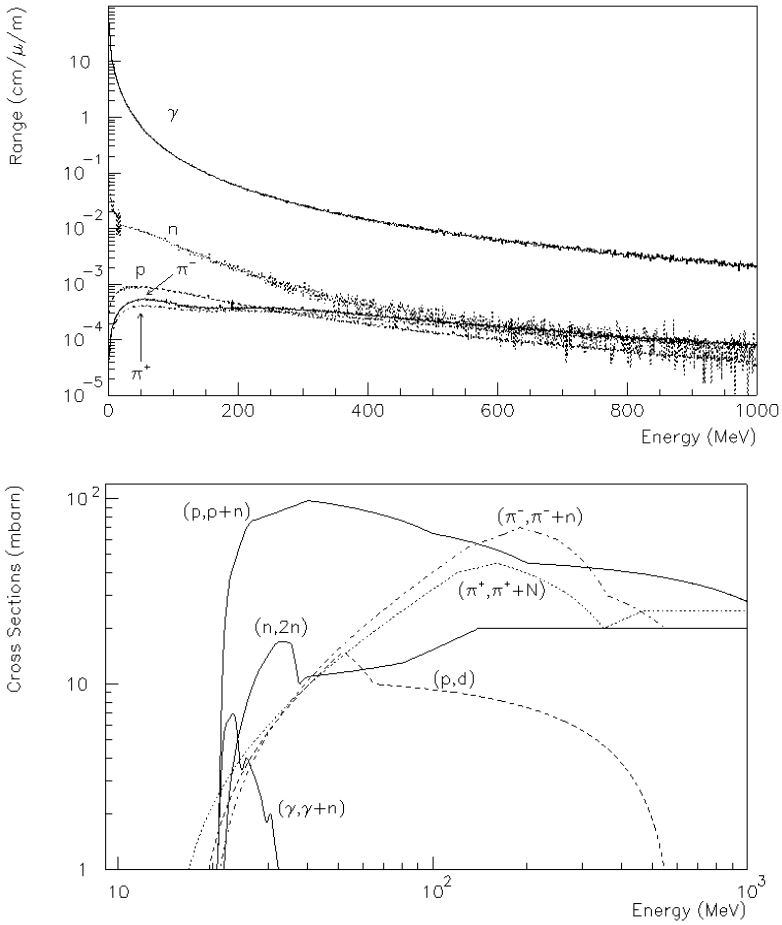

FIGURE 4.2: Cumulative range of secondaries generated in muon-induced showers (top) and cross sections for ^{11}C production as a function of energy (bottom).

Deutsch argued then that most of the ^{11}C isotopes are produced in association with a neutron emission. The detection technique then consists in tagging in sequence the cosmic muon in coincidence with the induced neutron, via capture on protons, the positron emitted by the ^{11}C. To prove his conjectured, I simulated with the FLUKA package the production rates and ranges of all the secondary particles from the μ-induced showers, starting from the energy and angular distribution of the residual muon flux in the Gran Sasso cavern, as measured by the MACRO experiment. The other required ingredients for evaluating the ^{11}C production rate were the cross sections for each production channel, already available in literature. The cosmogenic particle production rates and ranges, as well as the ^{11}C production cross sections, are shown in figure 4.2. To cross-check the robustness of the results, I simulated also the production rates at the energies of the CERN experiment. The so–obtained production rates are quoted in table 4.1. To check the robustness of the results, I simulated also the production rates at the energies of the CERN experiment.

Deutsch's idea of eliminating the ^{11}C events by looking at the three-fold coincidence turns out to be still valid even in presence of invisible channels, as the production rate of ^{11}C nuclides without a neutron in the final state accounts only for $\sim$1 over 20 of the nuclides produced. The definitive proof of the effectiveness of such technique naturally came from the study of the available CTF data, even if the limited size of the

Channel	E_μ [GeV]				
	100	190	285	320	350
^{12}C(p,p+n)^{11}C	1.8	3.2	4.9	5.6	5.7
^{12}C(p,d)^{11}C	0.2	0.4	0.5	0.6	0.6
^{12}C(γ,n)^{11}C	19.8	27.0	34.1	46.6	38.4
^{12}C(n,2n)^{11}C	1.4	2.6	3.8	4.4	4.6
^{12}C(π^+,π+N)^{11}C	1.0	1.8	2.8	3.2	3.3
^{12}C(π^-,π^-+n)^{11}C	1.3	2.3	3.6	4.1	4.2
Invisible	0.9	1.6	2.4	2.7	2.9
Total	25.4	37.3	49.7	54.4	57
Measured	22.9±1.8	36.0±2.3			
Extrapolated			47.8	51.8	55.1

TABLE 4.1: Muon induced production rates for ^{11}C in [$10^{-4}/\mu$/m]. The calculated total production rates are compared with the experimental values available at 100 and 190 GeV, and with the extrapolated values at the mean muon energy for several energy (320 GeV is the mean muon energy in Borexino). The invisible channels rate has been calculated by adding the rate from the ^{12}C(p,d)^{11}C reaction to 2/3 of the rate from the ^{12}C(π^+,π+N)^{11}C reaction.

detector, in comparison with the neutron range, strongly affected the total detection efficiency. Thanks to the "clean" CTF data sample, taken between 2002–2004 without any scintillator/detector operation, I was able to collect enough statistics to provide an unambiguous measurement of the technique efficiency. For each observed neutron, following a cosmic muon, I applied a spherical cut (0.7 m radius) around the neutron capture position, and I collected all the events in the so–defined sphere for about 3 ^{11}C mean lives. Analysing the event time distribution, with respect to the muon one, I observed a decay time compatible with the ^{11}C ones. Correcting the measured rate for the detection efficiency, evaluated with Monte Carlo simulations, and with the random coincidence technique on the data themselves, I found a total production rate in agreement with the predicted one.

The *pep* neutrino analysis on the Borexino data sample was more sophisticate, thanks to an efficient and accurate muon track reconstruction. This allowed to minimize the data loss of the vetoed volume around the neutron capture, by intersecting the "sphere" with a cylindrical volume around the muon track. The overall rejection efficiency was measured in ∼91% with a corresponding data loss of ∼52%, as shown in figure 4.3.

4.2.2 The positronium pulse shape discrimination

Positronium signature in organic liquid scintillators for neutrino experiments, D. Franco, G. Consolati, D. Trezzi, Phys. Rev. C83 (2011) 015504.

The residual ^{11}C events, after the three-fold coincidence technique, were estimated in ∼2.5 cpd / 100 tons, a still too high rate to observe *pep* neutrinos. I then developed an innovative pulse shape technique to separate the ^{11}C emitted positrons from the neutrino-scattered electrons. This technique looks for the formation of the ortho-positronium (o-Ps) bound state, a process competitive to the positron annihilation. In vacuum the o-Ps has a mean life of ∼140 ns. In matter, however, interactions of o-Ps with the surrounding medium strongly reduce its lifetime: processes like chemical reactions, spin-flip (ortho–para conversion at para–

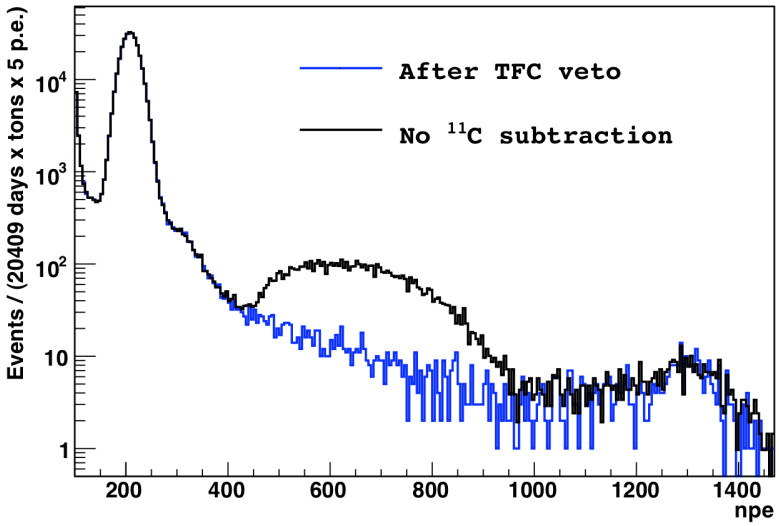

FIGURE 4.3: Borexino energy spectrum before and after the three-fold coincidence technique.

magnetic centers), or pick-off annihilation on collision with an anti-parallel spin electron, lead to the two body decay with lifetimes of a few nanoseconds. If the delay introduced by the positron annihilation lifetime is of the order of a few nanoseconds, calorimetric scintillation detectors, like Borexino, are unable to disentangle the energy deposited by positron interactions from that released by annihilation γ-rays. However, a delayed γ-ray emission, even of a few nanoseconds, induces a distortion in the time distribution of detected photoelectrons (pulse shape), with respect to a direct annihilation event, providing a good signature for isolating β^+ events.

I measured the o-Ps properties in the Borexino scintillator and in the most popular choices of scintillator solvents. I used a PALS (positronium annihilation spectroscopy) technique, which consists of a ^{22}Na source immersed in the scintillator sample, located between two fast detectors (Pilot U plastic scintillator). These are able to measure the time difference between the 1.273 MeV γ emitted by the ^{22}Na source, and one of the γ's induced by the ^{22}Na β^+ annihilation or decay (the 1.273 γ and the positron are emitted simultaneously by the ^{22}Na source). All the samples analyzed were characterized by an o-Ps mean life about 3 ns and a formation probability of about 50%. Such a mean life produces an observable distortion of the pulse shape, as shown with simulated data in figure 4.5, allowing a separation between the residual ^{11}C positron events, and the electrons induced by the neutrino elastic scattering. Further, the discrimination algorithm was "trained" on a pure sample of ^{11}C β^+ events, selected by the three-fold coincidence, and on a pure sample of β^-, from the ^{214}Bi decays, selected in coincidence with the daughter ^{214}Po isotope. The difference in the distributions is shown in figure 4.6.

4.2.3 Multi–dimensional fit

The *pep* neutrino analysis was applied on the data sample after the of the three-fold coincidence cut and it is based on a likelihood approach looking simultaneously at three variables: the energy spectrum, the o-Ps pulse shape discriminator, and the spatial distribution. The latter is fundamental to discriminate the external background from the bulk contamination and the neutrino signal. To cross check the robustness

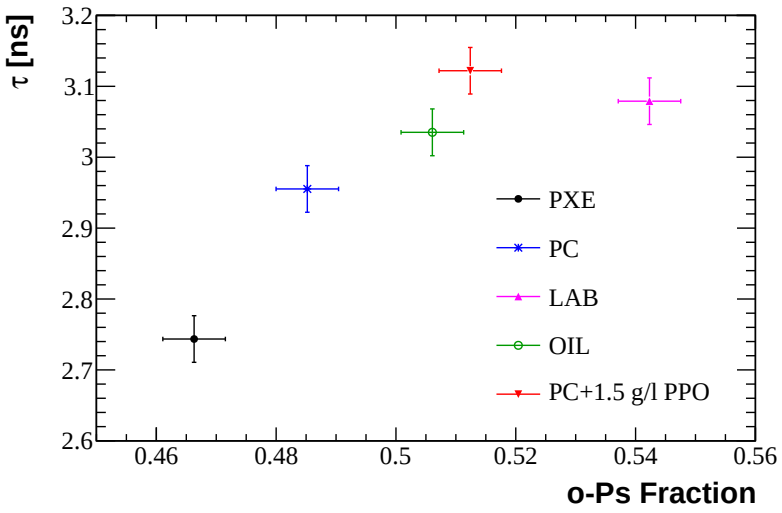

FIGURE 4.4: Results of the o-Ps probability formation and mean life for the analyzed samples of scintillators.

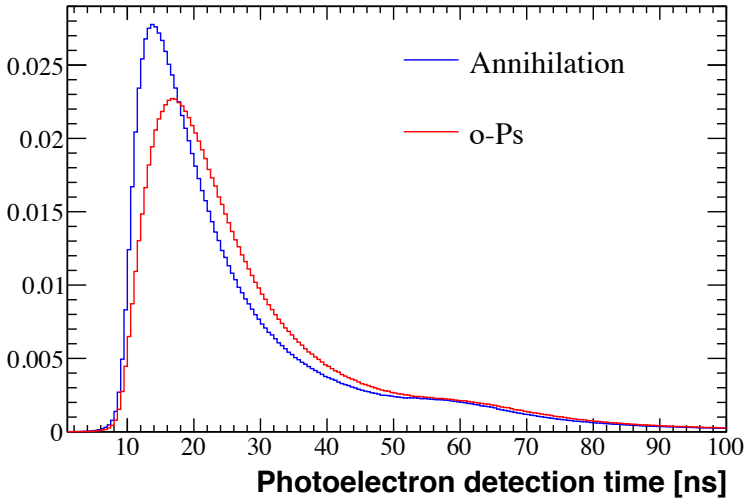

FIGURE 4.5: Borexino simulated photoelectron time distributions, for 0.5 MeV positrons directly annihilating and forming o-Ps.

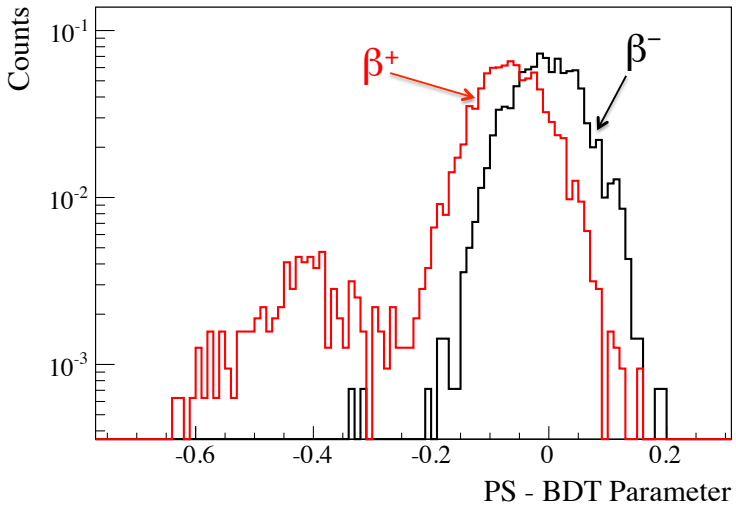

FIGURE 4.6: Pulse shape discrimination variable distributions for ^{11}C β^+ events, selected by the three-fold coincidence, and β^- from the ^{214}Bi events, selected in coincidence with the daughter ^{214}Po isotope.

of the approach, the same method was applied on the three-fold coincidence rejected sample, as shown in figure 4.7. As in the ^{7}Be neutrino analysis, the probability density functions was produced by both Monte Carlo simulations. The systematics are evaluated by comparing the results obtained by varying the number of background components. The *pep* interaction rate was estimated in 3.1±0.6(stat)±0.3(syst) cod / 100 ton. The similarity between the spectral shapes of CNO neutrinos and the background from the ^{210}Bi, did not allow to provide a direct measurement of the CNO neutrino rate, but only to place an upper limit of 7.9 counts cpd / 100 ton, very close to the predictions from the SSM, assuming the MSW-LMA oscillation model.

4.3 Solar ^{8}B neutrinos

Measurement of the solar ^{8}B neutrino rate with a liquid scintillator target and 3 MeV energy threshold in the Borexino detector, Borexino Collaboration, Phys.Rev. D82 (2010) 033006.

^{8}B neutrinos are characterized by an high energy endpoint (∼16 MeV) and a continuous spectrum which make them the ideal candidate to probe the transition region between the vacuum oscillations and the matter–enhanced mixing regime. The excellent radio–purity achieved in the Borexino scintillator allowed to isolate an almost pure sample of ^{8}B neutrino induced electrons, by elastic scattering, with the lowest energy threshold (3 MeV) ever achieved by any other experiment. The 3 MeV threshold approaches the oscillation transition region, where non–standard effects (e.g. oscillation in sterile neutrinos, non-standard interactions) are expected.

As the author of the ^{8}B neutrinos analysis, I set the "direct measurement" of the ^{8}B spectrum as the final goal. "Direct measurement" is here meant to be without any assumption on the spectral shape, and

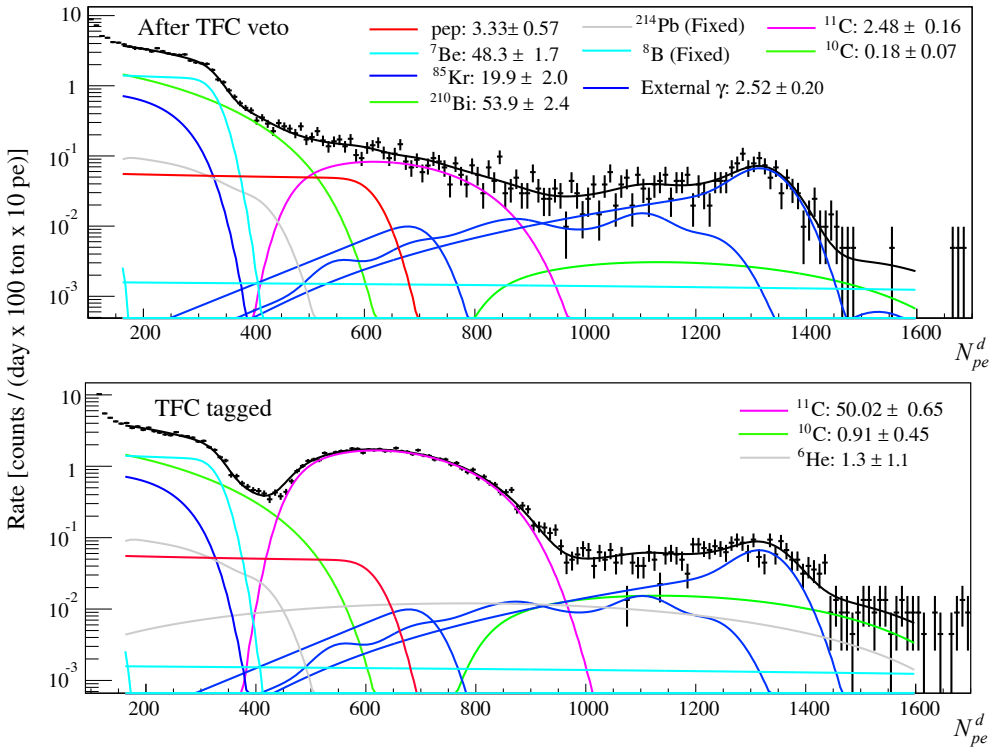

FIGURE 4.7: Energy spectra and results for the best fit in the *pep* neutrino energy range, with Monte Carlo probability density functions.

hence, without assuming neutrino oscillations in order to observe unexpected distortions at low energies. This requirement prevented any spectral fit, and obliged me to identify and reject most of the background components on an event-by-event basis. The residual contaminations had to be statistically subtracted after the accurate determination of their rate. The ^{8}B analysis was then extremely challenging because of the signal-to-background ratio, quantified in ∼1/25,000, before any selection cut.

The threshold at 3 MeV was imposed by the external background from ^{208}Tl, mostly in the phototube materials, which emits 2.6 MeV γ's. Above 3 MeV, the dominant background components are cosmic muons, the particles induced by their showers, and the cosmogenic isotopes, quoted in table 4.2. Muons was rejected by looking the water tank veto, and by developing a special pulse shape analysis with the scintillator detector itself. To reject the shower induced particles, a 2 ms veto was applied after each muon crossing the water tank. 98.3% of the fast ($\tau < 2s$) cosmogenic isotopes was removed by vetoing the detector for 6.5 s after each muon crossing the scintillator. The cosmogenic cut introduces a reduction of the detector live-time of 29.2%. The resulting effective live-time is 345.3 d. ^{10}C was efficiently suppressed by the three-fold coincidence technique, similar to the one applied for the ^{10}C in the *pep* analysis. Cosmogenic ^{11}Be, which has a mean life of ∼20 s, is the only cosmogenic component statistically subtracted. Its rate was measured by analysing the subsample of events defined by a cylindrical volume cut around each muon track, in a time gate of 100 s from the muon itself.

Among the contaminants intrinsic to the scintillator, ^{214}Bi was efficiently detected on a one-by-one event basis, in coincidence with its daughter, the ^{214}Po decay. The residual external background penetrated in the

Isotopes	τ	Q [MeV]	Decay	Expected Rate $> 3\ MeV$ [cpd/100 t]	Measured Rate $> 3\ MeV$] [cpd/100 t]
^{12}B	0.03 s	13.4	β^-	1.25$\pm$ 0.03	1.48 $\pm$ 0.06
^{9}C	0.19 s	16.5	β^+	(1.8 $\pm$0.3)$\times10^{-1}$	(1.7 $\pm$ 0.5)$\times10^{-1}$
^{6}He	1.17 s	3.5	β^-	(6.0 $\pm$ 0.8)$\times10^{-1}$	(5.1 $\pm$ 0.7)$\times10^{-1}$
^{10}C	27.8 s	3.6	β^+	(6.5$\pm$0.5)$\times10^{-3}$	(6.6$\pm$1.8) $\times10^{-3}$
^{11}Be	19.9 s	11.5	β^-	(3.2 $\pm$ 0.5)$\times10^{-2}$	(3.6$\pm$3.5)$\times10^{-2}$

TABLE 4.2: Dominant components of the muon-induced contaminants with Q-value $>$ 3 MeV in Borexino. The expected rate is obtained by extrapolating the KamLAND data at the Gran Sasso mean muon energy [72].

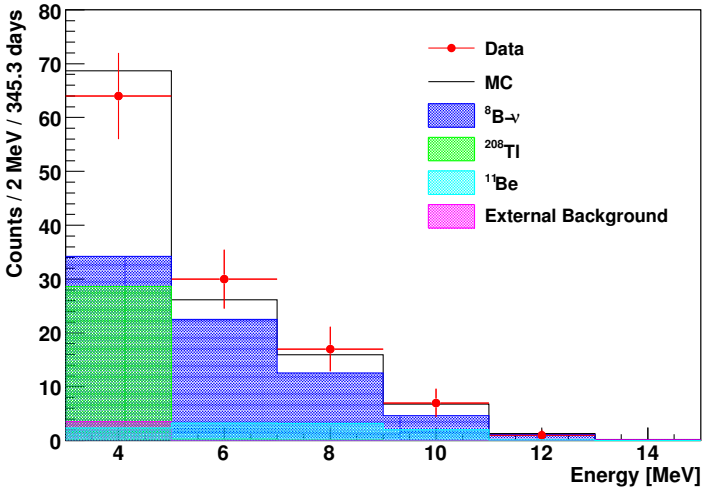

FIGURE 4.8: Comparison of the final spectrum after data selection to Monte Carlo simulations.

fiducial volume (R $<$ 3 m), like the γ's from the neutron captures in the buffer, was estimated by means of a radial analysis. Intrinsic ^{208}Tl is the only intrinsic contaminant that can not be tagged event-by-event. However, its rate can be estimated by looking at the 64% branching ratio of the ^{212}Bi β-decay which goes into ^{212}Po, with a lifetime of τ = 431 ns (^{208}Tl is produced by the competitor 34% ^{212}Bi α-decay branch). The list of cuts and residual count rates are quoted in table 4.3. The data-MC comparison as well as the final spectrum after the residual background subtraction are shown in figures 4.8 and 4.9. The total ^{8}B neutrino interaction rate in Borexino was 0.217$\pm$0.038(stat)$\pm$0.008(syst) cpd / 100 ton for recoil electron energies $>$3 MeV.

4.4 Solar pp neutrinos

Neutrinos from the primary proton-proton fusion process in the Sun, Borexino Collaboration, Nature 512 (2014) 7515, 383.

Cut	Counts 3.0–16.3 MeV	Counts 5.0–16.3 MeV
All counts	1932181	1824858
Muon and neutron cuts	6552	2679
FV cut	1329	970
Cosmogenic cut	131	55
^{10}C removal	128	55
^{214}Bi removal	119	55
^{208}Tl subtraction	90±13	55±7
^{11}Be subtraction	79±13	47±8
Residual subtraction	75±13	46±8
Final sample	75±13	46±8
BPS09(GS98) ^{8}B ν	86±10	43±6
BPS09(AGS05) ^{8}B ν	73±7	36±4

TABLE 4.3: Effect of the sequence of cuts on the observed counts. The expected ^{8}B event counts are calculated from the best parameters for the MSW-LMA [73] and SSM BPS09(GS98) and BPS09(AGS05) [18] [11]

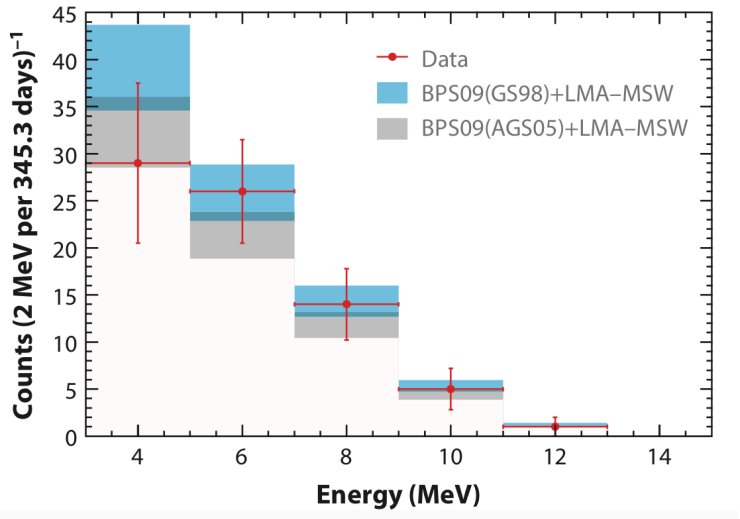

FIGURE 4.9: Comparison of the final spectrum, after the residual background subtraction, with the prediction from the SSM BPS09(GS98) (high metallicity) and BPS09(AGS05) (low metallicity), and from the MSW-LMA neutrino oscillation model.

The pp neutrino analysis is characterized by the low energy of the expected signal (below 400 keV), a region dominated by ^{14}C β events and ^{210}Po α-decays. The selection criteria remove residual cosmic muons, decays of muon-produced isotopes, and electronic noise events, as already explained in sections 4.1, 4.2, and 4.3. Furthermore, a special fiducial mass definition, corresponding to 75.5 ton, was applied to suppress low energy background radiation from external detector components, especially from the "north" and "south" poles of the detector. The spectral model of the ^{210}Po contribution, already discussed in the ^{7}Be analysis, was obtained by Monte Carlo simulations. On the other hand, ^{14}C is responsible for most of the detector triggering rate.

The ^{14}C rate was determined by looking at a sample of random coincidences, dominated by the ^{14}C events, which does not suffer from hardware trigger-threshold effects. Its rate was measured in $\sim$40 Hz, and, thanks to the independent set of random coincidences, its spectral shape well constraint. A so–high rate, however, is responsible of an important pile-up contribution, which occurs when two uncorrelated events are so closely in time that are measured as a single event. The pile-up component was determined independently, by overlapping real triggered events, without any selection cuts, with random data samples. The so-obtained sample was then selected and reconstructed with the same procedure applied to the regular data, in order to include the distortions induced by the reconstruction algorithms.

The solar pp neutrino interaction rate was measured by fitting the energy spectrum (figure 4.10) between 165 and 590 keV. The result is 144 $\pm$ 13 (stat.) $\pm$10 (syst.) cod / 100 ton. The stability and robustness of the measured pp neutrino interaction rate was verified by performing fits with a wide range of different initial conditions. The absence of pp solar neutrinos is excluded with a statistical significance of 10σ.

4.5 The Borexino solar neutrino spectroscopy

Borexino reached its main goal with the 5% measurement of the ^{7}Be solar neutrino rate. Four more measurements beyond the scope of the original proposal were made as well: the first observation of the solar pep neutrinos, the most stringent experimental constraint on the flux of CNO neutrinos, the measurement of the pp neutrinos, and the low-threshold measurement of the ^{8}B solar neutrino interaction rate. The latter measurements were possible thanks to the extremely low background rate above natural radioactivity, while the first two exploited the superior particle identification capability of the scintillator and an efficient cosmogenic background subtraction. All measurements benefit from an extensive calibration campaign with radioactive sources that preserved scintillator radio-purity. All these results are summarized in figure 4.11, showing the expected electron neutrino survival probability and the Borexino measured rates from the different solar reactions. The simultaneous measurements of the ^{7}Be, *pep*, ^{8}B, and pp solar neutrinos make Borexino the only detector able to map the transition between the matter-enhanced and vacuum-driven oscillation regimes in a single experiment.

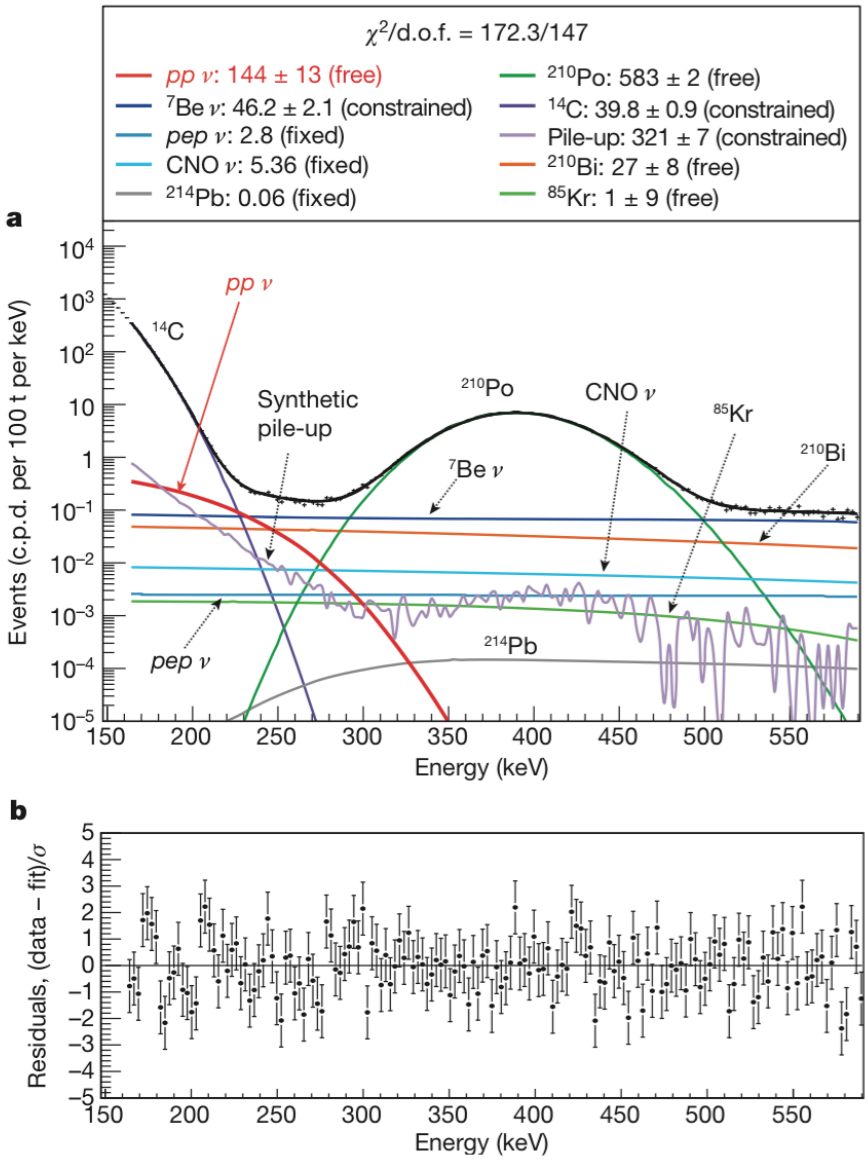

FIGURE 4.10: Fit of the energy spectrum between 165 and 590 keV.

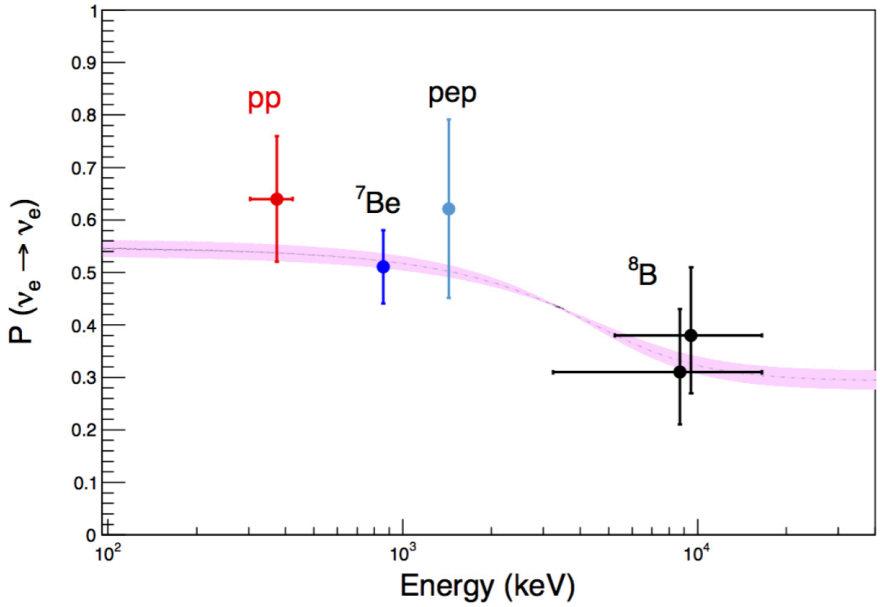

FIGURE 4.11: Survival probability of electron-neutrinos produced by the different nuclear reactions in the Sun and measured by Borexino.

Section 5

The future of Borexino and of solar neutrinos

To date, most of the solar neutrino spectrum has been observed, with the notable exception of neutrinos produced in the ^{13}N, ^{15}O, and ^{17}F reactions from the CNO cycle. A direct measurement of the CNO neutrino components may solve the long-standing and well–known solar metallicity problem. The abundance of the heavy elements, Z (aka metals) in the Sun is a critical parameter in the SSM, since it affects the radiative opacity, and the boundary definition of the convective zone. In particular, abundances of oxygen, carbon, and nitrogen have a direct impact on the energy production of the Sun via the CNO cycle. The SSM predicts different neutrino fluxes if assuming either high–Z [14] or low–Z [15] chemical compositions in the Sun. The largest discrepancy in the prediction of solar neutrino fluxes resides in the CNO component, corresponding to 32%, as shown in table 2.1. A measurement of the CNO neutrino flux at 10-20% accuracy could solve the metallicity problem.

The CNO cycle has also a key role in astrophysics, since it is the dominant source of energy in stars more massive than the Sun and in advanced evolutionary stages of solar-like stars. In addition, constraining the chemical composition of the Sun will improve astrophysical models like for star formation and Super Nova explosion.

In the current experimental framework, the future of Borexino somehow coincides with the future of solar neutrino detection. As already stated in the introduction, in fact, no other running or planned experiment is focused on this physics. The only exception is SNO+ whose however main objective is related to the neutrino-less double beta decay search and will postpone afterward the detection of solar neutrinos.

The importance of the CNO topic has pushed the Borexino collaboration to plan a new purification campaign, scheduled for 2016, to attempt the removal of the ^{210}Bi contamination from thee scintillator, the main obstacle to the measurement of CNO neutrinos. Such a purification campaign represents somehow the ultimate effort to complete the solar neutrino spectroscopy. If the required level of radio-purity will be not achieved, the scientific community may have to develop new techniques and build new experiments (and hence wait several years) before solving the metallicity puzzle with solar neutrinos.

Fortunately, the radio-purity and resolution requirements for the direct dark matter search are similar to (if not more stringent than) those for the solar neutrino physics. The detectors for searching WIMP's are becoming more and more massive, and are approaching the right size (several tons / tens of tons of target mass) to detect also solar neutrinos. In this context, thanks to my experience in the DarkSide experiment, I studied the sensitivity to solar neutrinos of a large (100 tons) mass of liquid argon dual-phase time projection chamber, assuming the technology developed to date for the direct dark matter search. I reported in this chapter the description of my analysis (which is planned to be published at the end of 2015) and the results, which are promising and demonstrate that the two physics sectors can be faced with a unique facility.

At the same time, the exceptional radio-purity and the good knowledge of the detector response make Borexino an ideal facility to test physics channels beyond the solar neutrino physics. Borexino has already provided important contributions to the geo-neutrino sector [76] and to the test fundamental physics laws like the conservation of the Pauli principle [77] and the electric charge conservation [78]. In 2016, Borexino will test the sterile neutrino hypothesis at the eV–scale with an intense source of anti-neutrinos, currently a hot topic of the experimental research which could provide valuable information on the physics beyond the Standard Model.

I have been involved to this project, baptized SOX, since its conception in 2012 contributing to the evaluation of the sensitivity and of the experimental requirements. The difficulty of producing a (anti-)neutrino source at the MCi activity level obliged to investigate different options, which lead to two main candidates: a $\sim$10 MCi ^{51}Cr neutrino source and a $\sim$100 kCi ^{144}Ce anti-neutrino source. The SOX measurement has the potential to clarify the tensions between the different anomalies mentioned in the section 2.3.4 in a relatively short time. I was in charge to estimate the SOX sensitivity with respect to the parameter space region allowed by the reactor and gallium anomalies, and to evaluate the impact of the backgrounds induced by the source itself. I report in the second part of this chapter the results of this analysis.

5.1 Solar neutrino detection in a large volume double–phase liquid argon experiment

Liquid argon (LAr) represents an excellent alternative to organic scintillators for observing CNO neutrinos via elastic scattering. LAr, as a noble gas, does not react chemically, it is resistant to bonding with other elements and it is then naturally radio-purer than organic scintillators. Further, LAr can be purified from ^{222}Rn at the μBq/m^3 level by cryo–adsorption with activated carbons [79].

Double–phase liquid argon Time Projection Chambers (TPCs), which utilizes a LAr target with a gaseous phase on top, have the additional advantage of efficiently rejecting "multiple scattering" events. Double–phase TPCs, in fact, can identify and disentangle, with very high accuracy, energy deposits occurring at a few millimeters along the drift field direction. This allows to discriminate neutrino–induced electrons (single scattering) from gamma particles, and hence also from radioactive decays, like ^{214}Bi from the ^{222}Rn chain segment.

The recent results from DarkSide-50 [80], a 50 kg double–phase TPC designed for direct WIMP detection, witness the excellent performances that this kind of technology can reach in particle discrimination and radio-purity. On the basis of these results, the DarkSide collaboration is proposing a roadmap for the construction of a detector able to reach the so–called "neutrino floor", the irreducible background in the direct

dark matter detection, due to solar neutrino coherent scatterings on argon nucleus [81]. The foreseen exposure of 1,000 ton×year would allow to collect more than 10,000 CNO neutrino events in the entire energy window. Such a detector would also have the capability of observing other solar neutrino components, like ^{7}Be and *pep*, with a more favorable signal–to–background ratio than in Borexino.

In this work, I explored the potential in the solar neutrino sector of future large mass LAr detectors, opportunely designed for direct dark matter search. In particular, I investigated the accuracy on the neutrino rates as a function of the background contaminations, taking into account the detector response and associated systematics.

5.1.1 Neutrino signal and background

The overall expected solar neutrino rate expected in 100 ton of LAr, via elastic scattering off electrons, is ∼150 cpd / 100 ton. However, in LAr, the low energy region (<0.6 MeV) is mostly populated by ^{39}Ar, a β-decaying isotope (Q-value = 0.565 MeV) produced by cosmic ray interactions with natural argon. ^{39}Ar activities in atmospheric argon and in argon extracted from deep underground, naturally shielded against cosmic rays, are ∼1 Bq/kg and <6.5 mBq/kg [82], respectively (the DarkSide collaboration has published very recently a measurement of the ^{39}Ar activity in underground LAr at the level of ∼0.7 mBq/kg [83]). These rates prevent to look for neutrino interactions in the low energy region, mostly populated by *pp* neutrinos. However, ^{7}Be neutrino interactions, whose Compton-like edge is expected at ∼0.66 MeV, are still accessible thanks to the excellent resolution achievable in LAr. This, in fact, is characterized by a scintillation photon yield of ∼40,000 photons/MeV [84], approximately a factor 4 larger than in organic liquid scintillators. A detector able to maximize the light collection efficiency has the potential to reach a resolution of the order of 1% at 1 MeV. DarkSide-50 [80] has already demonstrated, even if in a small scale detector, the possibility to reach a light yield of ∼7000 pe/MeV, with a 200 V/cm field (∼8500 pe/MeV with null field). Also MicroCLEAN [85], a small scale single-phase liquid argon detector, measured a light yield of ∼6000 pe/MeV, in absence of electric field, constant within 2% in the [0.04, 0.66] MeV energy range. Such light yields are approximately 12-14 times the light yield achieved in Borexino (∼500 pe/MeV), the solar neutrino experiment with the best resolution ever reached. Assuming the same resolution of MicroCLEAN and a ^{39}Ar specific activity of 6.5 mBq/kg, no events of ^{39}Ar are expected above 0.6 MeV in 4 years and in a 100 ton liquid argon detector, as shown in figure 5.1. From now on, the energy range of interest of solar neutrinos is defined with a low threshold of 0.6 MeV.

Recent measurements by the GERDA collaboration [86] demonstrated an activity of ^{42}Ar ($\tau_{1/2}$∼33 year), and consequently of its daughter ^{42}K ($\tau_{1/2}$∼12.4 hr), at the level of 94.5±18.1 μBq/kg in natural argon. Both the isotopes are potentially dangerous for a solar neutrino measurement since the Q-values are ∼0.6 and ∼3.5 MeV, respectively. ^{42}Ar can be produced by a two-fold neutron capture process on ^{40}Ar (^{40}Ar(n,γ)^{41}Ar and then ^{41}Ar(n,γ)^{42}Ar) or by spallation reactions from cosmic rays: ^{40}Ar(α, 2p)^{42}Ar [87]. The ^{42}Ar component produced by neutrons has an anthropogenic origin, being mostly produced during nuclear tests in atmosphere. The second component is cosmogenic, induced by cosmic α's, which represent 14% of the cosmic proton flux. Underground argon is not exposed to the nuclear tests, and is then free in anthropogenic ^{42}Ar contamination. Further, the cosmogenic ^{42}Ar component, as discussed in the next subsection, is a negligible background in argon extracted from underground, where the cosmic α flux is strongly suppressed.

The overall expected solar neutrino rate from ^{7}Be, ^{8}B, *pep*, and CNO neutrinos in the [0.6, 1.3] MeV energy range is 4.63$\pm$0.22 cpd/100 ton (5.14$\pm$0.25 cpd/ton) of liquid argon assuming the AGSS09 low–metallicity or LZ [15] (GS98 high–metallicity [14] or HZ) Standard Solar Model and the neutrino oscillation survival probabilities from the MSW-LMA (large mixing angle) solution with $\Delta m^2 = 7.54\times10^{-5}$ eV^2 and $\sin^2(\theta_{12})$ = 0.307 (see table 5.1) [3, 4]. The main contribution, about $\sim$3 cpd/100 ton, is due to the ^{7}Be component, though it is limited in the [0.6, 0.7] MeV energy range, as shown in figure 5.1. The HZ SSM predicts almost equal contributions from *pep* and CNO neutrinos above 0.7 MeV, while *pep* are expected to provide a double contribution with respect to the CNO one in the LZ model. The ^{8}B component is not measurable in the [0.6, 1.3] MeV energy range, since its contribution is negligible and not characterized by a recognizable spectral feature. It may be observed at high energies (>5 MeV) where contaminations from radioactive isotopes are negligible but this is beyond the scope of this work and will be not treated.

The main background components in the [0.6, 1.3] MeV energy range have been identified to have three origins:

- cosmogenic radionuclides produced *in situ* by the interaction of cosmic rays with liquid argon;
- intrinsic contamination of ^{222}Rn, emanated from the detector walls or artificially inserted in the active volume while recirculating gaseous argon;
- external background, *i.e.* gamma's from radioactive contaminants in the detector periphery materials.

Most of these backgrounds are associated to gamma emissions. The dual phase liquid argon TPC technology has the excellent capability to discriminate gamma's with multiple interactions in the active mass. If the interactions occur at a few millimeters of distance along the z–axis defined by the electric field, the associated ionization electrons reach the gaseous region with a delay of few microseconds, generating secondary pulses well separated in time. For instance, assuming an electric field of 200 V/cm, the correspondent drift velocity is $\sim$1 mm/μs: with these parameters, two interactions occurring at 1 cm of distance along the z–axis, generate two secondary pulse of light with a delay of about 10 μs. The characteristic emission times of gaseous argon ($\tau_{fast} \sim 6$ ns and $\tau_{slow} \sim 1.6$ μs) allow to identify the starting time of the pulses with tens of nanoseconds accuracy and to well identify the multiple interactions. Thanks to the capability to discriminate gamma's, most of the above mentioned backgrounds can be efficiently rejected.

Another potential source of background for solar neutrinos is ^{85}Kr (β–decay with a Q-value of 0.687 MeV), whose origin is mostly anthropogenic. Underground argon is expected to be free in ^{85}Kr, but, since this is naturally present in air, it may contaminate LAr during fluid handling operations. However, only $\sim$1% of ^{85}Kr decays have an energy above 0.6 MeV, and even assuming a contamination of a few μBq / ton of LAr, the ^{85}Kr contribution will be negligible with respect to the solar neutrino signal. Further, ^{85}Kr contamination can be directly measured by looking at the secondary decay branch through the metastable ^{85m}Rb level, which provides a clean β–γ coincidence, delayed by $\sim$1.4 μs.

In the next subsections, the contamination from each background source, and the associated residual rate after the multiple scattering cut, will be discussed in detail.

Neutrino Source	Low Metallicity (LZ)		High Metallicity (HZ)	
	All	[0.6-1.3] MeV	All	[0.6-1.3] MeV
pp	107.9 ± 2.0	0	107.0 ± 2.0	0
pep	2.28 ± 0.05	1.10 ± 0.02	2.23 ± 0.05	1.07 ± 0.02
^{7}Be	36.10 ± 2.60	2.85 ± 0.21	39.58 ± 2.85	3.13 ± 0.23
CNO	3.06 ± 0.30	0.64 ± 0.06	4.28 ± 0.44	0.90 ± 0.09
^{8}B	0.30 ± 0.04	0.035 ± 0.005	0.36 ± 0.06	0.042 ± 0.007
Total		4.63 ± 0.22		5.14 ± 0.25

TABLE 5.1: Expected solar neutrino rates per day in an active mass of 100 ton liquid argon, assuming the low-metallicity [15] and high-metallicity [14] Standard Solar Model, and neutrino oscillation in the MSW-LMA [**?**] solution with $\Delta m^2 = 7.54 \times 10^{-5}$ eV^2 and $\sin^2(\theta_{12}) = 0.307$.

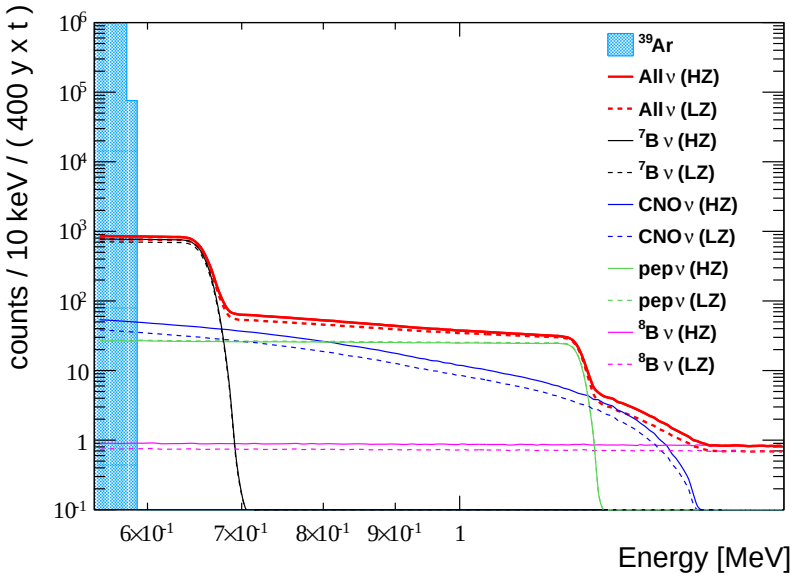

FIGURE 5.1: Solar neutrino spectra, assuming a 1.3% at 1 MeV resolution, correspondent to a light yield of 6 pe / keV. The light blues filled area represents the tail of the ^{39}Ar contamination, intrinsic to liquid argon.

5.1.2 Cosmogenic background

Direct dark matter search experiments are located deep underground to be shielded against the cosmic rays. The residual muon flux, however, may produce radioactive isotopes in muon–induced spallation processes on the argon nuclei, a dangerous electron-like background in the solar neutrino energy window.

Radiochemical and scintillator experiments for solar neutrino physics, like GALLEX and Borexino, have investigated cosmogenic radionuclide productions by means of dedicated setups exposed to muon beams at CERN [88, 71]. Further, radionuclide production models in simulation packages like GEANT4 and FLUKA have been strongly improved in the last years, yielding predictions in agreement within a factor $\sim$2 with the measured values, as shown by the Borexino collaboration in [89] and by the KamLAND one in [90]. We exploited FLUKA for evaluating the cosmogenic production rates, since it has been found in better agreement with the Borexino measurements [89].

The detector geometry described in the FLUKA code consists of a cylindrical TPC of 3.3 m radius and 3 m height, corresponding to ∼150 ton LAr active mass. Laterally the TPC is contained in a 3 cm thick teflon layer, and the top and bottom extremities are covered with 2 mm thick silica layers, representing silica photomultiplier arrays. The gaseous argon region is defined from 2 cm below the upper silica layer (Z_{GAr}). The TPC is contained in a 3 mm thick steel cylindrical cryostat 3.5 m radius and 3.2 m height. Gaseous argon is present also in the cryostat above Z_{GAr}. The cryostat is housed in a Borexino-like detector, being poured in a 6 m radius steel sphere filled with scintillator, in turn housed by a cylindrical tank (10 m height, 11 m diamater) filled with water. In this work, the veto is considered as passive only, despite the detection of light in the scintillator can provide a powerful rejection power against external background. Following the prescriptions of the cosmogenic simulation study for Borexino described in [89], we assumed a cosmic muon flux as measured by the MACRO experiment at the Gran Sasso laboratory ($\langle E_\mu \rangle$ = 283 GeV), with a rate of 1.14 μ / (hr $\times$ m^2) [91] and a ratio between $\mu+$ and $\mu-$ equals to 1.38, as measured by the OPERA experiment [92]. Cosmic muons are generated 3 m above the cylindrical tank on the top of a 0.7 m rock layer, in order to full develop the induced shower. The so-obtained production rates are then converted, isotope by isotope, in specific activities per 100 ton of LAr, taking into account the mean lifetime of each isotope and a data taking of 4 years. The simulation resulted in the production of more than 80 isotopes by muon spallation on argon, as shown in the tables in appendix A. Cosmogenic isotopes produced in the other materials of the detector are taken into account in this analysis, but do not contribute in a significant way to the overall background.

Each isotope has been then generated and tracked with a GEANT4 Monte Carlo, assuming the same geometry as in the FLUKA Monte Carlo, in order to evaluate the efficiency of the multiple scattering cut. A multiple scattering event is conservatively here defined when producing at least two deposits with energy above 10 keV and with a minimum vertical distance between the deposits of 1 cm. This cut is extremely effective in rejecting β^+–decays, which have high probability to produce multiple scatterings thanks to the positron annihilation gamma's, and β^-–decay channels associated with gamma emission. The energy region for solar neutrinos, however, is mostly populated by pure β–decay and the multiple scattering cut rejects only ∼20% of the cosmogenic background, as shown in figure 5.2.

A fraction of cosmogenic isotopes may be further rejected by vetoing the detector after each crossing muon. Conservatively, no time cut has been applied in this analysis, since it depends on the boundary conditions of the experiment, like the muon rate and the event acquisition gate.

The final predicted overall rate, summarized in table 5.2, corresponds to 4.108 cpd / 100 tons in the entire energy range, and 0.733 in the energy region of interest for solar neutrinos. The neutrino signal-to-background rate is estimated to be 6.3 (7) with the low (high) metallicity model. Even assuming conservatively a production rate higher by a factor 2, due to the uncertainties of the FLUKA model, the signal-to-background ratio will be larger than 3, allowing an accurate measurement of the solar neutrino components. The systematics induced by the uncertainties on the cosmogenic isotope activities will be discussed in the next section.

5.1.3 Radon contamination

A ^{222}Rn contamination in the target mass may represent an intrinsic obstacle to the solar neutrino measurements. ^{222}Rn concentration has been measured in several commercial samples of liquid argon by H. Simgen

Isotope	Half life	Decay Mode	Q-value	Rate	
			[MeV]	Entire Range	[0.6-1.3] MeV
^{41}Ar	109.61 min	β^-	2.492	0.213	0.054
^{38}Cl	37.230 min	β^-	4.917	0.815	0.147
^{39}Cl	55.6 min	β^-	3.442	0.173	0.051
^{32}P	14.268 d	β^-	1.711	0.636	0.332
^{34}P	12.43 s	β^-	5.383	0.145	0.021
^{31}Si	157.36 min	β^-	1.492	0.229	0.106
Others				1.897	0.022
Total				4.108	0.733

TABLE 5.2: Activity (cpd/100 t) of single scattering background events from *in situ* produced cosmogenic isotopes, in the whole spectrum, and in the region of interest for solar neutrinos [0.6–1.3] MeV.

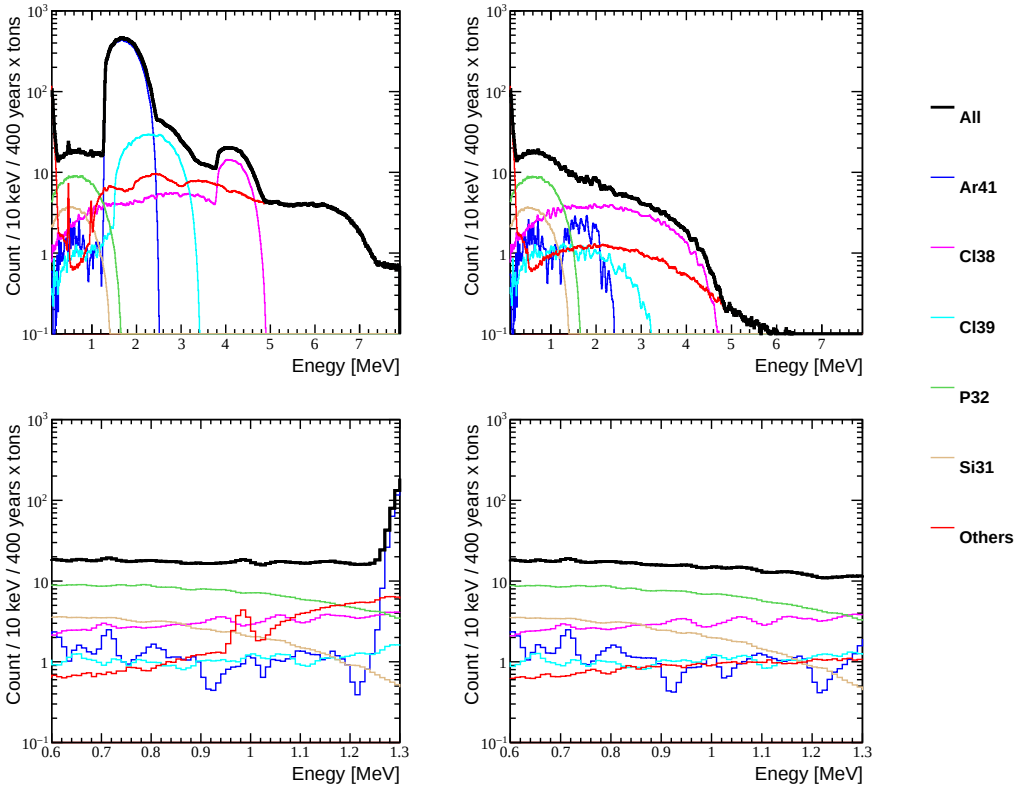

FIGURE 5.2: Spectra of cosmogenic isotope induced background, before (left) and after (right) the multiple scattering cut, in the full energy range (top) and in the solar neutrino energy window [0.6, 1.3] MeV (bottom).

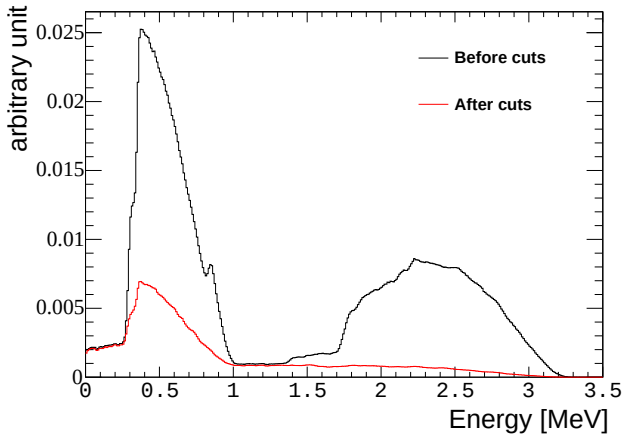

FIGURE 5.3: Contribution from ^{214}Pb and ^{214}Bi from the ^{222}Rn chain segment before and after the single interaction cut.

et al. in [79] with proportional counters. The purest measured sample was found to have to a concentration of 7$\pm$1 μBq / m^3, which corresponds to 500$\pm$71 μBq / 100 ton. ^{222}Rn can be then diffused in the detector target by the circulation loop of the cooling systems. However, cold-charcoal traps inserted in the loop were demonstrated to reduce the radon contamination to fractions of μBq level in 1 m^3 of gaseous argon, corresponding to the maximum sensitivity of the proportional counters used in these measurements (see [79] for more details). Potentially, the cryo-adsorption technique allows to reduce the contamination of ^{222}Rn to less than 1 mBq / 100 ton.

The ^{222}Rn decay segment is responsible of 3 α–decays (^{222}Rn, ^{218}Po, and ^{214}Po) and of 2 β–decays (^{214}Pb and ^{214}Bi). The segment ends with ^{210}Pb, which has a half lifetime of about 22.3 years, and can be considered stable with respect to the 4 years of expected data taking with a 100 ton LAr detector. In LAr, α events are well identified by means of the characteristic light emission pulse shape, and hence rejected. Further, α's are not quenched like in organic scintillators, and lie above the energy region of interest.

The ^{214}Pb and ^{214}Bi decays via β only with 6.3% and 18.2% branching ratios, respectively. The complementary fractions are associated to γ emissions and can be partially discriminated in a double–phase LAr TPC via the multiple scattering cut. The expected total spectrum from the ^{222}Rn decay segment is shown in figure 5.3, before and after the selection cut. Simulating ^{214}Pb and ^{214}Bi in our GEANT4 Monte Carlo setup, we estimated that the fractions of ^{214}Pb and ^{214}Bi falling in the solar neutrino energy region, after the cut, are 6.9% and 5.9%, respectively. With these numbers, a $\sim$45 μBq activity of ^{222}Rn contamination would introduce a background rate equivalent to the expected neutrino signal. Examples of ^{222}Rn contaminations from 10 μBq / 100 ton to 10 mBq / 100 ton are shown in figure 5.4.

^{222}Rn decay rate, however, can be directly measured by the LAr TPC itself by looking at the delayed coincidence between ^{214}Bi and ^{214}Po α–decay ($\tau_{1/2}$ = 163 μs), a technique widely used by several low background experiments (e.g. [75]). ^{214}Bi events can be selected in the [0.6, 3.3] MeV region, free from the ^{39}Ar contamination, and where $\sim$96% of ^{214}Bi decays are expected. An accurate constraint of the ^{222}Rn activity will allow to identify the neutrino spectral shape even with high ^{222}Rn contaminations, as discussed in the next section.

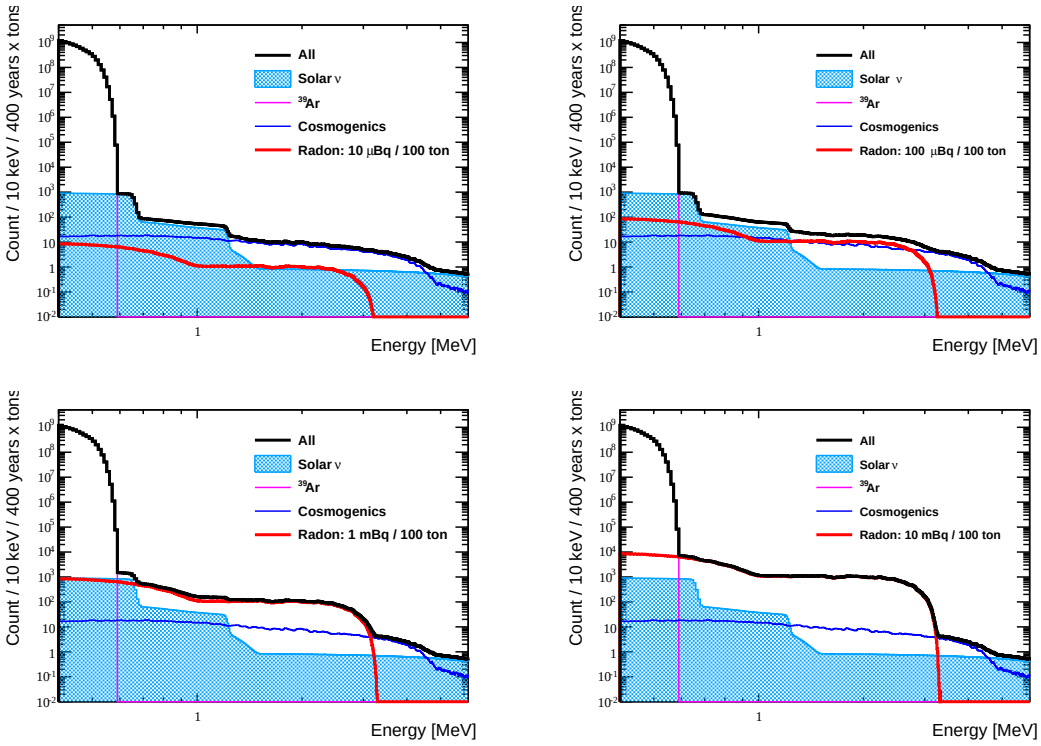

FIGURE 5.4: Overall spectrum expected in 100 tons of liquid argon, with 4 years of data taking, for different concentrations of radon contamination, from 10 μBq/100 ton to 10 mBq/100.

5.1.4 External background

External background refers to particles emitted by radioactive elements in the detector materials like the cryostat and the photosensors. Gamma's are the only particles able to reach the active mass and to produce an electron recoil. Nuclear recoils induced by neutron scattering, in fact, can be identified and discarded thanks to the pulse shape discrimination, whose rejection power has been measured larger than 10^7 in LAr [80].

To evaluate the background induced by external gamma rays, we simulated with GEANT4 [66], ^{40}K, ^{214}Bi and ^{208}Tl from the ^{238}U and ^{232}Th chains originated in the photosensors, and ^{60}C from the cryostat. Rejecting events with the multiple scattering cut, the survival fraction, with respect to the number of generated nuclei, is about a few per mil, as shown in table 5.3. In addition, the survived events are located close to the TPC walls. This allow to perform a fiducial volume cut to further remove them. Fitting the spatial distribution of the survived events, we evaluated an attenuation length varying between 3.6 and 5.1 cm, depending on the source and position. As shown in table 5.3, a fiducial volume cut of 30 cm from the TPC wall would provide a rejection factor of 10^5. Thanks to such short attenuation lengths, the fiducial volume cut can be opportunely tuned to completely suppress the external background.

The contaminations of ^{40}K, ^{214}Bi and ^{208}Tl in photosensors have been reported to be smaller than 0.1 mBq/kg in [93]. In our setup we have simulated a cylinder with a 3.3 m radius with 2 mm width photosensors on the top and on the bottom. This correspond to $\sim$300 kg of silicium and an upper limit on the activity

Source	Origin	Attenuation length [cm]	Survived Fraction without FV	Survived Fraction with FV
^{40}K	Photosensors	3.9	0.3×10^{-2}	0.1×10^{-5}
^{214}Bi	Photosensors	4.2	1.1×10^{-2}	0.9×10^{-5}
^{208}Tl	Photosensors	3.6	0.7×10^{-2}	0.2×10^{-5}
^{60}C	Cryostat	5.1	0.1×10^{-2}	0.3×10^{-5}

TABLE 5.3: Fraction of events producing a single cluster in the [0.6, 1.3] MeV energy range. The last column is referred to a fiducial volume cut applied at 30 cm from the TPC walls.

from photosensors of 30 mBq. Assuming a conservative rejection factor of 10^5 we expect $\sim$0.02 cpd in the [0.6–1.3] MeV energy range being negligible with respect to the solar neutrino fluxes.

The ^{60}Co concentration levels in stainless steel have been measured by Koehler et al. [94] and by Maneschg et al. [95] in different samples in the range of [6.6, 45.5] mBq/kg. Assuming the lowest value in the range, and 1 ton mass cryostat, the overall expected ^{60}C contamination is 570 cpd / 100 ton, and 1.7 cpd / 100 ton after the fiducial volume cut. The latter rate is comparable with the expected signal, making ^{60}Co the most dangerous background among the external sources. Several solutions can be adopted to further reduce the ^{60}Co contribution like a stronger fiducial cut or the identification of a stainless steel batch with lower ^{60}Co contamination. Titanium cryostats represent a natural and radical solution to this problem, being radio-purer than stainless steel and, especially, ^{60}Co–free.

In the sensitivity study described in the next section, we assume negligible the background from external sources.

5.1.5 Sensitivity to solar neutrinos

The measurements of solar neutrino spectral components in a 100 ton LAr dual phase TPC relies on the identification of the spectral shapes. The LAr detector sensitivity to solar neutrinos is estimated using a toy Monte Carlo approach, by fitting 10,000 samples of simulated data, generated with a Poisson statistics corresponding to 400 year $\times$ ton exposure for each metallicity model, and with a detector resolution derived from a light yield of 6000 pe / MeV. The external background is here neglected, since, as discussed above, can be completely suppressed by the fiducial volume cut.
The fitting model has to take into account the large uncertainty related to the knowledge of the cosmogenic background shape. As already mentioned, FLUKA has demonstrated to predict the cosmogenic rates within a factor $\sim$2. Further, the large amount of cosmogenic isotopes, and the extremely low rates of most of them, does not allow to free their amplitudes in the fitting procedure. There is the potential to identify the expected most abundant contribution, the ^{32}P decay (see table 5.2 and appendix A), with an endpoint at $\sim$1.7 MeV. All the other cosmogenics are here modelled with a linear function to avoid any assumption on their spectral shape. The parameters of the linear function are not assumed in the model and free to vary in the fit. The fit is performed with a likelihood approach using the RooFit package [96].

The radon contribution in the toy Monte Carlo samples was varied from 10 to 200 μBq / 100 ton. The ^{214}Bi-Po tagging efficiency was conservatively assumed equal to 60%. The associated uncertainty was used to weight with a Gaussian the radon contribution in the likelihood fitting procedure. The fitting range is extended to 5 MeV with respect to the solar neutrino energy window to better constrain the radon and the

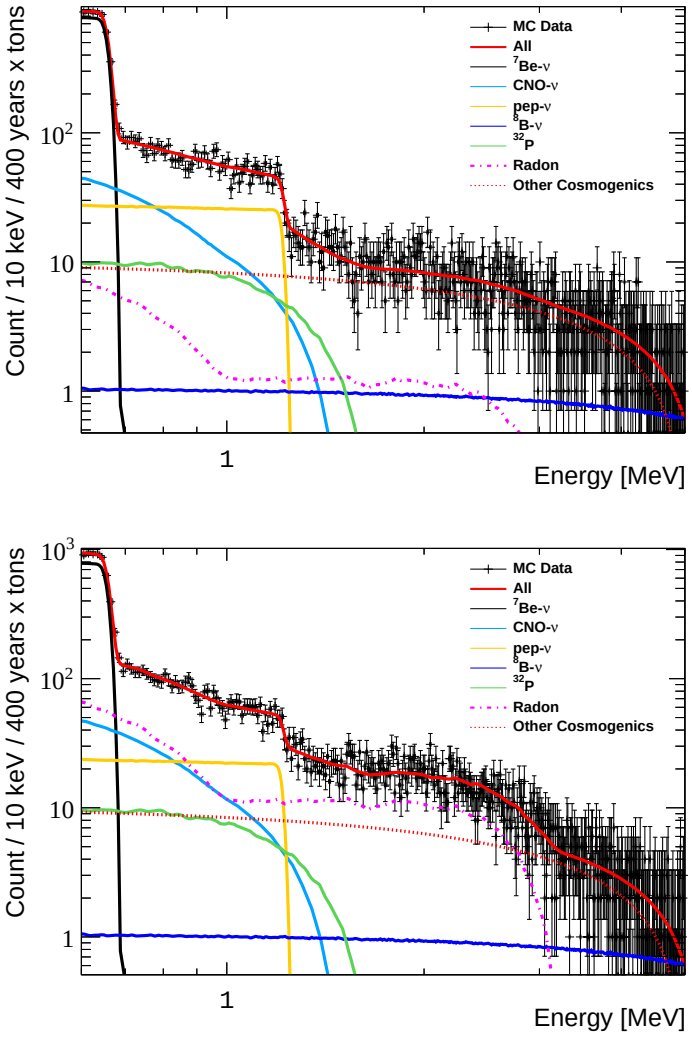

FIGURE 5.5: Examples of fits of toy MC data samples with radon contaminations of 10 (top) and 100 (bottom) μBq / 100 ton. The cosmogenic component, with the exception of the ^{32}P one, is modeled with a first degree polynom.

cosmogenic contributions. Examples of the fits are shown in figure 5.5 for radon contaminations of 10 and 100 μBq / 100 ton. The results of the fits of the toy Monte Carlo samples are quoted in table 5.4.

The CNO spectral shape is similar to the low energy radon component. At a radon contamination of 200 μBq / 100 ton, the fit highlights a systematic deviation from the central value of the CNO component (SSM-LZ) by a few percents. To guarantee a correct CNO measurement, the radon activity must be then reduced below 100 μBq / 100 ton. At the same time, no systematic effects are observed for ^{7}Be and *pep*, whose spectral shapes have clear characteristic features. Further, no differences are observed by assuming either the SSM–LZ or the SSM-HZ model, as shown in figure 5.6.

The impact of a ^{85}Kr contamination was also tested by adding 1 μBq / ton ^{85}Kr events to the toy MC samples. Such a contamination corresponds to $\sim$2% of the ^{7}Be signal above 0.6 MeV. The amplitude of

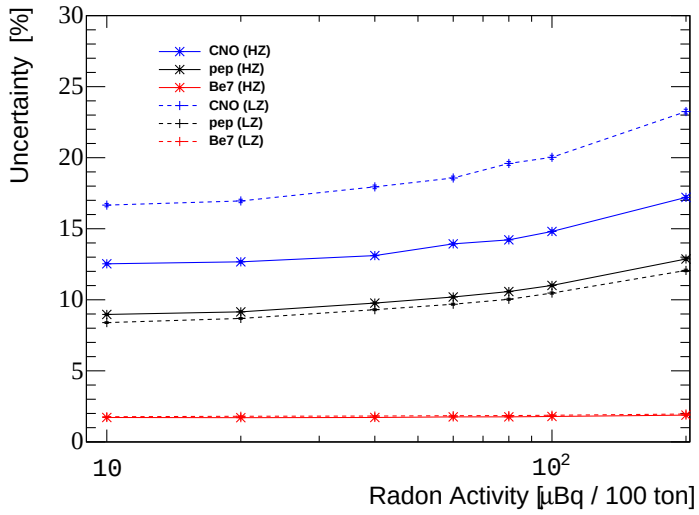

FIGURE 5.6: Statistical uncertainties on the solar neutrino components as function of the radon concentration.

^{222}Rn	Low Metallicity			High Metallicity		
activity	$\sigma(^7Be)$	$\sigma(pep)$	$\sigma(CNO)$	$\sigma(^7Be)$	$\sigma(pep)$	$\sigma(CNO)$
10	1.77 ± 0.01	8.4 ± 0.1	16.7 ± 0.1	1.72 ± 0.01	9.0 ± 0.1	12.5 ± 0.1
20	1.80 ± 0.01	8.7 ± 0.1	17.0 ± 0.1	1.70 ± 0.01	9.1 ± 0.1	12.7 ± 0.1
40	1.82 ± 0.01	9.3 ± 0.1	17.9 ± 0.1	1.72 ± 0.01	9.8 ± 0.1	13.1 ± 0.1
60	1.84 ± 0.01	9.7 ± 0.1	18.6 ± 0.1	1.76 ± 0.01	10.2 ± 0.1	13.9 ± 0.1
80	1.85 ± 0.01	10.0 ± 0.1	19.6 ± 0.1	1.76 ± 0.01	10.6 ± 0.1	14.2 ± 0.1
100	1.87 ± 0.01	10.5 ± 0.1	20.0 ± 0.1	1.79 ± 0.01	11.0 ± 0.1	14.8 ± 0.1
200	1.96 ± 0.01	12.1 ± 0.1	23.2 ± 0.2	1.88 ± 0.01	12.9 ± 0.1	17.2 ± 0.1

TABLE 5.4: Solar neutrino rate uncertainties [%] as function of the ^{222}Rn contamination [μBq / 100 ton]. At radon contamination equal to or larger than 200 μBq / 100 ton, systematic effects on the CNO component become not negligible.

the ^{85}Kr probability density function was added to the free parameters of the fit, without any constraint exploiting the secondary branch, the ^{85}Kr-^{58m}Rb delayed coincidence. No deviations from the results quoted in table 5.4 were observed.

The systematics associated with the linear model of the cosmogenic background shape were also studied. For this purpose, toy MC samples were generated by uniformly varying each isotope cosmogenic activity, from the tables in appendix A, by a factor between 0.5 to 2, with respect to its nominal activity. These samples were produced assuming radon contaminations of 10 and 100 μBq / 100 ton. The found uncertainties are compatible within the errors with the ones reported in table 5.4, demonstrating that the systematics induced by the assumption of a linear model for the cosmogenic shape are negligible.

The expected main detector systematic sources are the energy scale determination and the definition of the fiducial volume to reject external background. The detector response in the [0.6, 1.3] MeV range is expected to be almost linear. In the same range, E. Aprile et al. measured a linear energy response of the liquid argon ionization signal using a ^{207}Bi source with a gridded ionization chamber [97]. The scintillation signal is

expected behaving in the same way, being complementary to the ionization one. Further, the intrinsic ^{39}Ar contamination, with endpoint at 0.565 MeV, offers a precise calibration feature to constrain the energy scale at the sub percent level.

The definition of the fiducial volume does not introduce any systematics by cutting along the axis parallel to the drift field: the drift velocity can be measured with high accuracy and the correspondent spatial precision is at the sub-millimeter level. The dominant source of systematics is expected to be related to the xy–fiducial volume cut, since the position reconstruction on the plane orthogonal to the drift field strongly depends on the granularity of the photosensors on the top of the TPC, and on the diffusion of the ionization electrons. This systematics is expected to contribute to a few percents, not affecting the CNO and *pep* measurements, largely dominated by the statistical errors. It can however affect the ^{7}Be, due to the potential high accuracy ($\sim$1.7%) achievable on its measured rate.

5.1.6 Results

A dual–phase LAr TPC, with 100 ton fiducial mass, was here demonstrated to have the potential to reach high accuracies in the measurements of solar neutrino rates. In particular, it will improve, in 4 years, the precision of the ^{7}Be, pep and CNO components at the $\sim$2%, $\sim$10%, $\sim$15% levels, respectively. To date, Borexino provided the best measurements of the first two components (4.6% and 21.6%), and the best upper limit for the CNO [75].

The CNO measurement, in particular, will provide the first direct observation of neutrinos from the CNO cycle, with the potential to discriminate between the two metallicity SSMs. Following the same approach used in [98], the 15% precision on the CNO rate would improve the determination of the C and N contents in the Sun at 16.5% level, currently measured at $\sim$25% level.

Thanks to the precision on the ^{7}Be rate, the S17 nuclear cross section (^{7}Be(p,γ)^{8}B), among the input parameters in the SSM, would be measured at 8% accuracy, compatible with the precision achieved in the direct beam–target measurement [99], and improving the current S17 determination from Borexino using solar neutrino rates ($\sim$12% accuracy) [98].

In conclusion, a large volume LAr TPC, specifically designed for direct dark matter search, can also provide a rich set of physics results in the solar neutrino sector, by both improving the precision on the ^{7}Be and pep components, and with the potential of the first observation of the CNO component.

5.2 SOX: Sterile neutrinos Oscillation with BoreXino

SOX: Short distance neutrino Oscillations with BoreXino, Borexino/SOX Collaboration, JHEP 1308 (2013) 038.

The sterile neutrino hypothesis, already discussed in section 2.3.4, will be tested by placing an intense source of neutrinos next to the Borexino detector. Such a measurement met the interest, and required the efforts of, a larger collaboration with respect to the Borexino one. For that reason, it has been baptised with the new name of SOX (Short distance neutrino Oscillations with BoreXino). The original plan foresaw

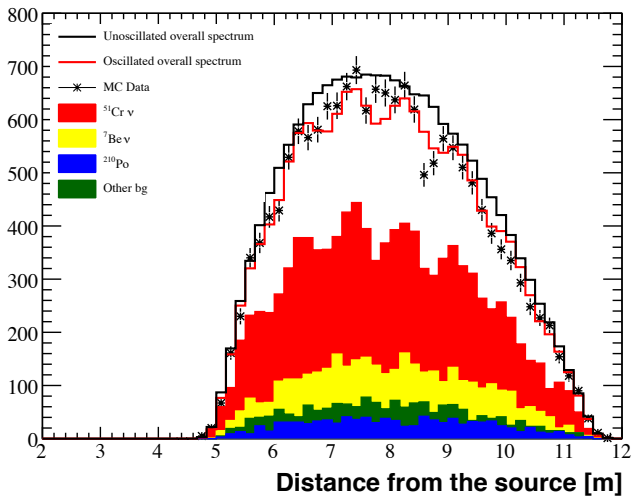

FIGURE 5.7: Example of a possible outcome of the 51Cr experiment (Phase A) with $\sin^2(2\theta_{14})$=0.3 and Δm^2_{41}=2 eV^2. Data points are obtained with a full Geant-4 simulation that was validated at 1% level with calibration sources, including known backgrounds. The signal (red band) is dominating at all distances from the source. The oscillatory behavior allows to reconstruct θ_{14} and Δm^2_{41}.

a staged approach with two sources: the 200-400 PBq activity ^{51}Cr ν_e and the 2-4 PBq ^{144}Ce–^{144}Pr $\bar{\nu}_e$. The Phase A consists in deploying the ^{51}Cr source at 8.25 m from the detector center. The Phase B and C were designed to insert the ^{144}Ce source in the Borexino water tank at 7.15 m from the detector centre and right in the center of the liquid scintillator volume, respectively. The ^{51}Cr source has the advantage to provide a monochromatic neutrino lines of 750 keV (90%) and 430 keV (10%), which facilitate the identification of the oscillation pattern as function of the L/E (distance over energy) variable. The disadvantage is represented by the detection mechanism, which relies on the elastic scattering process and can not be disentangled from the electron-like background, and by the relatively short life time ($\sim$40 days). The ^{144}Ce source provides a continuous anti-neutrino spectrum (end point about 3 MeV and 411 days of life-time), that could suffer of a systematic effect due to the correlation between the energy and the position reconstructions of the neutrino event. On the other hand, anti-neutrinos are detected via inverse beta decay process, and hence looking at the positron-neutron delayed coincidence, which strongly suppresses the background. Further, its long life-time is compatible with a sufficiently long data taking of about 500 days.

I studied the sensitivities for all the three phases in order to define the needed source activity and to evaluate the impact of the systematic uncertainties. For the ^{51}Cr experiment I assumed an activity of 370 PBq and to achieve 1% error in the measurement of the source activity, and 1% error in the knowledge of the fiducial volume. Preliminary analysis has shown that a precision of 1% in the activity might be obtained with a carefully designed and precisely calibrated isothermal calorimeter in which the activity is measured through a very precise knowledge of the heat released by the source. The calorimeter will be designed to allow the calorimetric measurement both during and after the data taking. The fiducial volume determination accuracy is easily achievable with a dedicated calibration campaign.

The sensitivity of the ^{51}Cr source test was evaluated assuming to deploy the source in the tunnel under the detector (8.25 m from the center) and after 6 days from its activation. The advantage of this proposal is that in Borexino the background is already very accurately measured and known, since the source is not

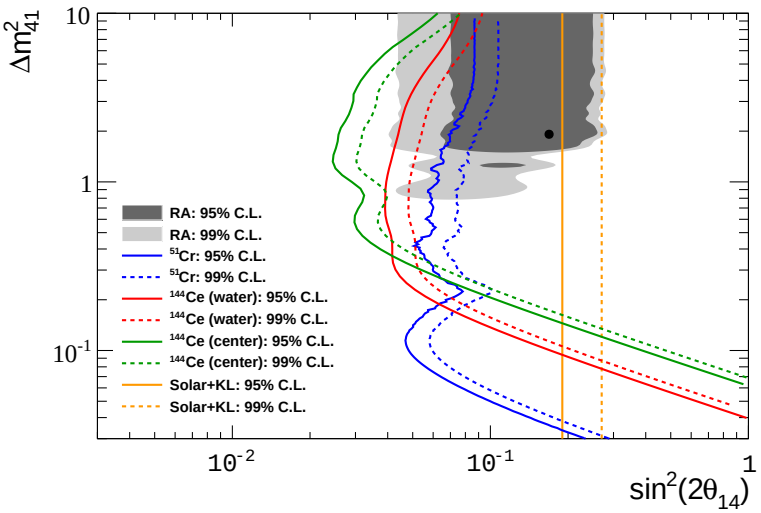

FIGURE 5.8: Sensitivity of the Phase A (^{51}Cr external, blue), of Phase B (^{144}Ce external, red) and Phase C (^{144}Ce center, green). The grey area is the one indicated by the reactor anomaly, if interpreted as oscillations to sterile neutrinos. Both 95% and 99% C.L. are shown for all cases. The yellow line indicates the region already excluded in [74].

in contact with or close to the active mass, and does not induce any further contamination. The expected background components are solar neutrinos (mostly ^{7}Be, which Borexino has accurately measured) and small amounts of radioactive contaminants intrinsic to the scintillator. The latter, in particular, are mostly due to the sizable ^{210}Po (τ = 199.6 days) content of the scintillator, for which we predict at the time of the test a rate of about 11.8 cpd in 133 tons of scintillator (selected as fiducial volume for the measurement), and in the energy region of interest, [0.25–0.7] MeV. The constant background is due to long living (>10 y) isotopes intrinsic to the scintillator, like ^{210}Pb (through the daughter ^{210}Bi) and ^{85}Kr, to solar neutrinos, and to gammas from the detector materials. The overall constant background rate is estimated in 54 cpd/133 ton of scintillator, taking into account the recent achievement in the purification of the scintillator. A detector duty cycle is conservatively assumed at the level of 90%. The signal is extracted by looking for the ^{51}Cr decay mean life (39.966 days) and the oscillation induced distortion in the spatial distribution.

I developed a toy Monte Carlo approach to evaluate the sensitivity. This consists in generating 2000 data samples for each pair of Δm^2_{41} and $\sin^2(2\theta_{14})$ parameters, according to the expected statistics. An example of Monte Carlo data sample is shown in figure 5.7. A period of 15 weeks of stable data taking is assumed before the source insertion in order to accurately constrain the background. The analysis model includes all the known background components, which have been accurately studied and measured from 2007 until now for solar physics, and the non-oscillated signal. I built the confidence intervals from the mean χ^2 for each couple of parameters with respect to the non-oscillations. The result, shown in figure 5.8, demonstrates that the deployment of a 370 PBq ^{51}Cr source at 8.25 m from the Borexino center covers most of the the reactor anomaly region in the (Δm^2_{41}, $sin^2(2\theta_{14})$) parameter space.

For the ^{144}Ce–^{144}Pr experiments we assume instead a 1.5% source intensity precision; furthermore, due to the correlated nature of the signal, we do not consider applying a fiducial volume cut (the whole scintillator coincides with the active volume) and therefore we omit the corresponding error. However, we include

a 2% experimental systematic error, uncorrelated between energy and space bins, to account for residual systematic effects.

The physics reach for the ^{144}Ce–^{144}Pr external (Phase B) and internal (Phase C) experiments, assuming 2.3 PBq (75 kCi) source strength and one and a half year of data taking) is shown in figure 5.8. The χ^2 based sensitivity plots are computed assuming an active radius of 5.5 m, compared to the current active radius of 4.25 m for the solar phase. Such an increase will be made possible by the addition of the scintillating fluor (PPO) in the inner buffer region (presently inert) of the detector. We have also conservatively considered to blind in the analysis a sphere centered in the origin and of 1.5 m radius to reject the gamma and bremsstrahlung backgrounds from the source assembly itself. Under all these realistic assumptions, it can be noted from figure 5.8 that the intrinsic ^{144}Ce–^{144}Pr sensitivity of Phase B covers at 95% C.L. the corresponding reactor anomaly zone, ensuring a very conclusive experimental result even without deploying the source in the central core of the detector. The background included in the calculation is negligible, being represented by about 5 $\bar{\nu}_e$ events per year from the Earth (geo-neutrinos) and from distant reactors, with negligible contribution from the accidentals.

The original SOX plan is recently changed on the basis of the availability of the sources. The difficulties in the 5-10 MCi ^{51}Cr source procurement, and the opportunity presented by the Russian collaborators to double the activity of the ^{144}Ce source, led to the modification of the original plan. The new sensitivity studies demonstrated that a 150 kCi ^{144}Ce source at 8.25 m from the center is almost equivalent to the discussed 75 kCi ^{144}Ce one at 7.5 m (Phase B). At the same time, the ^{144}Ce source will be available already in 2015, contrary to the ^{51}Cr source still under investigation, pushing the collaboration to chronologically invert the deployment of the two sources.

Section 6

Perspectives in the neutrino oscillation physics

The oscillation neutrino physics has still several goals to achieve beyond the already discussed physics of Borexino and SOX. The latest milestone reached in the physics of neutrino oscillations occurred in 2012 with the measurement of the last unknown mixing angle, θ_{13}. Its unexpected large value, close to the Chooz limit, makes CP–violation investigation accessible also in the neutrino sector. Future experiments have to answer to this and to other fundamental questions like the nature (Dirac or Majorana) and the absolute masses of neutrinos. Restricting the field to the oscillations only, the next generation of detectors will attempt to measure the CP–phase, the mass hierarchy, and the θ_{23} octant, and will provide accurate determinations of the other oscillation parameters.

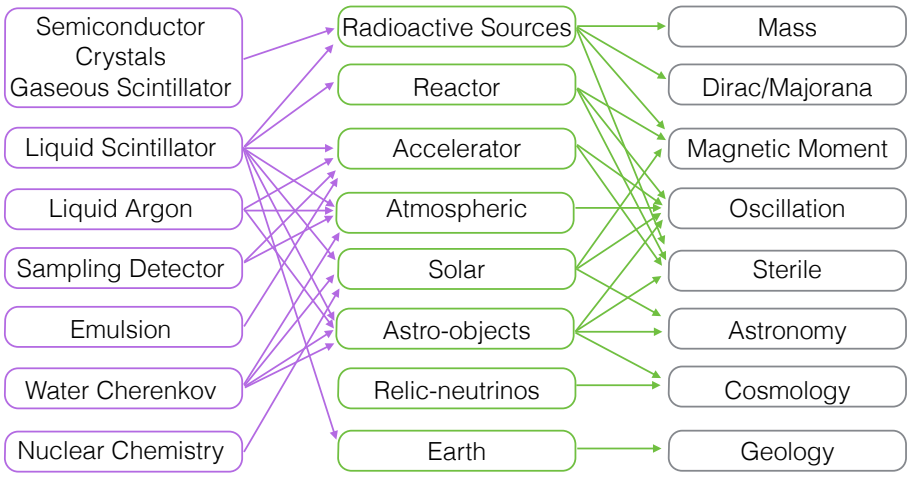

FIGURE 6.1: Neutrino physics problems and the ways to solve them: neutrino sources and detectors..

To achieve these goals, the next generation of detectors will require very high data statistics, commonly translated in an active masses of 1 or 2 orders of magnitude larger than the current generation of experiments. Larger masses will allow to cover also additional physics channels, like geo–neutrino, diffuse supernova neutrino background, and proton decay. The L/E range needed to complete the picture of the oscillation parameters is around 10 km / MeV, commonly fitting the atmospheric neutrino path and long–baseline reactor ($\sim$50 km) and accelerator ($\sim$1000 km) experiments.

Among the non–accelerator neutrino experiments, the most advanced in terms of R&D are JUNO [100], ORCA [101], PINGU [102], and INO [103], all designed to address the correct mass hierarchy. The JUNO detector will house about 20 kton of liquid scintillator under a $\sim$700 m overburden and will be located $\sim$60 km from two nuclear power plants with a total power of 36 GW. This experiment is expected to record 10^5 inverse beta decay events in five years. ORCA and PINGU are Mega-ton Cherenkov atmospheric neutrino detectors, where the active masses consist of sea water and South Pole ice, respectively. They are expected to disentangle the neutrino mass hierarchy in 3-5 years. INO is an iron calorimeter detector consisting of 50 kton of magnetized iron plates arranged in stacks with gaps in between where resistive plate chambers will be inserted as active detectors. INO has the potential to identify the mass hierarchy within 10 years from its commissioning.

The accelerator based experiments will be mainly focused on the CP–violation problem. Even if the mass hierarchy discovery potential is expected to be more powerful than in the non–accelerator case, beam experiments are foreseen to start the data taking approximately 10 years after the non–accelerator experiments. The CP–phase can be identified by exploiting the L/E (neutrino path length to energy ratio) dependence of the appearance probabilities of electron (anti) neutrinos. Neutrinos and anti–neutrinos, in fact, propagate differently through the Earth because of the matter effect, providing a distinct signature for the CP–phase. To date, there are a number of proposed projects for the next generation of accelerator experiments, with different parameter optimization (e.g. neutrino energy, baseline, beam power, and beam direction). In Japan, HyperKamiokande [104] will observe neutrinos with the shortest baseline (295 km, from Tokai to Kamioka) and the largest mass (1 Mton of water, 560 kton of fiducial mass).

Liquid argon TPC is an alternative technique with respect to the water Cherenkov, and is adopted by the Deep Underground Neutrino Observatory (DUNE) at Fermilab, which will observe neutrinos from a new, high intensity, on-axis neutrino beam directed towards a10 kton liquid argon detector located at Homestake with a baseline of 1300 km.

The ambitious future physics program with accelerator and non–accelerator experiments will answer to the three above–mentioned issues: the mass hierarchy, the θ_{23} octant, and, potentially the CP–violation in the leptonic sector. The program will require a considerable effort and time: while non–accelerator experiments are planned to provide a result in a time scale of 5-10 years, accelerator ones will be commissioned only in 15-20 years. In the near future (< 3 years), however, the fundamental issue of the sterile neutrinos will be tackled, with the potential of opening a new door beyond the Standard Model. Several new detectors [105] are, in fact, already in phase of construction, and will investigate the sterile neutrino hypothesis with very short baseline neutrino experiments. There are three main classes of new sterile neutrino experiments:

1. small scale ($\sim$1 ton) segmented detectors, placed near to a reactor core ($<$15 m);
2. large volume ($\sim$100 ton) neutrino experiments observing neutrinos from a very intense source placed at a few meters from the detector center;

3. very large volume ($\sim$1000 ton) detectors illuminated by accelerator neutrinos.

In the first class of experiments, the segmentation is helpful either for observing the oscillation pattern induced by the oscillation in sterile neutrinos, as for the cases of STEREO [105], PROSPECT [106] and DANSS [107], or for discriminating the background (e.g. SOLID). The already described Borexino/SOX [108] is as an example of the second class of detectors. The third class of experiments will exploit accelerator either with muon neutrinos, like in the ICARUS-NESSiE [109] case, to clarify the muon disappearance measurements at small L/E, or with electron anti–neutrinos, like IsoDAR [110]. The latter is an isotope decay-at-rest experiment, which will use an injector cyclotron setup, paired with a $\sim$1 kton scintillator-based detector. The rich program on the sterile will fix the ambiguity on the nowadays controversial results, and has the potential to discover one or more new particles, not explicitly foreseen by the Standard Model of particle physics.

In conclusion, the neutrino oscillation physics program has a clear planning for the next $\sim$30 years, with short–, medium–, and long–term experiments able to fully answer to the remaining questions in the oscillation sector, and to look for new physics beyond the Standard Solar Model.

Appendix A

Cosmogenic isotope production in liquid argon

Isotope	Half life	Decay Mode	Q-value [keV]	Activity [cpd/100 t]
^{6}He	806.7 ms	β^-	3507.8	1.28e-01 $\pm$ 1.25e-02
^{8}He	119.1 ms	β^-	9670.2	9.68e-03 $\pm$ 3.42e-03
^{8}Li	839.9 ms	β^-	12975.2	9.55e-02 $\pm$ 1.07e-02
^{9}Li	178.3 ms	β^-	13606.7	2.06e-02 $\pm$ 4.99e-03
^{11}Li	8.75 ms	β^-	20231.2	1.21e-03 $\pm$ 1.21e-03
^{7}Be	53.22 d	EC	861.815	1.02e-01 $\pm$ 1.08e-02
^{11}Be	13.76 s	β^-	11509.2	8.47e-03 $\pm$ 3.20e-03
^{12}Be	21.3 ms	β^-	11708	2.42e-03 $\pm$ 1.71e-03
^{8}B	770 ms	β^+	14949.8	9.68e-03 $\pm$ 3.42e-03
^{12}B	20.20 ms	β^-	13369.3	3.39e-02 $\pm$ 6.40e-03
^{13}B	17.36 ms	β^-	13437.2	7.26e-03 $\pm$ 2.96e-03
^{14}B	12.5 ms	β^-	20644	1.21e-03 $\pm$ 1.21e-03
^{9}C	126.5 ms	β^+	16494.8	4.84e-03 $\pm$ 2.42e-03
^{10}C	19.290 s	β^+	2929.62	8.47e-03 $\pm$ 3.20e-03
^{11}C	1221.8 s	β^+	1982.4	5.44e-02 $\pm$ 8.11e-03
^{14}C	5700 y	β^-	156.475	8.42e-06 $\pm$ 1.11e-06
^{15}C	2.449 s	β^-	9771.7	1.21e-02 $\pm$ 3.82e-03
^{16}C	0.747 s	β^-	7891.58	1.21e-03 $\pm$ 1.21e-03
^{12}N	11.000 ms	β^+	17338.1	1.21e-03 $\pm$ 1.21e-03
^{13}N	9.965 min	β^+	2220.49	3.63e-03 $\pm$ 2.09e-03
^{16}N	7.13 s	β^-	10419.1	3.87e-02 $\pm$ 6.84e-03
^{17}N	4.173 s	β^-	8680	1.21e-02 $\pm$ 3.82e-03
^{18}N	624 ms	β^-	11916.9	1.21e-03 $\pm$ 1.21e-03
^{14}O	70.606 s	β^+	5143.04	1.21e-03 $\pm$ 1.21e-03
^{15}O	122.24 s	β^+	2754	2.06e-02 $\pm$ 4.99e-03
^{19}O	26.88 s	β^-	4819.6	1.09e-02 $\pm$ 3.63e-03
^{20}O	13.51 s	β^-	2757.45	6.05e-03 $\pm$ 2.70e-03

Isotope	Half Life	Decay Mode	Q-value [keV]	Activity [cpd/100 t]
^{17}F	64.49 s	β^+	2760.8	3.63e-03 ± 2.09e-03
^{18}F	109.77 min	β^+	1655.5	4.11e-02 ± 7.05e-03
^{20}F	11.163 s	β^-	7024.53	3.99e-02 ± 6.95e-03
^{21}F	4.158 s	β^-	5684.2	1.57e-02 ± 4.36e-03
^{22}F	4.23 s	β^-	9543.42	2.42e-03 ± 1.71e-03
^{19}Ne	17.22 s	β^+	3238.4	2.42e-03 ± 1.71e-03
^{23}Ne	37.24 s	β^-	4375.81	8.47e-03 ± 3.20e-03
^{24}Ne	3.38 min	β^-	1994.39	4.84e-03 ± 2.42e-03
^{21}Na	22.49 s	EC	3547.6	8.47e-03 ± 3.20e-03
^{22}Na	2.6027 y	β^+	2842.3	1.99e-02 ± 3.03e-03
^{24}Na	14.997 h	β^-	4146.78	8.34e-02 ± 1.00e-02
^{25}Na	59.1 s	β^-	3835	3.99e-02 ± 6.95e-03
^{26}Na	1.077 s	β^-	7503.27	3.63e-03 ± 2.09e-03
^{23}Mg	11.317 s	EC	4056.1	1.21e-03 ± 1.21e-03
^{27}Mg	9.458 min	β^-	1766.84	7.01e-02 ± 9.21e-03
^{28}Mg	20.915 h	β^-	859.42	1.33e-02 ± 4.01e-03
^{25}Al	7.183 s	β^+	4276.7	4.84e-03 ± 2.42e-03
^{28}Al	2.2414 min	β^-	2862.77	2.23e-01 ± 1.64e-02
^{29}Al	6.56 min	β^-	2406.31	1.40e-01 ± 1.30e-02
^{30}Al	3.62 s	β^-	6325.68	2.78e-02 ± 5.80e-03
^{31}Al	644 ms	β^-	5205.97	2.42e-03 ± 1.71e-03
^{32}Al	33.0 ms	β^-	13020	1.21e-03 ± 1.21e-03

Isotope	Half Life	Decay Mode	Q-value [keV]	Activity [cpd/100 t]
^{27}Si	4.16 s	EC	4812.36	4.84e-03 ± 2.42e-03
^{31}Si	157.36 min	β^-	1491.5	2.33e-01 ± 1.68e-02
^{32}Si	153 y	β^-	227.2	1.26e-03 ± 1.15e-04
^{33}Si	6.11 s	β^-	5845	1.69e-02 ± 4.53e-03
^{34}Si	2.77 s	β^-	4592	1.21e-03 ± 1.21e-03
^{29}P	4.142 s	EC	4942.5	2.42e-03 ± 1.71e-03
^{30}P	2.498 min	EC	4232.4	1.08e-01 ± 1.14e-02
^{32}P	14.268 d	β^-	1710.66	6.52e-01 ± 2.79e-02
^{33}P	25.35 d	β^-	248.5	6.29e-01 ± 2.72e-02
^{34}P	12.43 s	β^-	5382.96	2.06e-01 ± 1.58e-02
^{35}P	47.3 s	β^-	3988.4	8.10e-02 ± 9.90e-03
^{36}P	5.6 s	β^-	7122.1	4.84e-03 ± 2.42e-03
^{30}S	1.178 s	EC	6138	1.21e-03 ± 1.21e-03
^{31}S	2.5534 s	EC	5398.02	3.63e-03 ± 2.09e-03
^{35}S	87.37 d	β^-	167.33	9.74e-01 ± 3.28e-02
^{37}S	5.05 min	β^-	4865.13	2.87e-01 ± 1.86e-02
^{38}S	170.3 min	β^-	2937	8.95e-02 ± 1.04e-02
^{39}S	11.5 s	β^-	5338.78	1.21e-03 ± 1.21e-03
^{34}Cl	1.5266 s	EC	5491.63	7.98e-02 ± 9.83e-03
^{38}Cl	37.230 min	β^-	4916.5	1.71e+00 ± 4.55e-02
^{39}Cl	55.6 min	β^-	3442	2.61e+00 ± 5.62e-02
^{40}Cl	1.35 min	β^-	7480	5.35e-01 ± 2.54e-02
^{35}Ar	1.7756 s	EC	5966.1	3.63e-03 ± 2.09e-03
^{37}Ar	35.011 d	EC	813.87	1.48e+00 ± 4.16e-02
^{39}Ar	269 y	β^-	565	4.02e-02 ± 4.84e-04
^{41}Ar	109.61 min	β^-	2491.61	2.23e+01 ± 1.64e-01
^{38}K	7.636 min	EC	5913.86	7.26e-03 ± 2.96e-03

Bibliography

[1] C. L Cowan et al., Science **124** (1956) 103.

[2] C Lujan–Peschard et al., Eur. Phys. J. C 73 (2013) 2439.

[3] L. Wolfenstein, Phys. Rev. D **17**, 2369 (1978).

[4] S.P. Mikheev and A.Yu. Smirnov, Sov. J. Nucl. Phys. **42**, 913 (1985).

[5] H. A. Bethe and C. L. Critchfield, Phys. Rev. **54** (1938) 248.

[6] C. F. von Weizsäcker , Z Phys. **39** (1938) 633.

[7] H. A. Bethe, Phys. Rev. **55**, (1939) 434.

[8] J.N. Bahcall and C. Peña-Garay, J. High Energy Phys. **11**, 004 (2003).

[9] J.N. Bahcall and M.H Pinsonneault, Phys. Rev. Lett. **92**, 121301 (2004).

[10] J.N. Bahcall, A.M. Serenelli, and S. Basu, Astrophys. J. Suppl. **165**, 400 (2006).

[11] C. Pena-Garay, A.M. Serenelli: arXiv:0811.2424 (2008).

[12] S. Turck-Chiéze et al. APJ **555** (2001) 69.

[13] M. Asplund et al., Nucl. Phys. A **777** (2006) 104.

[14] N. Grevesse and J. Sauval, Space Science Reviews **85** (1998) 161.

[15] M. Asplund et al., Ann. Rev. Astr. & Astrophys. **47** (2009) 481.

[16] T. R. Ayres et al., Astrophys. J. Suppl. Ser. **165** (2006) 618.

[17] L. Koesterke et al., Astrophys. J. **680** (2008) 764.

[18] A. Serenelli, arXiv:0910.3690 (2009).

[19] S. Basu et al., Phys. Rept. **457** (2008) 217.

[20] J.N. Bahcall et al., ApJ **626** (2004) 530.

[21] B. Pontecorvo, Chalk River Rep. PD 205 (1946).

[22] L. W. Alvarez, Univ. Calif. Rad. Lab. Rep. UCRL-328 (1949).

[23] R. Davis, D. S. Harmer, K. C. Hoffman, Phys. Rev. Lett. **20** (1968) 1205.

[24] W. Hampel et al. (GALLEX Collaboration), Phys. Lett. **B420** (1998) 114.

[25] W. Hampel et al. (GALLEX Collaboration), Phys. Lett. B **447**, 127 (1999).

[26] J.N. Abdurashitov et al. (SAGE Collaboration), J. Exp. Theor. Phys. **95**, 181 (2002).

[27] J.N. Abdurashitov et al. (SAGE collaboration), Phys. Rev. C **80**, 015807 (2009).

[28] J.N. Abdurashitov et al. (SAGE Collaboration), Phys. Rev. **C59** (1999) 2246.

[29] M. Altmann et al. (GNO Collaboration), Phys. Lett. B. **490**, 16 (2000).

[30] Y. Fukuda et al. (Kamiokande Collaboration), Phys. Rev. Lett. 77 (1996) 1683

[31] Y. Fukuda et al. (Super-Kamiokande Collaboration), Phys. Rev. Lett. **81**, 1562 (1998).

[32] B. Aharmim et al. (SNO Collaboration), Phys. Rev. C **72**, 055502 (2005).

[33] B. Aharmim et al. (SNO Collaboration), Phys. Rev. C **75**, 045502 (2007).

[34] K. Nakamura et al. (Particle Data Group), J. Phys. G **37**, 075021 (2010).

[35] T. K. Gaisser, Phys. Scr. T **121** 51 (2005).

[36] K.S. Hirata et al. (KamiokaNDE Collaboration), Phys. Rev. Lett. 63, 16 (1989).

[37] R. Becker–Szendy et al., Phys. Rev. D **46** (1992) 3720.

[38] W. W. M. Allison, et al. Phys. Lett. B **391** (1997) 491.

[39] M. Ambrosio et al. (MACRO Collaboration), Astropart. Phys. **19**, 313 (2003).

[40] M Sanchez et al. Phys. Rev. D **68** (2003) 11304.

[41] K. Abe et al. (Super–Kamiokande Collaboration), Phys. Rev. Lett. **110** (2013) 181802.

[42] F. Reines et al., Phys. Rev.**92** (1953) 830.

[43] K. Eguchi et al. (KamLAND Collaboration), Phys. Rev. Lett. **90**, 021802 (2003).

[44] S. Abe et al. (KamLAND Collaboration), Phys. Rev. Lett. **100** (2008) 221803.

[45] M. Apollonio et al., Phys. Lett. B **466** (1999) 415.

[46] F. Boehm et al.,Phys.Rev. D **62** (2000) 072002.

[47] Y. Abe et al. (Double CHOOZ), Phys. Rev. D **86** (2012) 052008.

[48] F. P. An et al. (Daya Bay Collaboration), Phys. Rev. Lett. **108** (2012) 171803.

[49] J. K. Ahn et al. (RENO Collaboration), Phys. Rev. Lett. **108** (2012) 191802.

[50] G. Mention et al., Phys. Rev. **D83** (2011), 073006.

[51] M. Ahn et al. (K2K Collaboration), Phys. Rev. D **74** (2006) 072003.

[52] P. Adamson et al. (MINOS Collaboration), Phys. Rev. Lett. **110** (2013) 251801.

[53] N. Agafonova et al. (OPERA Collaboration), JHEP **11** (2013) 036.

[54] K. Abe et al. (T2K Collaboration), arXiv:1311.4750 (2013).

[55] A.A. Aguilar-Arevalo et al. (MiniBooNE Collaboration), Phys. Rev. Lett. **110** (2013) 161801.

[56] C. Athanassopoulos et al. (LSND Collaboration), Phys. Rev. Lett. **77** (1996) 3082.

[57] B. Armbruster et al. (KARMEN Collaboration), Phys. Rev. D **65** (2002) 112001.

[58] B. Pontecorvo, JETP **53** (1967) 1717.

[59] A. C. Hayes et al., arXiv:1309.4146 (2013).

[60] C. Zhang et al., Phys. Rev. **D87** (2013) 073018.

[61] C. Giunti and M. Laveder, Phys. Rev. **C83** (2011) 065504.

[62] C. Giunti, arXiv:1311.1335 (2013).

[63] P.A.R. Ade et al. (Planck collaboration), arXiv:1303.5076

[64] A. Mirizzi et al., Phys. Lett. B **726** (2013) 8.

[65] F. Capozzi et al., arXiv:1312.2878 (2013);

[66] S. Agostinelli et al., IEEE T. Nucl. Sci. **53** No. 1 (2006) 270.

[67] H. Back et al. (Borexino Collaboration), JINST **7** (2012) P10018.

[68] G. Bellini et al. (Borexino Collaboration), JINST **6** (2011) P05005.

[69] M. Deutsch, *"Proposal for a Cosmic Ray Detection System for the Borexino Solar Neutrino Experiment"*, Massachusetts Institute of Technology, Cambridge, MA (1996).

[70] M. Cribier et al., Astropart. Phys. **6**, 129 (1997).

[71] T. Hagner et al., Astropart. Phys. **14** (2000) 33.

[72] S. Abe et al. (KamLAND Collaboration), Phys. Rev. **C81**, 025807 (2010).

[73] G. L. Fogli, E. Lisi, A. Marrone, A. Palazzo and A. M. Rotunno, arXiv:0806.2649 (2008).

[74] A. Palazzo, Mod. Phys. Lett. **A28** No. 7 (2013) 1330004.

[75] G. Bellini et al. (Borexino Collaboration), Phys. Rev. D **89** 112007 (2014).

[76] M. Agostini et al. (Borexino Collaboration), Phys. Rev. D **92** (2015) 031101.

[77] G. Bellini et al. (Borexino Collaboration), Phys.Rev. C **81** (2010) 034317.

[78] M. Agostini et al. (Borexino Collaboration), arXiv:1509.01223 (2015).

[79] H. Simgen, G. Zuzel, Appl. Radiat Isot. **67** 922 (2009).

[80] P. Agnes et al. (DarkSide Collaboration) Phys. Lett. B **743** 456 (2015).

[81] C. Galbiati talk at the LNGS Scientific Committee, April 2015, https://agenda.infn.it/conferenceDisplay.py?confId=9608.

[82] J. Xu et al., physics/1204.6011 (2012).

[83] P. Agnes et al. (DarkSide Collaboration) arXiv-xxxxxxxx.

[84] T. Doke, K. Masuda, E. Shibamura, Nucl. Instr. Meth. A **291-3** (1990) 617.

[85] W. H. Lippincott et al., Phys. Rev. C **81** (2010) 045803.

[86] C. Cattadori, J. Phys.: Conf. Ser. **375** 042008 (2012).

[87] A. S. Barabash, V. N. Kornoukhov, V. E. Jants NIM A **385** 530 (1997).

[88] M. Cribier et al., Astropart. Phys. **6** (1997) 129.

[89] G. Bellini et al. (Borexino Collaboration), JCAP **1308** (2013) 049.

[90] S. Abe et al. (KamLAND Collaboration), Phys. Rev. C **81** 025807, 2010.

[91] M. Ambrosio et al. (MACRO Collaboration) Phys. Rev. D **52** 3793 (1995).

[92] N. Agafonova et al. (OPERA Collaboration), Eur. Phys. J. C **67** 25 (2010).

[93] I. Ostrovskiy et al., physics/502.07837 (2015).

[94] M. Koehler et al., Appl. Radiat. Isot. **61** 207 (2004).

[95] W. Maneschg et al., NIM A **593** 448 (2008).

[96] W. Verkerke and D. Kirkby physics/0306116 (2003).

[97] E. Aprile, W. Hsin-Min Ku, J. Park, H. Schwartz, Nucl. Instrum. Meth. A **261** Issue 3 (1987) 519.

[98] A. Serenelli, C. Pena-Garay, W. C. Haxton, Phys. Rev. D **87** 043001 (2013).

[99] E. G. Adelberger et al., Rev. Mod. Phys. **83** 195 (2011).

[100] Y.-F. Li, J. Cao, Y. Wang, and L. Zhan, Phys.Rev. D **88** (2013) 013008.

[101] U. F. Katz, arXiv:1402.1022 (2012).

[102] M. G. Aartsen et al. (IceCube-Pingu Collaboration), arXiv:1401.2046 (2014).

[103] INO, India-based neutrino observatory, http://www.ino.tifr.res.in/ino/.

[104] K. Abe et al. (2011), arXiv:1109.3262.

[105] K. N. Abazajian et al., arXiv:1204.5379 (2012).

[106] J. Ashenfelter et al. (PROSPECT Collaboration), arXiv: 1309.7647 (2013).

[107] Danilov M (DANSS Collaboration), arXiv::1311.2777 (2013).

[108] G. Bellini et al. (Borexino/SOX Collaboration), JHEP **1308** (2013) 038.

[109] M. Antonello et al. (ICARUS and NESSiE Collaborations), CERN-SPSC-2012-010 and SPSC-P-347 (2012).

[110] A. Bungau et al., Phys. Rev. Lett. **109**, 141802 (2012).

Curriculum Vitae

Work Experience:

SINCE 10/2014	**CNRS CR1 Researcher** at Laboratoire Astroparticule et Cosmologie
10/2010 – 09/2014	**CNRS CR2 Researcher** at Laboratoire Astroparticule et Cosmologie
11/2005 – 07/2010	**Post–Doc** at Università degli Studi di Milano (Italy)
01/2005 – 10/2005	**Post–Doc** at Max Planck Institut fuer Kernphysik (Heidelberg, Germany)

Education:

07/2009	**INFN R5 habilitation**
01/2005	**Ph.D.** in Physics *in cotutelle* from **Milano** and **Heidelberg** Universities *Dr. Rer. Nat.: Magna Cum Laude* Thesis: The Borexino experiment: test of the purification systems and data analysis in the Counting Test Facility Advisors: Prof. G. Bellini and Prof. W. Hampel
07/2001	**Laurea in Physics** from **Milano** University *110/110 Cum Laude* Thesis: The Borexino experiment at Gran Sasso Laboratories: development of an analytical approach for the evaluation of the detector sensitivity. Advisors: Prof. G. Bellini and S. Malvezzi

Research Responsibilities:

LABEX UNIVEARTHS	Project Coordinator of the Jeune Equipe JE2.
NUTOPS	Project Coordinator (ANR-JCJC).
DARWIN	Local Coordinator at APC.
DARKSIDE	Member of the Institutional Board; Member of the Steering Committee; Monte Carlo Group Coordinator.
BOREXINO	Member of the Institutional Board; Monte Carlo Group Coordinator; ^{8}B neutrino Analysis Group Coordinator.

Grants:

01/2015 – 12/2017	LabEx UnivEarthS Jeune Equipe JE2 – Dark Matter Search with DarkSide (150 kEuro) – **D.F. principal investigator**
01/2014 – 12/2015	FACCTS – France and Chicago Collaborating in the Sciences – Simulation of liquid argon scintillation – (15 kDollar) – **D.F. co–principal investigator**
12/2011 – 11/2015	ANR JCJC – NuToPs: Positronium signature in scintillators for neutrino detection (171 kEuro) – **D.F. principal investigator**
12/2013	Appel d'offre physique recherche Universitè Paris Diderot – Dèveloppement de photodétecteurs SiPM (11 kEuro) – **D.F. principal investigator**
02/2013 – 01/2016	ASPERA Grant – LOWE-NUs: A Concerted R&D Program for Low Energy Neutrino Detectors (165 kEuro)
08/2012 – 07/2015	EU-FP7 – LAGUNA-LBNO: sensitivity study (5,000 kEuro)

Referee and Editor:

- Referee: Physical Review Letter, Physical Review Special Topics: Accelerators and Beams, Physical Review D, Physical Review C.
- Guest Editor: Advances in High Energy Physics Special Issue on the Direct Dark Matter Search.

Teaching and Supervision:

SINCE 2014:	Co-director of PhD thesis of T. Houdy (SOX experiment) ED STEP'UP
SINCE 2013:	Co-director of PhD thesis of P. Agnes (DarkSide experiment) ED STEP'UP
2015:	Member of the jury (*examinateur*) for the PhD thesis of M. Tenconi (U. Paris Sud)
2012–2014:	Supervisor of the Post-Doc S. Perasso on the ANR-JCJC "NuToPs" project
2011–2012:	Supervisor of the Post-Doc C. Ghiano (Borexino)
2013:	Supervisor of L2 stage (2 months) of H. Bel at Paris-Diderot University
2013:	Supervisor of NPAC M2 mini-stage on direct detection of dark matter with the DarkSide experiment
2012:	Supervisor of NPAC M2 mini-stage on antineutrino detection with Double Chooz
2012:	Supervisor of NPAC M2 internship of A. Loiret: "Enhancing the Anti-Neutrino Signature in the Double Chooz Experiment"
2011:	Member of the jury for the PhD thesis of M. Buizza Avanzini (U. Milano)
2010-2011:	Co-supervisor of internship of W. Maneschg at Max-Planck-Institut fuer Kernphysik and Heidelberg University: "Low-energy solar neutrino spectroscopy with Borexino: Towards the detection of the solar pep and CNO neutrino flux"
2007–2008:	Co-supervisor of M2 internship of M. Buizza Avanzini at Milano University: "Studio dei neutrino solari da ^{8}B con l'esperimento Borexino e delle sistematiche ad esso associate"
2007–2008:	Co-supervisor of L3 internship of R. Cuozzo at Milano University "Studio dei fondi indotti da muoni cosmici nel rivelatore Borexino"
2006–2007:	Co-supervisor of L3 internship of S. Consonni at Milano University: "Studio del fondo cosmogenico nella regione dei neutrini solari da pep e CNO nel rivelatore Borexino"
2006–2007:	Assistant Professor, "Laboratorio di Calcolo I", Milano University
2003–2004:	Assistant Professor, "Physics Laboratory: Mechanics and Electromagnetism", Heidelberg University
2002–2003:	Assistant Professor, "Computational Methods in Physics", Milano University

Science Communication:

09/2014:	Interview at the radio broadcast France Inter La tête au carré, with subject: "Soleil et neutrinos".
1998/2000:	Scientific guide at the National Museum of Science and Technology "Leonardo Da Vinci", Milano.

Conferences and Seminars:

- Talk at Rencontres de Moriond (EW Interactions and Unified Theories): "First results from DarkSide-50", Mar 2015.
- Talk at Planck 2014 (Paris): "DarkSide-50", May 2014.
- Seminar at SPP Saclay (Paris): "Recent results from DarkSide-50", May 2014.
- Seminar at APC (Paris): "Direct dark matter search with DarkSide-50", April 2014.

- Talk at Conseil Scientifique IN2P3 (Paris): "Sterile neutrino search with sources: SOX & CeLAND", June 2013.
- Talk at GdR Neutrino (Caen): "Borexino results and future perspectives", October 2012.
- Talk at Conseil Scientifique IN2P3 (Paris): "Dark Side and its perspectives", October 2012.
- Talk at NOW 2012 (Otranto): "Results from Borexino", September 2012.
- Seminar at LPNHE (Paris) and IPHC (Strasbourg): "Solar neutrino spectroscopy and oscillation with Borexino", November 2011 and February 2012.
- Talk at the ANT 2011 (Philadelphia): "Positronium signature in organic liquid scintillators for neutrino experiments", October 2011.
- Seminar at the LAPP (Annecy): "Recent (and future) results from Borexino", July 2011.
- Talk at the LNGS Scientific Committee: "Report on Borexino activities", May 2010.
- Seminars at APC (Paris) and CPPM (Marseilles) (ppt and pdf): "Neutrino physics with Borexino", January 2010.
- Talk at IFAE2009 (Bari): "Solar Neutrino Physics with Borexino", April 2009
- Talk at SIF2008 (Genova): "11C background suppression in the CNO-pep solar neutrino energy region with Borexino", September 2008
- Poster at Neutrino 2008 (Christchurch, New Zealand): "Performances and Calibrations of the Borexino Detector", June 2008.
- Talk at NOW2008 (Otranto): "Measurement of the solar 8B neutrino flux with 246 live days of Borexino ...and observation of the MSW vacuum-matter transition!", September 2008.
- Seminar at LIP (Lisbon): The first year of Borexino data", July 2008
- Talk at HQL08 (Melbourne): The first year of Borexino data", June 2008.
- Seminar at Milano University (Milano): "Neutrino physics with the Borexino detector at the Gran Sasso Laboratory", November 2007.
- Poster at Neutrino 2006 (Santa Fe) "CNO and pep neutrino spectroscopy in BOREXino: measurement of the cosmogenic 11C background with the Counting Test Facility", June 2006.
- Talk (pdf, ppt) at LRT 2006 Workshop (Aussois): "Measurement of the cosmogenic 11C background with the Borexino Counting Test Facility", October 2006.
- Talk (pdf, ppt) at Now 2004 Workshop: "11C measurement and the CNO and pep fluxes in Borexino", September 2004.
- Seminar at Milan: "Measuring ultra trace levels of Ar and Kr in nitrogen for the purification of the Borexino scintillator", October 2004

Publication Summary

- 103 citable publications
- 57 refereed publications
- 4 refereed publications with DF corresponding author

Selected Published Papers

- *Neutrinos from the primary proton-proton fusion process in the Sun*, Borexino Collaboration, Nature 512 (2014) 7515, 383.
- *Final results of Borexino Phase-I on low energy solar neutrino spectroscopy*, Borexino Collaboration, Phys. Rev. D89 (2014) 112007.
- *SOX: Short distance neutrino Oscillations with BoreXino*, Borexino/SOX Collaboration, JHEP 1308 (2013) 038.
- *Mass hierarchy discrimination with atmospheric neutrinos in large volume ice/water Cherenkov detectors*, D. Franco (corresponding author), C. Jollet, A. Kouchner, V. Kulikovskiy, A. Meregaglia, S. Perasso, T. Pradier, A. Tonazzo, V. Van Elewyck, JHEP 1304 (2013) 008.
- *Reactor electron antineutrino disappearance in the Double Chooz experiment*, Double Chooz Collaboration, Phys.Rev. D86 (2012) 052008.
- *First evidence of pep solar neutrinos by direct detection in Borexino*, Borexino Collaboration, Phys. Rev. Lett. 108 (2012) 051302.
- *Positronium signature in organic liquid scintillators for neutrino experiments*, D. Franco (corresponding author), G. Consolati, D. Trezzi, Phys. Rev. C83 (2011) 015504.
- *Observation of Geo-Neutrinos*, Borexino Collaboration, Phys. Lett. B687 (2010) 299-304.
- *The Classification of Flaring States of Blazars*, E. Resconi, D. Franco, A. Gross, L. Costamante, E. Flaccomio, Astron.Astrophys. 502 (2009) 499-504.
- *CNO and pep neutrino spectroscopy in Borexino: Measurement of the deep-underground production of cosmogenic C11 in an organic liquid scintillator*, Borexino Collaboration (D. Franco corresponding author), Phys. Rev. C74 (2006) 045805.